

COOLANT SIDE HEAT TRANSFER WITH ROTATION TASK III REPORT: APPLICATION OF COMPUTATIONAL FLUID DYNAMICS

By

F.C. Kopper, G.J. Sturgess and P. Datta

January 1989

contract NAS3-23691. These limitations shall be considered void two (2) years after date on these data. This legend shall be marked on any reproduction of these data in whole or in part.

UNITED TECHNOLOGIES CORPORATION

Pratt & Whitney

Commercial Engine Business

Prepared for

National Aeronautics and Space Administration

NASA Lewis Research Center

21000 Brookpark Road

Cleveland, Ohio 44135

Contract NAS3-23691



National Aeronautics and
Space Administration

N91-24551

Unclas
0019854

G3/34

CSCL 20D

(NASA-CR-182109) COOLANT SIDE HEAT TRANSFER
WITH ROTATION. TASK 3 REPORT: APPLICATION OF
COMPUTATIONAL FLUID DYNAMICS (PWA) 91 p



FOREWORD

This document was prepared by F. C. Kopper, Dr. G.J. Sturgess and Dr. P. Datta of Commercial Engineering, Commercial Engine Business of Pratt & Whitney, United Technologies Corporation, East Hartford, CT. It describes a study to develop and verify computational methods for predicting local heat transfer and coolant pressure drop within the coolant passages of rotating turbine blades. This work was carried out under the sponsorship of the National Aeronautics and Space Administration under Contract NAS3-23691. This report describes a part of Phase I, Task III of this contract. The work was performed under the direction of Dr. F. Yeh, NASA Project Manager, and Mr. F. Kopper, Pratt & Whitney Program Manager.

PRECEDING PAGE BLANK NOT FILMED

TABLE OF CONTENTS

<u>Section</u>	<u>Page</u>
1.0 SUMMARY	1
2.0 INTRODUCTION	2
2.1 Objectives	3
3.0 COMPUTATIONAL APPROACHES	4
3.1 Basic Procedure	4
3.2 Baseline Code and Its Features	5
3.3 Suitability of Baseline Code	11
3.3.1 Turbulence Model	12
3.3.2 Treatment of Curvilinear Surfaces	15
3.3.3 Use of Wall Functions to Represent Boundary Layers	15
3.3.4 Numerical Diffusion	15
3.3.5 Summary	15
3.4 Modifications for Rotation	16
3.5 Exploratory Calculations	18
4.0 EXPERIMENTAL DATA	22
4.1 Benchmark-Quality Experiments	23
4.2 Selected Experiments	24
4.2.1 Effects of Rotation	24
4.2.2 Effects of Duct Aspect Ratio with Rotation	25
4.2.3 Surface Heat Transfer in a Sharp Bend	26
5.0 COMPARISONS OF CALCULATIONS AND MEASUREMENTS	28
5.1 Effects of Rotation	28
5.1.1 Computational Set-Up	28
5.1.2 Flow Visualization	28
5.1.3 Mean Velocity Development	29
5.1.4 Fluctuating Quantities	32
5.1.5 Summary	35
5.2 Effects of Duct Aspect Ratio with Rotation	35
5.2.1 Computational Set-Up	35
5.2.2 Flow Visualization	35
5.2.3 Velocity Profile Development	36
5.2.4 Effects of Rotation	38
5.2.5 Summary	39
5.3 Surface Heat Transfer in a Sharp Bend	40
5.3.1 Computational Set-Up	40
5.3.2 Comparison Conditions	40
5.3.3 Flow Visualization	40
5.3.4 Surface Heat Transfer	41
5.3.5 Summary	42

TABLE OF CONTENTS
(Continued)

<u>Section</u>	<u>Page</u>
6.0 DISCUSSION OF RESULTS	43
6.1 General Observations	43
6.2 Fluid Dynamics	44
6.3 Heat Transfer	47
6.4 Summary	47
7.0 CONCLUSIONS AND RECOMMENDATIONS	48
7.1 Conclusions	48
7.2 Recommendations	48
APPENDICES	
A1: DESCRIPTION OF 3D-TEACH CODE	49
A2: TREATMENT OF WALL BOUNDARY LAYERS IN BASELINE CODE	67
A3: EXTRA TERMS DUE TO SYSTEM ROTATION	74
REFERENCES	81

LIST OF ILLUSTRATIONS

<u>Figure</u>	<u>Title</u>	<u>Page</u>
2.1	Blade Internal Geometry (JT8D)	1
2.2	Program Structure	3
3.1	Summary of Some of the Equations Solved in 3D-TEACH	6
3.2	Modification Procedure to Develop Code for Turbine Blade Analysis	12
3.3	Coolant Passage Heat Transfer Model	14
3.4	Coordinate System for a Rotating Frame of Reference	16
3.5	Schematic of Coolant Passage for Exploratory Calculation	18
3.6	Grid for Exploratory Calculations	19
3.7	Test of Momentum Equation - Flow Visualization	21
3.8	Streakline Cross Sections for a Range of Rotational Speeds	22
4.1	Rotational Passage of Moon's Experiment	25
4.2	Schematic of Moore's Test Section to Explore Aspect Ratio	26
4.3	Flow Passage for Heat Transfer in a Sharp Turn	27
4.4	Definition of Heated Test Sections for Heat Transfer Measurements	27
5.1	Calculated Secondary Flow Patterns Due to Coriolis Forces With Rotation (Moon's Experiment)	29
5.2	Calculated and Measured Mean Axial Velocity Profiles in Moon's Experiment	30
5.3	Comparisons of Boundary Layer Thicknesses Along Pressure and Suction Walls of Moon's Duct	31
5.4	Comparison of Momentum Thickness on Suction Wall of Moon's Duct	31
5.5	Skin Friction Coefficient Variation Along Pressure and Suction Walls in Moon's Duct	32
5.6	Kinetic Energy of Turbulence Profiles Across Moon's Duct Close to Exit	33
5.7	Reynolds Stress Comparison Across Moon's Duct on Inflow Leg	34
5.8	Streaklines Showing Vortex Development for Different Aspect Ratio Ducts in Moore's Experiment	36
5.9	Calculated Effects of Duct Aspect Ratio on Mean Axial Velocity Profiles in Moore's Experiment	37
5.10	Comparison of Calculated and Measured Aspect Ratio Effects on Mean Axial Velocity Profiles	38
5.11	Calculated Effect of Rotation Number on Mean Axial Velocity Profiles in Moore's Experiment	39
5.12	Experimental Visualization of Flow Development on Bottom Surface of a Sharp Turn, Showing Separated Flow Regions	40
5.13	Calculated Streakline Flow Visualization on Bottom Surface of Metzger's Experiment Showing Separated Flow Regions	41
5.14	Comparison of Measured and Calculated Nusselt Numbers at Two Reynold Numbers in Metzger's Sharp Turn Experiment	42
6.1	Clauser Plot of Axial Velocity Profiles for Moon's Experiment	46

LIST OF TABLES

<u>Table</u>	<u>Title</u>	<u>Page</u>
I	Additional Source Terms Due to Rotation	17
II	Operating Conditions for Exploratory Calculation	20

1.0 SUMMARY

The National Aeronautics and Space Administration (NASA) is sponsoring an experimental and analytical program to investigate heat transfer within rotating turbine blades. The program is to generate flow, heat transfer, and pressure drop data for rotating passages simulating blade passages. The passages are multipass in configuration, with and without turbulators on the walls, to simulate the configurations and conditions expected in the first stage blades of advanced aircraft gas turbines. The experimental results are to be manipulated to provide data correlations for an empirically-based design system. The feasibility of developing computational fluid dynamic techniques for calculating the flows in such passages is to be explored.

This report presents a part of the planned Phase I, Task III effort which covers analysis and data correlation.

The Pratt & Whitney 3D-TEACH (Teaching Elliptic Axisymmetric Characteristics Heuristically) CFD (Computational Fluid Dynamics) code was selected as a suitable vehicle for modification to meet the needs of the program. This state-of-the-art viscous flow computational fluid dynamics computer code has been revised to account for rotating internal flows. The modifications made have been evaluated for flows characteristic of those expected in the application. For this purpose, experimental studies extant in the literature were used. The results, while encouraging, reveal some limitations for the present codes.

2.0 INTRODUCTION

In current design technology there is a need to predict the effects of rotation on local heat transfer and pressure loss within coolant passages of turbine blades, particularly blades that have multipass coolant passages, such as shown in Figure 2.1. Accurate calculation of these quantities is very important as it can lead to an improvement in the reliability of predicting turbine airfoil temperatures and ultimately, blade life. Accurate estimates of temperature and life permit available cooling air to be used most effectively and reduces its negative impact on turbine performance.

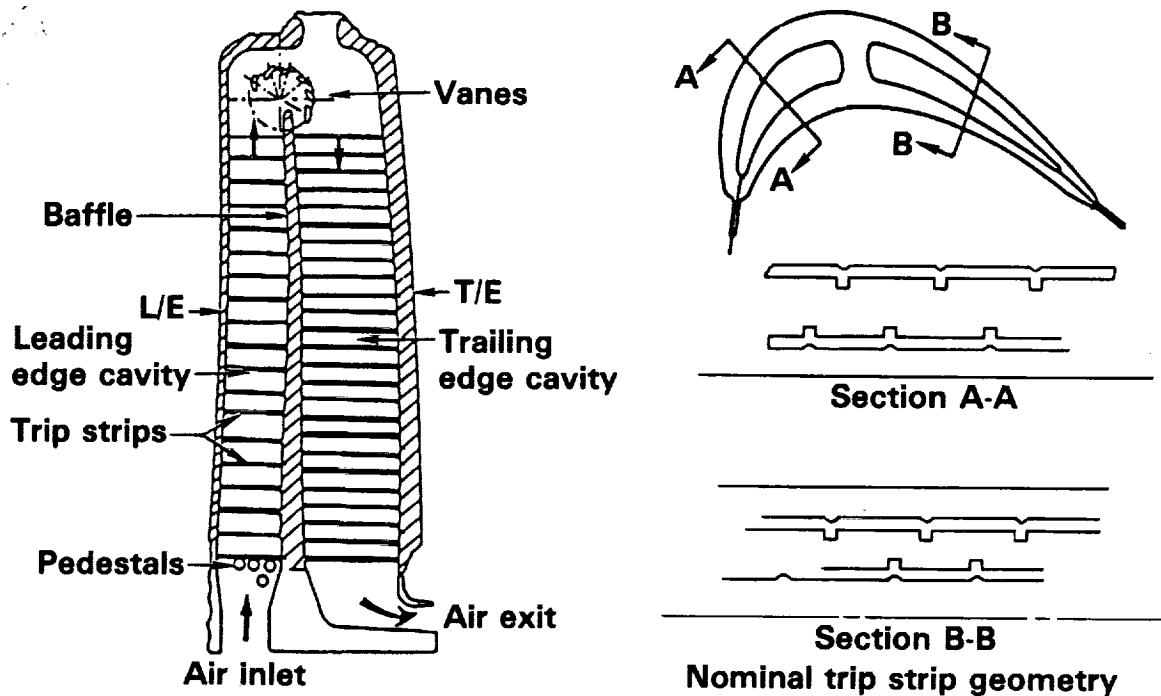


Figure 2.1 Blade Internal Geometry (JT8D)

In recognition of these requirements, the National Aeronautics and Space Administration (NASA), through its Lewis Research Center and under the aegis of the HOST program, is sponsoring an experimental and analytical study of heat transfer and pressure loss in rotating multipass passages with configurations and dimensions typical of modern turbine blades.

Computational fluid dynamics techniques, although far from completely developed, have shown potential for calculating the internal flows in the gas turbine engine. The complexity of the flow within turbine blades suggests that comprehensive empirical correlations of data will be difficult to obtain. Therefore, there is strong motivation to apply computational techniques to a) understand the flow development, b) assist in determining suitable correlations for the experimental data, and c) eventually, provide a quantitatively-accurate calculation procedure.

2.1 Objectives

The overall objective of the NASA program is to develop and verify improved analysis methods that will form the basis for a design system which will result in efficient turbine components with improved durability. This objective is to be achieved through three program elements. The first element is to establish a comprehensive experimental database that can form the basis of an empirical design system. The second is to develop computational fluid dynamic techniques for this application. Finally, the third element is to analyze the information in the database with mathematical modeling to devise a suitable design and analysis procedure. The approach is illustrated in Figure 2.2. This report is concerned with part of the second of these elements - the computational fluid dynamic aspects.

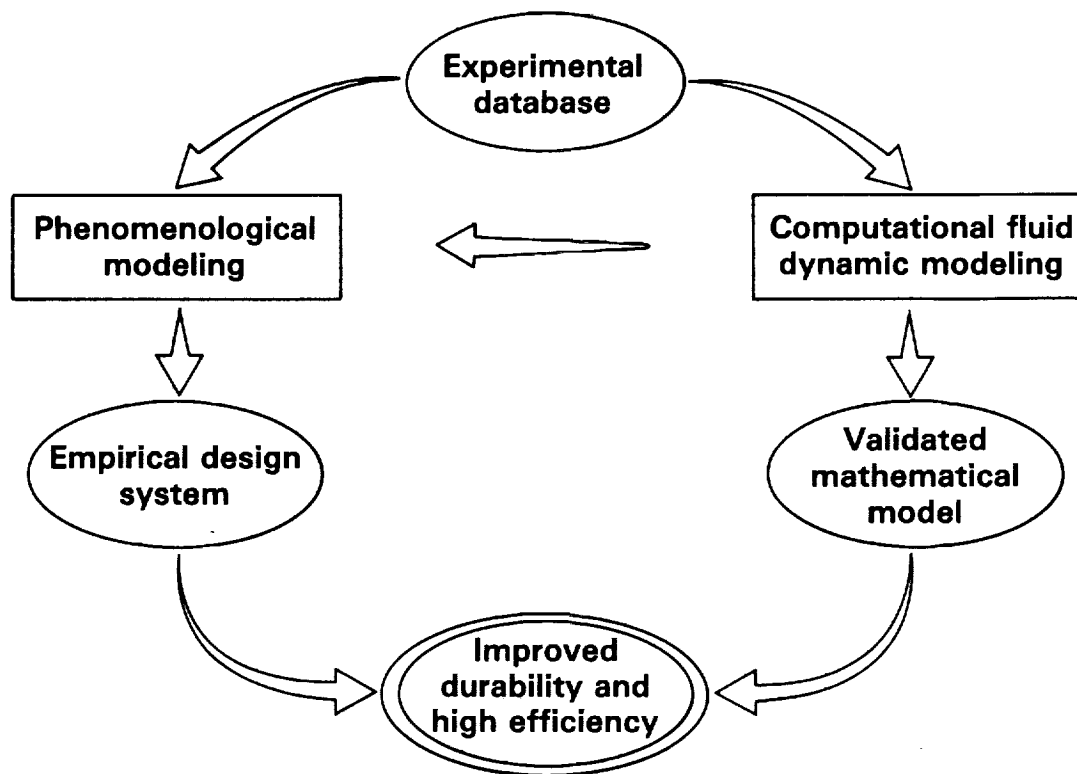


Figure 2.2 Program Structure

The specific objectives of the work presently reported were to:

1. Select a baseline CFD computer code
2. Assess the limitations of the baseline code
3. Modify the baseline code for rotational effects
4. Verify the modified code against benchmark experiments in the literature
5. Identify shortcomings in the code as revealed by the verification.

3.0 COMPUTATIONAL APPROACH

Accurately predicting the local coolant-side heat transfer coefficients, coolant temperature rise and pressure drop over a wide range of operating conditions and geometries in the cooling passages is a formidable task because of the turbulent, three-dimensional, elliptic nature of the flow. Further complications are introduced by the effects of rotation and turbulence - promoting devices frequently introduced into the passages. Figure 2.1 illustrates these features in a typical passage.

3.1 Basic Procedure

Computational fluid dynamics methods in general fall into four main classes, namely:

1. Incompressible potential flow solutions
2. Solutions based on viscous-inviscid interaction approaches
3. Parabolic time-marching finite difference methods for viscous flows
4. Elliptic iterative finite difference methods for viscous flows

It can be appreciated that this list of classes is one of increasing physical realism and flexibility to handle more complex problems. It also is a list representing increasing difficulty, complexity, and cost. The character of the flow field described above, and to be calculated, dictates an approach from Class 4.

Within Class 4, the TEACH-code was selected for the present program because it represented the only Class 4, generalized, three-dimensional, viscous, elliptic flow code currently available at Pratt & Whitney that was sufficiently developed to be considered. The approach used in this code for turbulence management (time-mean/wholly statistical) represents a technically reasonable and computationally economic approach in an engineering environment (Ref. 1).

The computational approach selected is one being developed by Pratt & Whitney for three-dimensional, viscous, reacting, elliptic flow calculations for the combustor and other gas turbine applications. The procedure is known by the acronym 3D-TEACH. It is one of a family of such codes being developed by Pratt & Whitney, and its generic solution approach is well-known and accepted in the industry. The acronym TEACH (Teaching Elliptic Axisymmetric Characteristics Heuristically) represents a generic solution technique (Ref. 2) and these codes represent current production state-of-the-art calculations in terms of equations solved, physical models used, discretization of the equations, and the solution algorithms. They are not perfect, but are a marked advance from one-dimensional flow calculations and global modeling that formed the previous capability. The structure of the codes has been made such that modular replacement can be carried out as better models and solution algorithms are developed, while the basic framework and operational features remain.

The Pratt & Whitney 3D-TEACH code is a generalized aerothermal, fluid dynamic solver for steady, three-dimensional, elliptic, turbulent, reacting flows. The approach stays within the framework of continuum mechanics and uses a statistical description of turbulence, coupled with the accepted Eulerian description provided by the Navier-Stokes equations of motion. Closure to the resulting time-mean equations is provided by turbulence modeling of the eddy viscosity type. The modeled partial differential equations are manipulated into a general form that permits a single solution algorithm to be used for a numerical procedure. A hybrid (upwind/central) finite differencing scheme is used to discretize the equations. An outline of the solution procedure is given in Appendix A1. In original form, the code was derived at Imperial College, London, England, as a teaching aid.

3.2 Baseline Code and Its Features

The Pratt & Whitney 3D-TEACH code is being developed for application to the combustion chamber of the gas turbine engine (Ref. 3). In cylindrical coordinates, it solves the general steady flow equation,

$$\begin{aligned} \frac{\partial}{\partial x} (\bar{\rho} \bar{u} \bar{\phi}) + \frac{\partial}{r \partial \theta} (r \bar{\rho} \bar{v} \bar{\phi}) + \frac{\partial}{r \partial \theta} (\bar{\rho} \bar{w} \bar{\phi}) - \frac{\partial}{\partial x} (\Gamma_{\text{eff},\theta} \cdot \frac{\partial \bar{\phi}}{\partial x}) - \frac{\partial}{r \partial r} (r \Gamma_{\text{eff},\theta} \cdot \frac{\partial \bar{\phi}}{\partial r}) \\ - \frac{\partial}{r \partial \theta} \left(\frac{1}{r} \Gamma_{\text{eff},\theta} \cdot \frac{\partial \bar{\phi}}{\partial \theta} \right) = S_{\phi} \end{aligned} \quad (3.1)$$

where overbars denote time-averaged quantities, and,

- ρ = gas density
- u, v, w = gas velocities in x, r, θ directions, respectively
- ϕ = any of the independent variables
- $\Gamma_{\text{eff},\theta}$ = an appropriate turbulent exchange coefficient, depending on what ϕ represents
- S_{ϕ} = a so-called "source term" which lumps together all other items in a given equation not included in the first six terms of Equation 3.1.

This general form was adopted so that a single solution algorithm could be used in the numerical procedure, which is given in Appendix A1. By way of example, Figure 3.1 gives the values of some of the parameters in Equation 3.1. Those shown are relevant for the present application. However, the code also contains information relevant to its combustion application, including, for example, species equations with source terms to describe the reaction rate of a fuel, etc. This extraneous information was stripped from the code to establish a baseline code for use in this turbine study.

EQUATION	ϕ	$r_{EH,\phi}$	S_ϕ
CONTINUITY	1	0	0
x-MOMENTUM	\bar{u}	μ_{EH}	$\bar{p}_x \cdot \frac{\partial \bar{p}}{\partial x} + \frac{\partial}{\partial x} \left(\mu_{EH} \frac{\partial \bar{u}}{\partial x} \right) + \frac{\partial}{\partial r} \left(\mu_{EH} r \frac{\partial \bar{v}}{\partial x} \right) - \frac{2}{3} \frac{\partial}{\partial x} (\mu_{EH} \nabla \cdot \vec{v}) + \frac{\partial}{\partial \theta} \left(\mu_{EH} \frac{\partial \bar{w}}{\partial x} \right)$
r-MOMENTUM	\bar{v}	μ_{EH}	$-\frac{\partial \bar{p}}{\partial r} + \bar{p}_r + \frac{\partial}{\partial x} \left(\mu_{EH} \frac{\partial \bar{u}}{\partial r} \right) + \frac{\partial}{\partial r} \left(r \mu_{EH} \frac{\partial \bar{v}}{\partial r} \right) - \frac{\partial}{\partial r} \left(\frac{2}{3} \mu_{EH} \nabla \cdot \vec{v} \right) - \frac{\partial}{\partial \theta} \left(\mu_{EH} \frac{\partial \bar{w}}{\partial r} \right) + \frac{\bar{w}^2}{r} - \frac{2\mu_{EH}\bar{v}}{r^2} - \frac{2\mu_{EH}}{r^2} \frac{\partial \bar{w}}{\partial \theta} - \frac{1}{r} \frac{\partial}{\partial \theta} (\mu_{EH} \bar{w})$
θ -MOMENTUM	\bar{w}	μ_{EH}	$-\frac{\partial \bar{p}}{r \partial \theta} + \frac{\partial}{r \partial \theta} \left(\mu_{EH} \frac{\partial \bar{w}}{\partial \theta} \right) + \frac{\partial}{\partial x} \left(\mu_{EH} r \frac{\partial \bar{u}}{\partial \theta} \right) + \frac{\partial}{\partial r} \left(\mu_{EH} \frac{\partial \bar{v}}{r \partial \theta} \right) - \frac{2}{3} \frac{\partial}{\partial \theta} (\mu_{EH} \nabla \cdot \vec{v}) + \frac{2\mu_{EH}}{r} \frac{\partial \bar{v}}{r \partial \theta} - \frac{\bar{v}\bar{w}}{r} - \frac{\bar{w}}{r^2} \frac{\partial}{\partial r} (\mu_{EH} r)$
TURBULENCE ENERGY	K	μ_{EH}/σ_K	$\mu_{EH} \left[2 \frac{\partial \bar{v}}{r \partial \theta} \frac{\partial \bar{w}}{\partial r} + 2 \frac{\partial \bar{w}}{\partial x} \frac{\partial \bar{u}}{r \partial \theta} + \left(\frac{\partial \bar{u}}{r \partial \theta} \right)^2 + \left(\frac{\partial \bar{v}}{r \partial \theta} \right)^2 + 2 \left(\frac{\partial \bar{w}}{r \partial \theta} \right)^2 \right] + \mu_{EH} \left[2 \left(\frac{\partial \bar{w}}{r \partial \theta} \right) \frac{\bar{v}}{r} - \frac{\partial \bar{v}}{r \partial \theta} \frac{\bar{w}}{r} + 2 \frac{\bar{v}}{r} \frac{\partial \bar{w}}{r \partial \theta} \right]$
ENERGY DISSIPATION	ϵ	μ_{EH}/σ_ϵ	$C_{\epsilon 1} \frac{\epsilon}{K} \mu_{EH} \left[2 \frac{\partial \bar{v}}{r \partial \theta} \frac{\partial \bar{w}}{\partial r} + \left(\frac{\partial \bar{u}}{r \partial \theta} \right)^2 + 2 \frac{\partial \bar{w}}{\partial x} \frac{\partial \bar{u}}{r \partial \theta} + \left(\frac{\partial \bar{v}}{r \partial \theta} \right)^2 \right] + C_{\epsilon 3} \frac{\epsilon}{K} \left[2 \mu_{EH} \left(\frac{\partial \bar{w}}{r \partial \theta} \right)^2 - \frac{2}{3} \nabla \cdot \vec{v} (\mu_{EH} \nabla \cdot \vec{v} + \bar{p}K) \right] + C_{\epsilon 1} \frac{\epsilon}{K} \mu_{EH} \left[2 \left(\frac{\partial \bar{w}}{r \partial \theta} \right) \frac{\bar{v}}{r} - \left(\frac{\partial \bar{v}}{r \partial \theta} \right) \frac{\bar{w}}{r} + 2 \left(\frac{\partial \bar{w}}{r \partial \theta} \right) \frac{\bar{v}}{r} + (\nabla \cdot \vec{v})K - C_{\epsilon 2} \frac{\epsilon^2}{K} \right]$

where $\nabla \cdot \vec{v} = \frac{\partial \bar{u}}{\partial x} + \frac{1}{r} \frac{\partial (r \bar{v})}{\partial r} + \frac{\partial \bar{w}}{\partial \theta}$

$C_{\epsilon 3}$ is an additional constant, presently taken as being equal to $C_{\epsilon 1}$.

Figure 3.1 Summary of Some of the Equations Solved in 3D-TEACH

In Figure 3.1, the terms K and ϵ respectively represent the specific kinetic energy of turbulence and its rate of dissipation. Thus, the code solves transport equations for K and ϵ . These arise from the turbulence model incorporated, which is the so-called two-equation, or K - ϵ , model. The turbulence model provides expressions for the Reynolds stresses in terms of calculable quantities.

Reynolds stresses can consist of two parts - a shear stress and a normal stress. The normal stress is obtained simply from the fluctuating dynamic pressures, while Boussinesq's analogy is used to relate the shear stress to the velocity gradient through an eddy viscosity μ_t . Thus for incompressible but variable density flow, the Reynolds stress can be expressed in compact tensor notation, as:

$$-\bar{\rho} \overline{u'_i u'_j} = \mu_t \left(\frac{\partial \bar{u}_i}{\partial x_j} + \frac{\partial \bar{u}_j}{\partial x_i} - \frac{2}{3} \frac{\partial \bar{u}_k}{\partial x_k} \delta_{ij} \right) - \frac{2}{3} \bar{\rho} K \delta_{ij} \quad (3.2)$$

where primes represent randomly fluctuating values, and,

$$\begin{aligned} \delta_{ij} &= \text{Kronecker delta} \\ K &= \frac{1}{2} (\bar{u}'^2 + \bar{v}'^2 + \bar{w}'^2) \end{aligned} \quad (3.3)$$

The eddy viscosity μ_t is obtained by dimensional arguments from the Prandtl-Kolmogorov definition,

$$\mu_t = \bar{\rho} \frac{C_\mu K^2}{\epsilon} \quad (3.4)$$

where C_μ is a constant of proportionality, equal to 0.09.

As the flow field is found from an effective turbulent eddy viscosity, it is convenient to also base the turbulent heat transfer on an effective thermal diffusivity.

Eddy diffusivity gives for the flux of a scalar,

$$-\overline{u'_i \theta'} = \Gamma_t \frac{\partial \bar{\theta}}{\partial x_i} \quad (3.5)$$

where

$$\begin{aligned} \theta &= \text{a scalar quantity, i.e. temperature} \\ \Gamma_t &= \text{turbulent eddy diffusivity.} \end{aligned}$$

The eddy diffusivity is found from the ratio of turbulent kinematic eddy viscosity ν_t , to a turbulent Prandtl number ϕ_t , that is specified as input.

For the eddy viscosity approach to turbulence modeling, the two-equation approach is the most general and sophisticated representation, and it is not computationally expensive. The sophistication comes from the use of differential equations to describe both the velocity scale and length scale to which eddy viscosity is assumed proportional, rather than relying on an a priori scale specification as in the mixing-length approach.

There are a number of limitations to the model. The K-equation is exact, but the modeling used in producing the dissipation equation is known to be shaky. More importantly, use of the gradient diffusion idea itself has been long challenged. There are objections to the assumption that the Reynolds stresses depend on just the local mean rates of strain, as well as to the assumption that the stresses are proportional to these rates of strain. The "constant of proportionality" C really depends on the ratio of local production and dissipation of turbulence energy, and this ratio is not actually a constant. A further weakness is the adoption of a single velocity scale at a point in the flow, although this scale can vary from point to point. The implication of a single scale is that the turbulence is isotropic. Real turbulence usually has some degree of anisotropy. Certain flows result in turbulence which is highly anisotropic; for example, flows that are swirling or which have strong curvature in the streamwise direction. The velocity and length scales have to be the same order of magnitude as the mean field motion. This is only true for flows dominated by simple shear forces; buoyancy forces, for example, have their own separate scales. It is implied that the turbulent motions have a small scale compared to that over which the magnitude of a diffusing quantity changes significantly. Most of the larger eddies in a turbulent flow do not satisfy this condition, whether the eddies are coherent or not. Thus, material can be transported by vortical motion against the gradient of temperature. Another "action-at-distance" which is removed from consideration by relying on local mean rates of strain is the effect of "flow history" on turbulence structure.

The shortcomings of the turbulence model and their relevance to the internal flows of the turbine blade will be returned to later. Two other features of the baseline code have to be described because they are of direct relevance to the surface heat transfer calculations ultimately to be made in the present application.

The first feature is related to the treatment of curvilinear surfaces, and it arises from the use of finite differences to approximate the partial differential equations to be solved.

The finite difference analogue of the differential equations is obtained by overlaying a computational mesh on the flow domain to be calculated, and obtaining the basic finite difference form of the partial derivatives for every node of the mesh from a control volume approach. The finite difference expressions, when substituted back into the differential equations, yield a set of linearized, algebraic equations (Appendix A1) for every node of the mesh. In finite difference methods, the mesh is constrained by the coordinate system used; therefore, either the coordinate system is chosen to fit the geometry, or the geometry is "discretized" to fit the coordinate system.

The 3D-TEACH code is a generalized code. Therefore, the coordinate system is fixed, and the boundary geometry is made to conform. All curvilinear surfaces, therefore, have to be represented through "stair-steps".

The use of stair-step geometries has a number of implications. First, surface areas are not correct. Thus, irrespective of physical modeling and numerical accuracy, calculation of wall shear stress and surface heat transfer on surfaces not aligned with the mesh can never be correct. Second, adequate representations of the geometry bounding the flow to be calculated usually require more computer storage than is available on the current generation of computers. Mesh refining to control numerical diffusion (to be discussed) is not therefore possible, and furthermore, in some circumstances the calculated flowfield may be influenced by the geometric representation.

In order to calculate surface heat transfer, some treatment of the wall boundary layers is necessary. The K- ϵ turbulence model, described above, involves many assumptions and has known shortcomings; in addition, it is essentially for high Reynolds numbers. It is appropriate to examine the suitability of this model for the boundary layer calculations needed.

With the no-slip boundary condition established at impervious walls, the local velocity adjacent to solid surfaces becomes low. As walls are approached therefore, the local Reynolds number of the flow based on local velocity and distance from the wall is very small, and viscous stresses become significant. The large-scale turbulence structure is likely to be directly influenced by viscosity, and the presence of the solid boundary will distort the turbulence structure.

Near to a solid surface, the turbulent eddies are of a size comparable with the distance from the surface since they cannot be larger than this distance. This physical situation is that in the regions of the flow where the turbulence is produced. In the high Reynolds number production regions, the turbulence-producing eddies are widely separated in wave-number space from regions where this energy is dissipated. In the wall region, the dissipative motions are influenced directly by the mean strain rate, so that the fine scale eddies share the anisotropy of the large scale eddies and are no longer isotropic. Characterization of such turbulence in terms of a single length and time scale is a questionable assumption. Because the Reynolds stresses fall to zero on the solid surface, very large gradients of turbulence properties exist normal to the wall. These gradients cause significant turbulent transport of energy toward the wall, so that the inner layer of the boundary layer is not in local equilibrium.

The existence of simple boundary conditions leads to simple geometries and relatively simple mathematics for boundary layers. However, the turbulence of boundary layers is just as complicated, or more so, as that of high Reynolds number flow. The two-equation turbulence model is inappropriate for boundary layers because it neglects any direct viscous effects on the turbulence structure. Most of the assumptions inherent in the two-equation model are violated, i.e., single length and time scales, local equilibrium, and homogeneity.

To take account of the direct influence of viscosity a calculation has to continue solving the conservation equations right through the viscous sub-layer of the boundary layer, where all the viscous effects on turbulence dominate. If the two-equation model of turbulence will not do, the physics could be accounted for by an appropriate higher order closure. However, higher order closures are inherently computationally expensive to use, and become almost prohibitively expensive in the case of boundary layer calculations. Because of the severely steep gradients normal to the surface in boundary layers, not less than 15 cross-stream grid nodes are required for the sub-layer and a total of 100 may be required for the complete layer.

The TEACH code was originally conceived for the calculation of complete fields, and not just boundary layer flows. For the reasons given above, an attempt to simultaneously calculate the bulk flow field and the boundary layer flows would result in an enormous computer storage requirement, and would be extremely expensive to perform. To circumvent these difficulties, the TEACH codes use special treatment at the walls.

It was argued that the main flow field is not influenced to first order by the details of the flow at the walls. The profile "universality" feature of boundary layers was then invoked to provide an easy description of the flow near solid boundaries. A "law of the wall" approach was used to conveniently link the wall to the near-wall nodes of the finite difference solution grid. This is done very inexpensively. The approach is described in Appendix A2.

The wall-function method is a standard procedure in all the TEACH codes, and is satisfactory for most purposes. However, deviations from "universal" laws do arise, and the wall-function approach is not valid for separated flow regions, flows with large density gradients, boundary layers with strong curvature, and most importantly, large pressure gradients in the direction of flow.

It should be appreciated that the TEACH code is not analytically exact but is an approximate solution procedure. Approximations are introduced at several stages. However, of particular importance is the use of finite differencing to discretize the equations to be solved.

The accuracy of a differencing scheme can be judged from the order of the terms of an equivalent Taylor series that have been retained in the expansion. Unfortunately, the requirements of numerical stability are opposite to those of accuracy with respect to these terms. The spatial differencing of the convective terms of the conservation equations in an Eulerian coordinate system can result in numerical diffusion occurring. Use of a higher order differencing scheme eliminates or significantly reduces this diffusion. However, use of central differencing, for example, introduces an oscillatory behavior into the solution. This "wiggling" can lead to nonphysical behavior (Ref. 4). The use of an upwind or donor-cell technique eliminates wiggling; however, this is accomplished by the introduction of a diffusive-like term into the difference equations. Thus, while "numerical damping" suppresses oscillation, it leads to significant additional diffusion of the convected parameter. Therefore, a severe restriction can be placed on the quality of quantitative prediction (Ref. 5).

It can be argued for use of upwind differencing in regions where convection strongly dominates streamwise diffusion, that the local upstream values of the field variables are swept downstream virtually unchanged, whereas in high-diffusion regions the form of the relatively small convection terms is not important. In regions where the two transport mechanisms are comparable, a switch to more accurate central differencing for convection or use of a suitably weighted combination of central and upstream differencing can be used.

This somewhat narrow view of complex flows has led to the appearance and use of a popular and successful hybrid central/upwind differencing scheme (Ref. 6). This scheme is currently used in the TEACH codes described in Appendix A1. The scheme uses central differencing for convection and diffusion fluxes when the absolute value of the Peclet number for the control volumes existing about grid nodes is less than, or equal to, two; upwind differencing for convection fluxes and neglect of diffusion fluxes is used otherwise. Peclet number defines the relative importance of convective and diffusive transport.

To successfully use the hybrid differencing scheme for complicated flows, care must be taken in establishing the computational grid upon which the calculations are performed. The approximations of the algebraic expressions used to represent the partial differential equations becomes asymptotically exact as the distance between the nodes set up by the grid, and used to link the algebraic expressions, is reduced. In the limit, the number of nodes can be increased until an asymptote to the solution to the differential equations is achieved. In practice, this increase is limited by computer storage and the cost of the calculation. However, it is not just the number of nodes that are used which is important in determining the accuracy of a solution, but also the distribution of those nodes within the flowfield to be determined (Refs. 7 and 8). This nodal distribution is important because whenever curvature of the flow in the streamwise coordinate direction exists, a truncation error arises in the solution (Ref. 9). There is also a problem in multidimensional flows of streamline-to-grid skewness (Ref. 10). With upwind differencing, these effects start to have a damaging effect on solution accuracy when the Peclet number exceeds two.

It has been concluded (Ref. 3) that the hybrid finite differencing scheme, although yielding physically realistic solutions in all circumstances, introduces excessive numerical diffusion for many two-dimensional flows, and for all three-dimensional flows. This is because present computer storage is not sufficient to permit local adjustment of the grids as described above, except for the simplest of flows. Thus, the solution accuracy is presently controlled by the numerics, rather than the hierarchy of physical modeling.

3.3 Suitability of Baseline Code

The salient features of the baseline code have been described. Some limitations and shortcomings were highlighted. The suitability of the baseline code for modification to a form for the intended application is now discussed. (The modifications to be made are illustrated in Figure 3.2.)

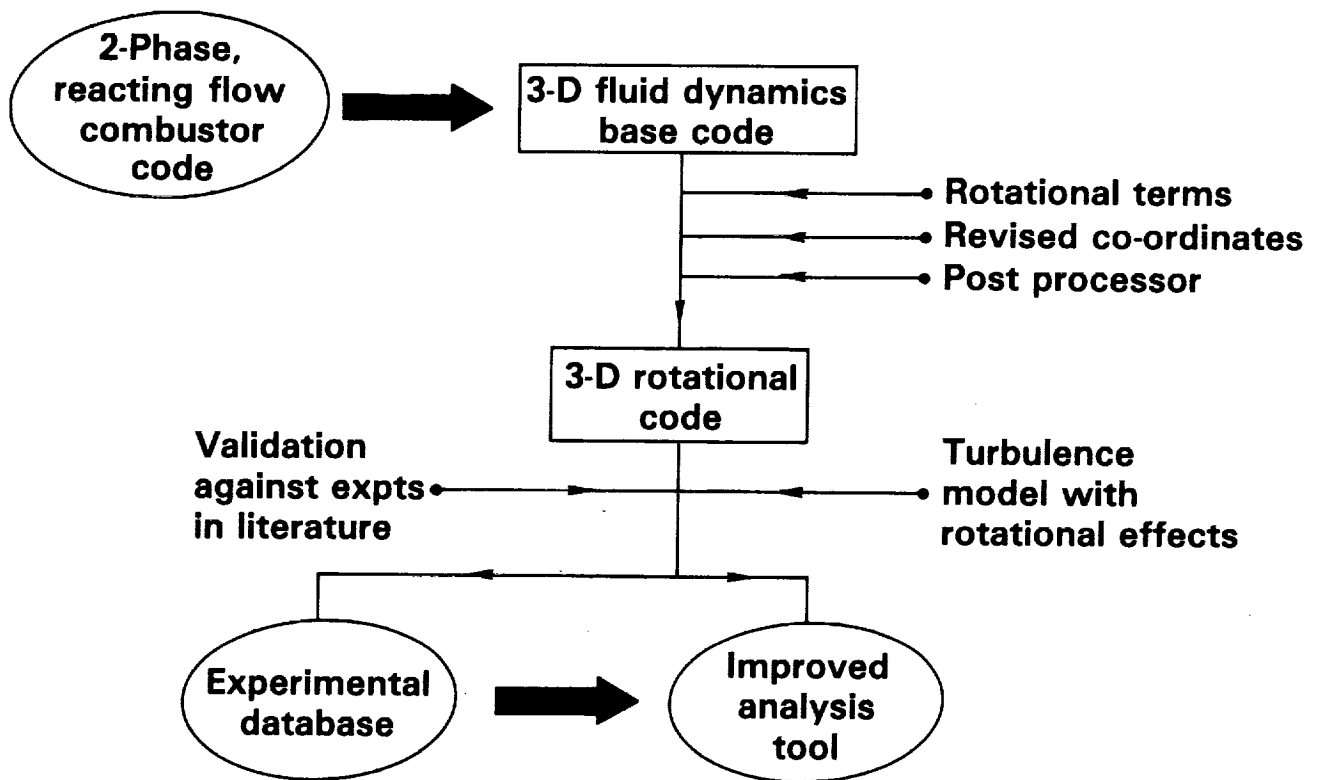


Figure 3.2 Modification Procedure to Develop Code for Turbine Blade Analysis

There are four features of the baseline code that give rise to concern for application to turbine blade internal flows:

1. Suitability of the turbulence model for calculation of the bulk flow field;
2. Stair-step treatment of curvilinear surfaces;
3. Use of wall functions to represent boundary layers;
4. Effects of numerical diffusion.

3.3.1 Turbulence Model

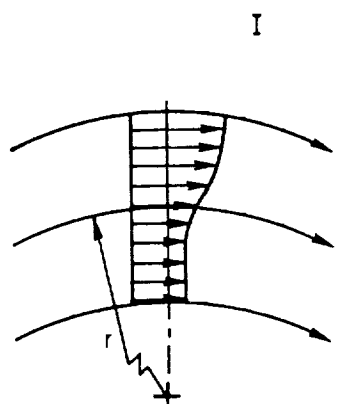
It has been found experimentally that general streamline curvature in the plane of the mean shear produces large changes in the turbulence structure of the shear layers. These effects can occur not only in boundary layers but in any shear layer where the streamlines have a component of curvature in the plane of the mean shear. Turbulence in the boundary layer on a highly convex surface may be nearly eliminated, while on highly-concave surfaces momentum transfer by quasi-steady longitudinal vortices dominates the ordinary turbulence processes. Thus, the changes in turbulence are not only quantitative but also qualitative. The changes are usually an order of magnitude more important

than normal pressure gradients and other explicit terms appearing in the time-mean equations of motion; this is not so for flows dominated by secondary flows. This effects on local Reynolds stresses do not appear as soon as the curvature is imposed. This means flow "history" effects are important.

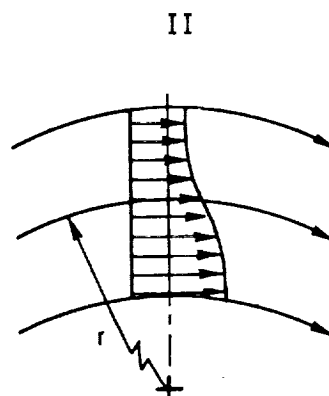
The streamline curvature is a distortion that gives rise to extra rates of strain in addition to that due to simple shear. The Reynolds stresses are changed by a factor $(1-\alpha s)$ where $5 \leq \alpha \leq 15$, and

$$s = \bar{u}/r/(\partial \bar{u}/\partial r)$$

Now, consider the flows sketched below where in the first case the angular momentum increases outward from the flow center of curvature, and in the second case where it decreases.



Angular momentum
increasing with radius



Angular momentum
decreasing with radius

It can be appreciated from the equations above that for the first case the Reynolds stress is reduced, the turbulence is suppressed, and the flow curvature is stabilizing. For the second case, the turbulent motion is strongly augmented, and the large eddies develop into longitudinal vortices.

The two-equation turbulence model with its assumption that the one-point, two-variable correlations for Reynolds stresses and turbulent scalar fluxes are directly proportional to the mean gradients implies that the eddy viscosity is isotropic. The model therefore displays equal sensitivity to both primary and secondary strains; certainly it also has no way to account for flow "history." The flow behavior is not well-predicted by such mean-field closure methods.

The flow through a blade cooling passage (see Figure 2.1) will involve at least one 180-degree sharp turn, and more with multi-pass configurations. Flows in ducts with curvature produce secondary flow motions induced by the transverse pressure gradient due to lateral curvature of the main flow. In addition, secondary motions arise for turbulent flows in non-circular ducts due to Reynolds stress gradients in the cross-stream direction, particularly for thick inlet boundary layers. As the flow proceeds through the passage, the effects become more pronounced. The flow curvature produced by the turns will also

result in the stabilizing and destabilizing changes in turbulence structure described above. However, in this case the turns are likely to be so sharp that the cross-stream flow is probably dominated by mean pressure forces (Ref. 11), so that the effects of the turbulence model on mean profiles should be small.

For the model to be used in the present experiments (Figure 3.3), the passage high aspect ratios in the flow direction and the modest curvatures used suggest that boundary layer effects could be quite important. If this is so, the code could not be expected to do well with the isotropic $K-\epsilon$ turbulence model.

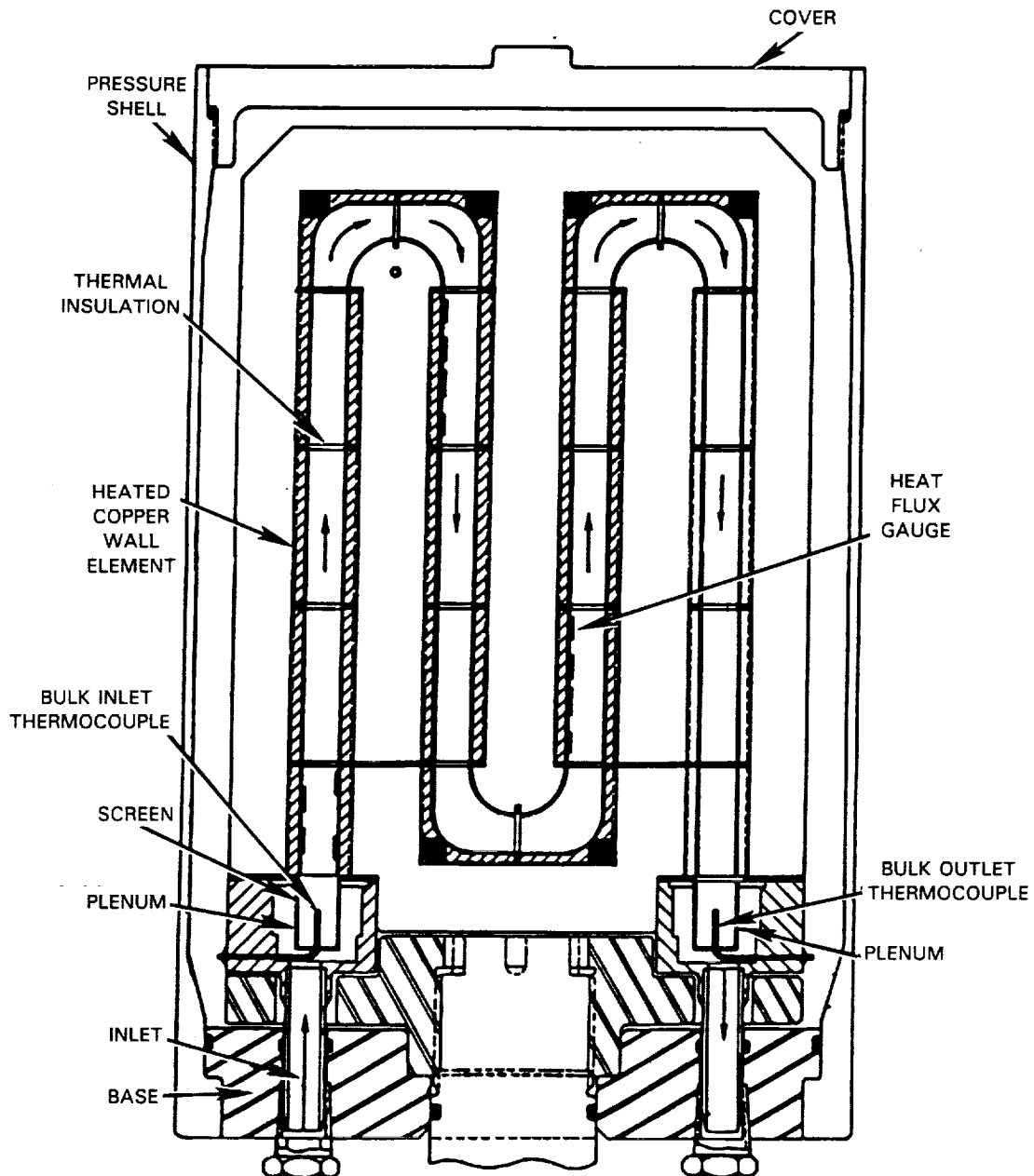


Figure 3.3 Coolant Passage Heat Transfer Model

3.3.2 Treatment of Curvilinear Surfaces

The stair-step representation of the modest curvatures shown for the model in Figure 3.3 will introduce a much larger momentum deficit into the flow than would exist physically. If the flow in the model were to separate in leaving the turns, this deficit would not be so critical. However, the turns are so modest that significant flow separation on the inner surface of the turn is unlikely to take place. This being so, the boundary layers in the legs away from the turns will be calculated incorrectly from those actually existing.

The flow in an actual blade (see Figure 2.1) is likely to be better calculated than that in the present model. This is because the baffle in a real blade is much thinner than in the model, such that a rectilinear representation of it does not introduce any significant momentum deficit into the flow. (The turning vanes suppress separation.)

3.3.3 Use of Wall Functions to Represent Boundary Layers

The flow through the model has large density gradients, significant pressure gradients in the direction of flow, boundary layers with moderate to strong curvature, and possibly small regions of separated flow. These are all situations in which the wall function approach could be expected to fail. However, the significance of such failures is likely to be overshadowed by the limitations of anisotropic turbulence, the crude representation of the bend curvatures, and the effects of numerical diffusion.

3.3.4 Numerical Diffusion

The calculations to be made are elliptic in character. Therefore, the imposed downstream boundary conditions have to be sufficiently removed from the region of interest such that they do not influence the calculation in this region. For the model shown in Figure 3.3, this means that to obtain good calculations of the flow in the first two legs of the passage, three legs must be calculated, and so on. Thus, the calculation domain becomes extensive. An extensive calculation domain can demand a large number of grid lines to cover it with an acceptable degree of resolution.

The maximum array size currently available on Pratt & Whitney's computers is of the order of 30x40x40, or 48,000 nodes. A considerable number of grid lines are consumed in representing the turns with stair-steps and in defining the flow passages. The three-dimensional grid necessary to adequately represent and fully cover a complex and extensive calculation domain quickly consumes the available computer storage. Thus, there is little opportunity to refine the mesh to minimize numerical diffusion, as is possible in two-dimensional calculations (Ref. 12). Therefore, considerable numerical diffusion will inevitably be present in the calculations. This is a problem with all three-dimensional viscous flow calculations made on the current generation of general purpose computers (Refs. 3 and 13).

3.3.5 Summary

The selected baseline code has the basic features essential for the stated objectives. It is therefore a suitable vehicle for modification for rotational effects. However, there are limitations and shortcomings to the code that will

impact the quantitative accuracy achievable. Fortunately, the structure of the code is modular so that some of the deficiencies may easily be remedied as better models come along. This applies specifically to the turbulence model and the finite differencing scheme. Also, it is anticipated that computer storage will soon cease to be a problem (although the cost of solution will then need to be addressed by speeding up the calculation procedure). The problem of a three-dimensional curvilinear representation is much more difficult, and a near-term answer is not at hand.

3.4 Modifications for Rotation

The equations to be solved are the three momentum equations, the continuity equation, the energy equation, an equation of state, and the transport equations for K and ϵ . The modifications to be made involve incorporating rotational effects. If the blade is placed at radius R and is rotated with steady angular velocity Ω , additional inertial accelerations will arise. These are due to Coriolis and centrifugal forces, $2\bar{\rho}\bar{\Omega}\bar{V}$ and $\bar{\rho}\Omega^2 R$ respectively, where V is the bulk flow velocity in the cooling passage, and where the overbar denotes a time-mean quantity as before and $\bar{\rho}$ denotes a vector quantity.

The coolant passages, shown in Figure 3.3, are most conveniently represented by a Cartesian coordinate system x, y, z , fixed on the "blade." The additional terms due to rotation are most conveniently added to the general equation (Appendix A1, rewritten in Cartesian form) as additional source terms, S_{θ}, Ω . Therefore, the Coriolis and centrifugal forces must be derived in terms of the rotating coordinate system shown in Figure 3.4.

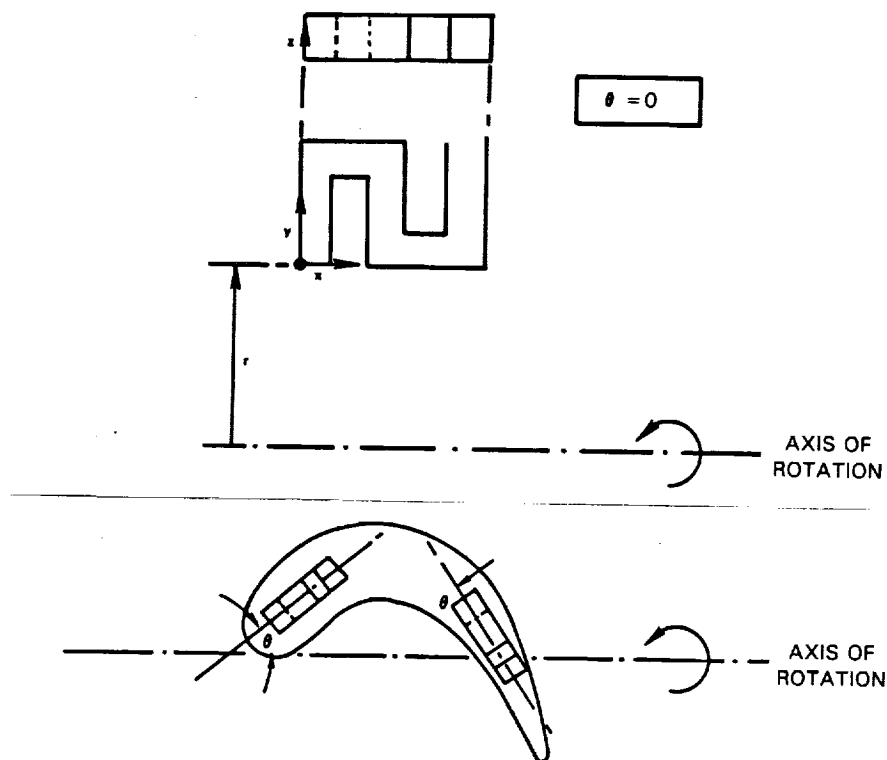


Figure 3.4 Coordinate System for a Rotating Frame of Reference

Coriolis forces can contribute directly to the development of secondary flows and indirectly to affect the turbulence structure. The rotation has a stabilizing-destabilizing effect on turbulence, similar to that described for bulk flow curvatures described above. It has been observed experimentally (Ref. 14) in rotating channel flow that on the trailing (suction) side rotation suppressed turbulence production and on the leading (pressure) side rotation caused the appearance of Taylor-Gortler-type vortices.

There is no contribution to the continuity equation. The contribution to the momentum equations is the sum of the Coriolis and centrifugal terms. The velocities Ω and ∇ are resolved into their components, $(i\Omega_x + j\Omega_y + k\Omega_z)$ and $(iu + jv + kw)$ respectively, to give the additional sources $S_{\phi, \Omega}$. Unit vectors in the major coordinate directions are represented by i, j and k . The momentum equation is shown in Appendix A3, while the sources are given in Table I.

TABLE I.- ADDITIONAL SOURCE TERMS DUE TO ROTATION

Equation	ϕ	$S_{\phi, \Omega}$
x-momentum	\bar{u}	$\bar{\rho} (\bar{v} - z\Omega_x + x\Omega_z)\Omega_z - \bar{\rho} (\bar{w} - x\Omega_y + y\Omega_x)\Omega_y$ $+ \bar{\rho} \bar{u} - \Omega_z - \bar{\rho} \bar{w}\Omega_y$
y-momentum	\bar{v}	$\bar{\rho} (\bar{w} - x\Omega_y + y\Omega_x)\Omega_x - \bar{\rho} (\bar{u} - y\Omega_z + z\Omega_y)\Omega_z$ $- \bar{\rho} \bar{u} - \Omega_z - \bar{\rho} \bar{w}\Omega_x$
z-momentum	\bar{w}	$\bar{\rho} (\bar{u} - y\Omega_z + z\Omega_y)\Omega_y - \bar{\rho} (\bar{v} - z\Omega_x + x\Omega_z)\Omega_x$ $+ \bar{\rho} \bar{u}\Omega_y - \rho v\Omega_x$
enthalpy	\bar{H}	$-\left\{ \bar{\rho} \bar{u} [\Omega_y (\Omega_x y - \Omega_y x) + \Omega_z (\Omega_x z - \Omega_z x)] \right\}$ $-\left\{ \bar{\rho} \bar{v} [\Omega_x (\Omega_y x - \Omega_x y) + \Omega_z (\Omega_y z - \Omega_z y)] \right\}$ $-\left\{ \bar{\rho} \bar{w} [\Omega_x (\Omega_z x - \Omega_x z) + \Omega_y (\Omega_z y - \Omega_y z)] \right\}$

Similarly, there is a stagnation enthalpy term $\bar{\rho} \nabla^2 R$ that gives rise to a source term in the energy equation, as Table I shows.

No additional terms arise in the K-equation. An assumption of the turbulence model, that the turbulence is in equilibrium so that production and dissipation of turbulence kinetic energy are in balance, is invoked to infer that there are no additional terms in the ϵ -equation either. This means that although secondary flow development due to Coriolis forces should be calculated through the modified equations of motion, the effects on the turbulence structure will not be calculated.

The passage angle θ in Figure 3.4 is accounted for in the resolving of Ω into its components. The position vector r in Figure 3.4 is automatically taken care of by working in terms of the angular velocity Ω .

Details of the derivations are given in Appendix A3. Buoyancy effects are not accounted for as they should be small in this application.

3.5 Exploratory Calculations

Following debugging of the programming changes to incorporate the rotational terms shown in Table I, it was considered desirable to establish if the modifications gave a calculated flow behavior that was at least physically realistic. To this end, a simplified passage geometry was considered, as shown in Figure 3.5.

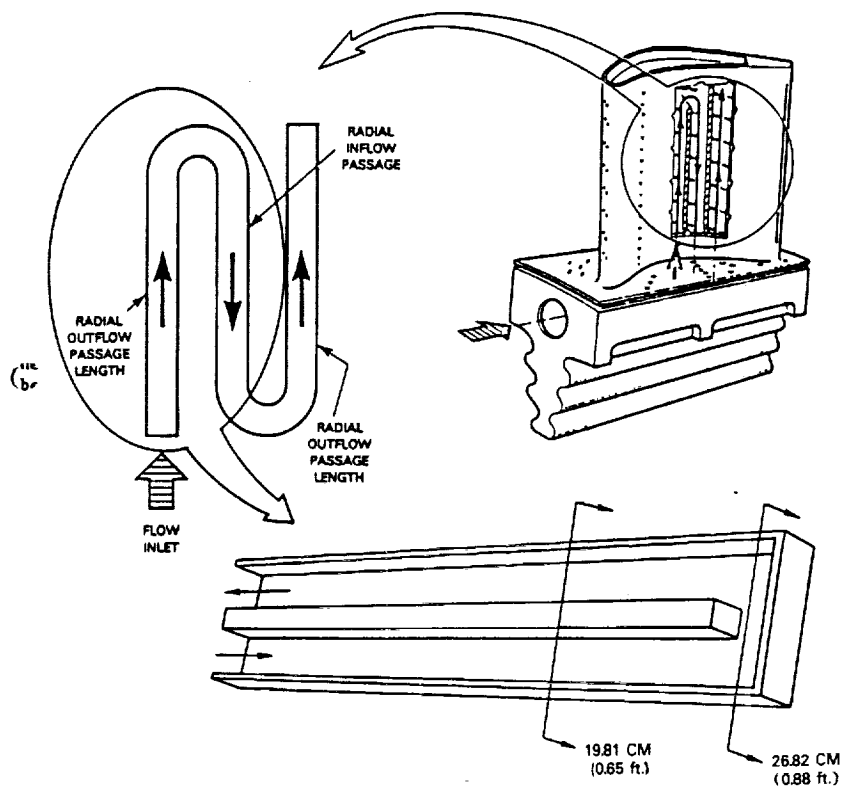


Figure 3.5 Schematic of Coolant Passage for Exploratory Calculation

In the simplified geometry a single outflow and inflow leg was considered. The grid used (33x11x5) is shown in Figure 3.6, where it is seen to be extremely coarse. However, this grid utilized the biggest virtual machine then available on Pratt and Whitney's computer system (4 Megabytes; currently 12 Megabytes). It illustrates the current difficulties associated with three-dimensional calculations. The calculations that result from this grid have to contain large amounts of numerical diffusion and are certainly not grid-independent. Although the flow resolution attainable with this grid is also poor, the calculations are considered adequate to ascertain whether or not the modified code is behaving as it should.

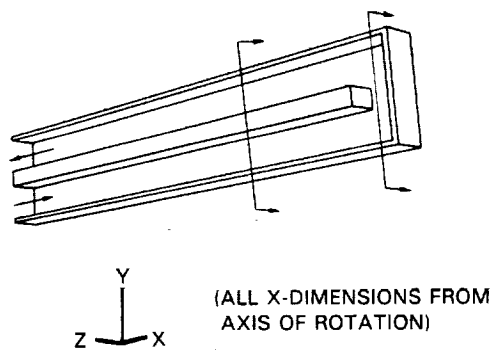
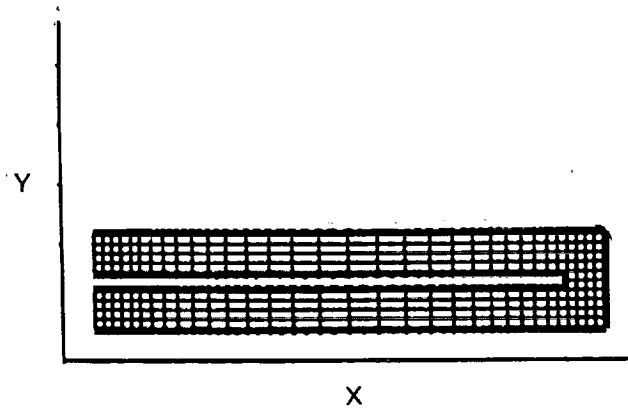
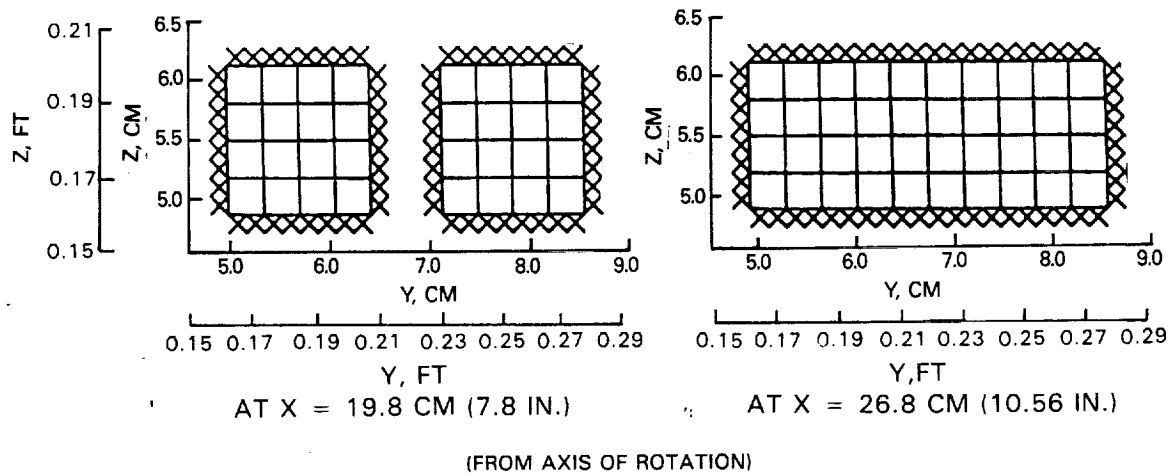


Figure 3.6 Grid for Exploratory Calculations

The operating conditions for the exploratory calculations are shown in Table II.

TABLE II.- OPERATING CONDITIONS FOR EXPLORATORY CALCULATIONS

Passage cross-section	:	1.27 x 1.27 cm	(0.5 x 0.5 inch)
Passage length	:	15.24 cm	(6 inches)
Inlet air temperature	:	15.9°C	(60°F)
Air pressure	:	10 bar	(10 atmos)
Coolant mass flow rate	:	0.0077 kg/s	(0.017 lb/sec)
Wall temperature	:	94°C	(200°F)
RPM	:	600	(baseline)
Reynolds number	:	30,000	
Rossby number	:	0.174	

The table represents a "smooth-wall" test condition for the model of Figure 3.3. The passage is rotated about the y-axis.

The results of the calculations are presented as flow visualizations by means of streaklines. Streaklines are the computational analogue of fine aluminum tracer particles momentarily illuminated by a finite-thickness sheet of laser-light as used, for example, in water tunnels. Streaklines are not streamlines, nor are they vectors, although they have some characteristic of both. The TEACH code can generate either random streaklines or uniform lines of origin; in the present case the random mode is used.

Figure 3.7 shows the flow in the passage at cross-sections of 19.8 cm (7.8 inches) and 26.8 cm (10.56 inches) from the axis of rotation for a rotational speed of 600 RPM. In Figure 3.8, flows in the same sections are compared for 0, 60, 600 and 1900 RPM, and the flow through the complete passage length (x-y plane) is also shown.

With reference to Figure 3.7, the development of secondary flows due to the influence of Coriolis forces can be seen. In the outflow (away from the axis of rotation) leg of the passage, a pair of counter-rotating vortices develop. The vortex centers are shifted slightly from the centerline of the leg towards the pressure side, but the size and strengths of the vortices are about equal. As the vortex pair enters the turn, their rotational velocity is overcome and flow changes direction as mass is forced to the pressure side of the turn. The flow entering the passage inflow leg from the turn is therefore forced into a right-angled corner. As it escapes from the corner to begin flowing down the inflow leg (toward the axis of rotation), the air has no choice other than to establish a single vortex. The action of the turn is thus to coalesce the vortex pair formed by Coriolis forces into a single vortex, completely filling the passage inflow leg. Figure 3.8 demonstrates that increasing rotation

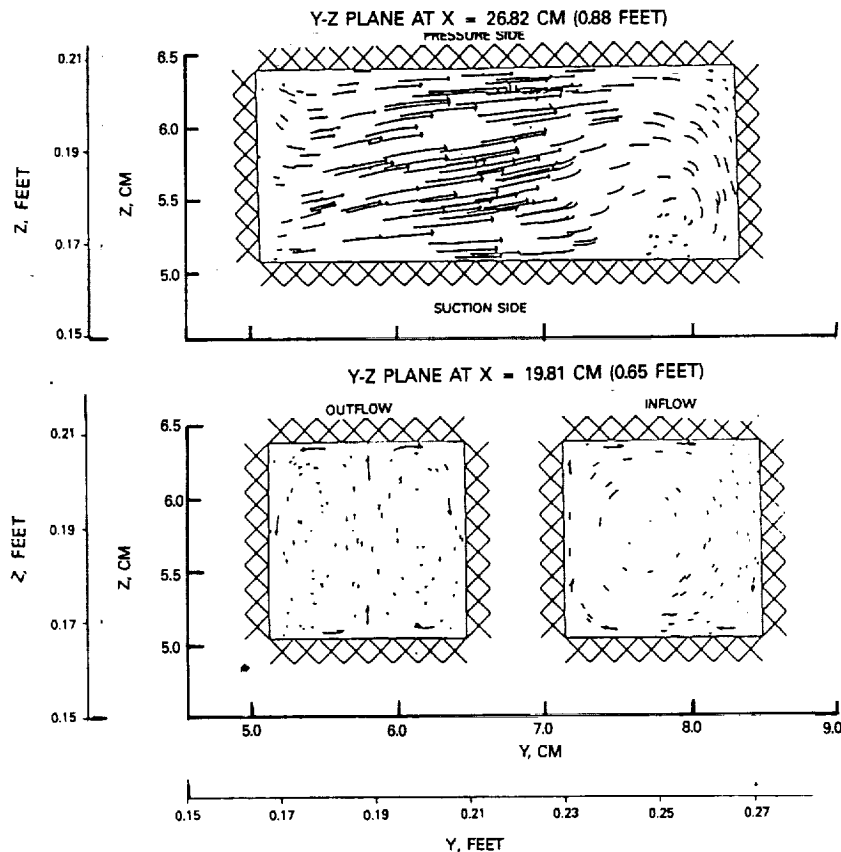


Figure 3.7 Test of Momentum Equation - Flow Visualization

increases the strength of the single vortex in the inflow leg leaving the turn. However, the double vortex system begins to re-establish itself in the inflow leg as the flow proceeds toward the axis of rotation. The pair of vortices so-formed is initially no longer symmetrical as the vortex originating from the coalesced pair from the outflow leg dominates. With rotation there is no evidence of flow separation in the inflow leg immediately following the turn. This is due to the vortex motion.

These results are intuitively correct (Ref. 15) and show that the code is behaving soundly in a qualitative sense. Consistency checks were also carried out on this geometry to establish that the same results were obtained for all orientations.

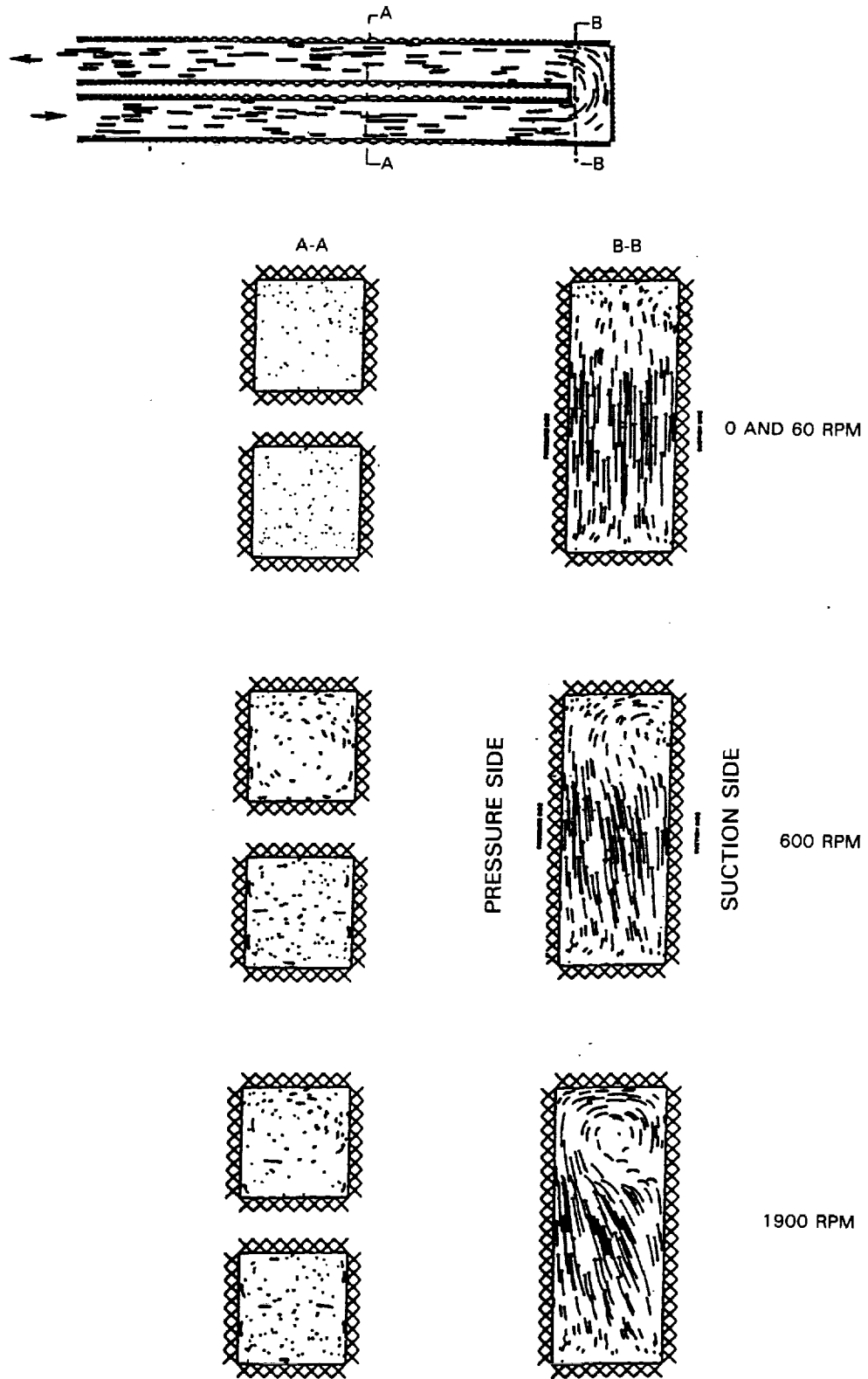


Figure 3.8 Streakline Cross Sections for a Range of Rotational Speeds

4.0 EXPERIMENTAL DATA

Although the modified code appeared to be performing in expected fashion as a result of the exploratory calculations, some form of quantitative verification was desirable before committing to extensive calculations for the test geometry shown in Figure 3.3. In principle, the verification testing should be conducted for geometries as simple as possible, and against experiments that explore the overall relevant physical processes one at a time and not simultaneously. These two conditions are essential so that the effects of geometric modeling can be separated from the physical modeling, and so that shortcomings can be identified with a specific physical model. Ideally then, experiments of simple isothermal flow with rotation, stationary isothermal flow in sharp 180° bends, heat transfer in simple flow with rotation, and, heat transfer in stationary, sharp, 180° bends, would represent a desirable set of experiments against which to verify the performance of the modified three-dimensional code.

4.1 Benchmark-Quality Experiments

A series of experiments was defined above that would provide a suitable verification. However, to be useful for this purpose, an experiment must also satisfy additional criteria. A qualified experiment that does satisfy these additional criteria is termed a benchmark-quality experiment. Benchmark-quality experiments are difficult to find.

A benchmark-quality experiment is defined as follows:

1. Minimum necessary flow dimensionality. Experiments in which the flows can be represented as one or two-dimensional are desired. Three-dimensional flow situations will be used only when specifically testing three-dimensional flow modeling capability.
2. Well-behaved flows. Flows in which instabilities, periodicity, or changes in gross behavior occur as flow conditions change are avoided. For example, flows in which the location of reattachment points of separated flow regions could undergo significant shifts as Reynolds number is changed over the range of interest should be avoided (unless, of course, this is the flow feature being tested).
3. Continuous variation of test parameters. Experiments should be conducted over a wide range of values of test parameters rather than at isolated sets of conditions.
4. Known boundary conditions. Entrance and exit flow profiles must be specified as completely as possible. Velocity, temperature and pressure profiles are required. Concentration profiles are important for reacting flow experiments; initial droplet size, velocity and spatial distributions are required for two-phase flows. For assessing turbulence models, initial profiles of turbulence intensity and integral length scale are vital.

5. Progression in flow complexity. The ideal experiment for assessing flow models would consist of a series of experiments of increasing flow complexity such that the credibility of the analysis can be checked in stages. For example, the initial tests for a given flow geometry should be single-component, isothermal flow visualization tests which could be used to check the fluid mechanic aspects of the analysis. Two-component gaseous flows could be used to check the ability to predict mass diffusion; thermal diffusion could be checked using gases introduced with different initial conditions, reacting gaseous mixtures the next stages. A similar progression of experiments with two-phase flows can be constructed.
6. Extensive instrumentation. Flow mapping experiments in which nonintrusive techniques are used to characterize flows throughout the chamber volume are highly desirable. Estimates of instrument precision should be made and possible sources of bias identified. Redundant measurements performed with different instruments are valuable.

For the present purposes, extensive and complete verification is not the objective so that a full-range of experiments cannot be considered. Despite this, those experiments chosen should conform to the definition as closely as possible. Of course, it is most unlikely that any single experiment will conform exactly to the ideal, so that some compromises have to be accepted.

4.2 Selected Experiments

An exhaustive literature survey was not made, and a total of only three experiments was selected. Two of these experiments explored rotational effects in isothermal flow and also covered the effects of passage aspect ratio (Refs. 17 and 18). The third experiment was concerned with heat transfer in a sharp, 180° bend, and had no rotation (Ref. 19). Although a more extensive comparison against experiments in the literature, and a literature survey would have been useful, such a comprehensive verification and survey were not a part of the present contract.

4.2.1 Effects of Rotation

Calculation of the effects of rotation on isothermal flow along a duct was investigated through the experiment of Moon (Ref. 17). Although carried out some years ago, it seems to have been a well-conducted experiment, and closely fits the description of a benchmark-quality experiment.

The test-duct was rectangular, with a cross-section of 15.24 x 7.62 cm (6 x 3 inches) and a length of 1.83 m (72 inches). Air was supplied uniformly at one end with a mean velocity of 16.5 m/s (54 ft/sec). The duct was arranged horizontally with the major axis of the cross-section vertical, and was rotated horizontally at a steady speed of 165 RPM about an axis passing through the center of the duct and perpendicular to the main flow direction. The arrangement is shown in Figure 4.1. The entering air was delivered through a contraction and the supply duct contained honeycomb and screens to deliver a flat inlet velocity profile unaffected by rotation. The rotating test duct was contained within a cylindrical box to minimize disturbances.

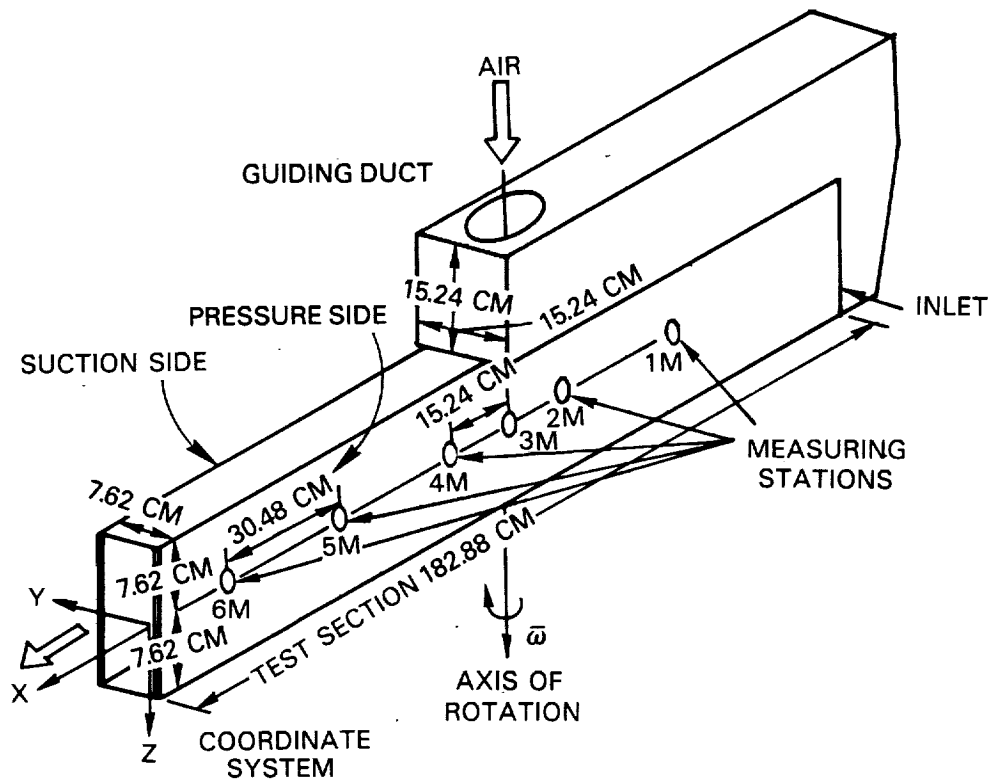


Figure 4.1 Rotational Passage of Moon's Experiment

Measurements were confined to the horizontal centerline at stations shown in Figure 4.1. The first station (1M) was located 0.46 m (1.5 feet) from the duct inlet, and the other stations were 0.30 m (1 foot) apart. A flattened hypodermic tube was used to take profiles of total pressure across the minor axis of the duct. Six static pressure taps were provided on each side-wall. Wall shear stress measurements were made by means of Preston tubes. Fluctuating velocities and Reynolds stress profiles were measured with hot-wires. At the inlet, horizontal profiles of mean and fluctuating axial velocities were provided.

4.2.2 Effects of Duct Aspect Ratio With Rotation

Moon's experiment was conducted with a duct aspect ratio of 2:1. Moore (Ref. 18) used essentially the same apparatus to explore the effects of duct aspect ratio with rotation. This experiment was considered significant because passage aspect ratio is an important design parameter in practice.

The modified duct section of the apparatus is shown in Figure 4.2. The spacing between the vertical side-plates now forming the duct was set to 1.9 cm (0.75 inch) for passage aspect ratios (height/width) of 1:1, 4:1, and 7.33:1; while a value of 3.81 cm (1.5 inches) was used for an aspect ratio of 0.5:1. The 1.9 cm (0.75 inch) duct width allowed fully-developed flow to be established.

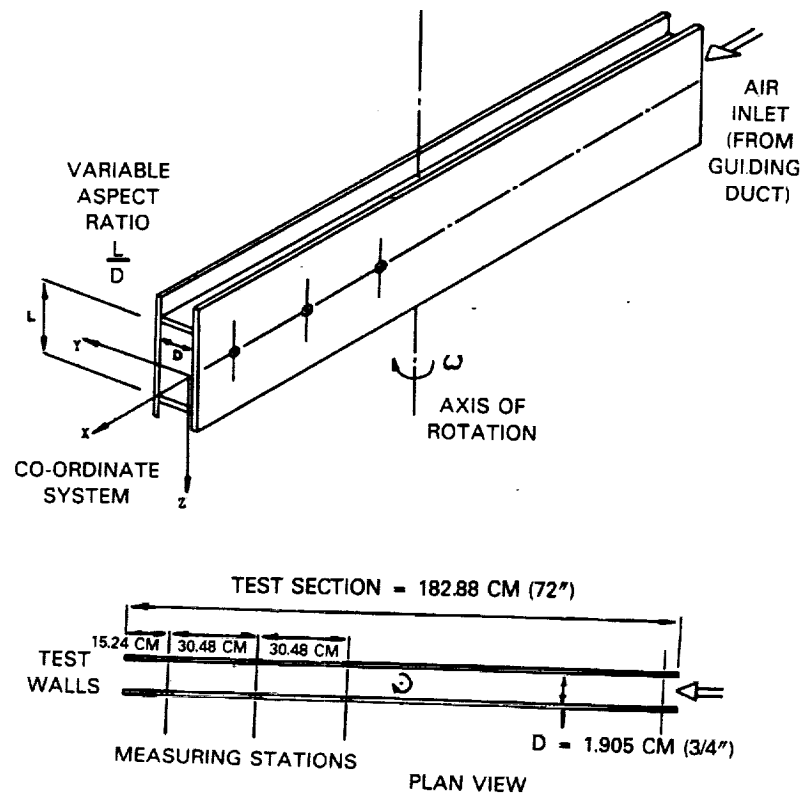


Figure 4.2 Schematic of Moore's Test Section to Explore Aspect Ratio

4.2.3 Surface Heat Transfer in a Sharp Bend

Pratt and Whitney has sponsored a program of work at Arizona State University to provide data on pressure losses and heat transfer in sharply turning passages. Some of this material has been utilized for the present purposes (Ref. 19).

Figure 4.3 shows the arrangement of the flow passage, and it can be seen that the 180° turn is really sharp. This is as it is in a real blade (see Figure 2.1), and not as it is in the model to be tested as part of the present contract (see Figure 3.3). The turn also can involve either contractions ($W1/W2 > 1.0$) or expansions ($W1/W2 < 1.0$) of the passage. Passage aspect ratio can be varied as well, as can the end-wall clearance beyond the partition forming the sharp turn. The apparatus is stationary. The overall passage consists of an unheated plenum chamber provided with screens to ensure flow uniformity, the heated test-section, and an unheated exit region. The test section walls are built of individual insulated copper segments to provide a uniform surface temperature on the segment, and each segment is provided with an individual foil-heater on its rear-face. Figure 4.4 shows the segments and the five regions of uniform temperature that result. The top and bottom walls are mirror-images of each other.

The apparatus was allowed to reach equilibrium before readings were taken. Air mass flow rate, air pressure drops, electrical power inputs, and segment temperatures were recorded. Heat losses to the background were determined for each configuration tested.

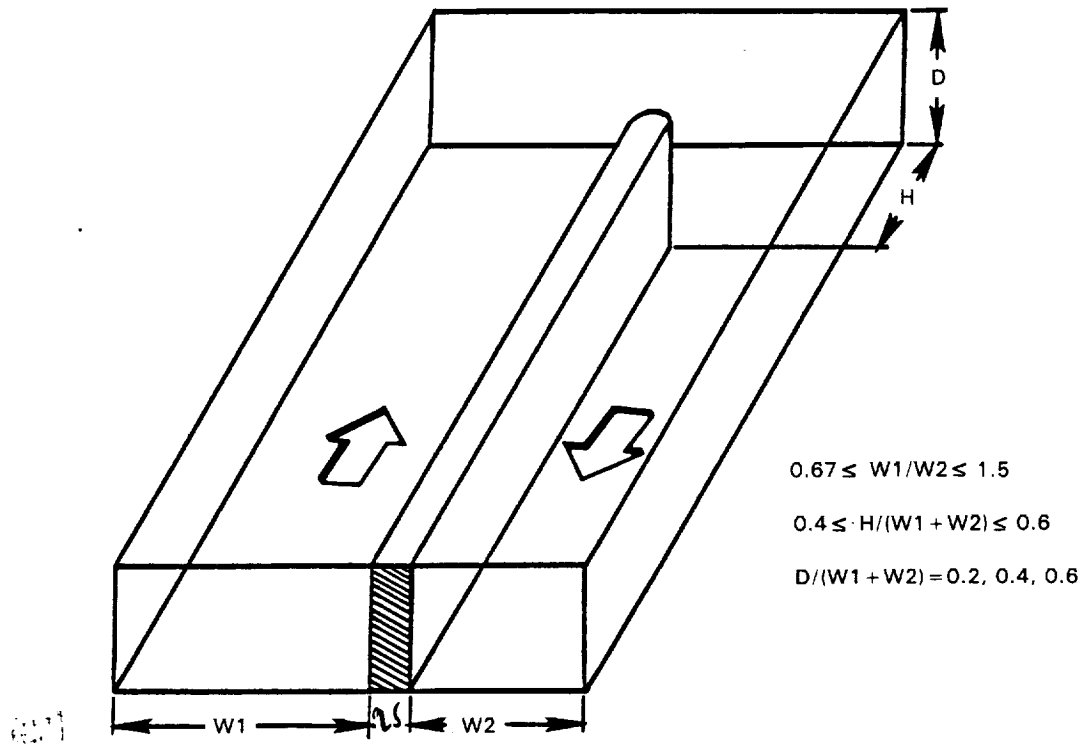


Figure 4.3 Flow Passage for Heat Transfer in a Sharp Turn

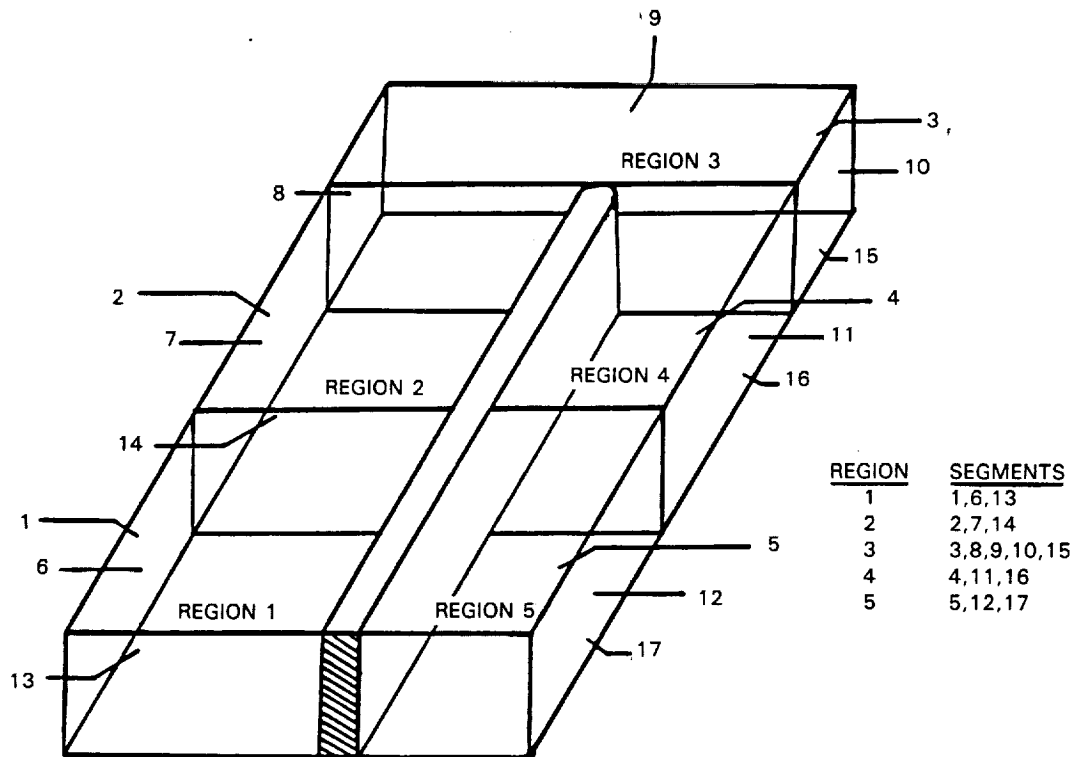


Figure 4.4 Definition of Heated Test Sections for Heat Transfer Measurements

5.0 COMPARISONS OF CALCULATIONS AND MEASUREMENTS

5.1 Effects of Rotation

5.1.1 Computational Set-Up

The computer storage capacity available at the time the calculations were made was represented by a 4 Megabyte virtual machine. For this machine, the code was configured with a 30x20x20 maximum array size. Almost the maximum allowable grid was used within this capacity, 30x20x14. Cells in the x and z-coordinate direction were arranged to have an aspect ratio of unity; in the y-coordinate direction the grid lines were arranged to enhance the view obtained close to the suction and pressure sides of the duct, where the boundary layers of interest were. With this grid the solution cannot be considered grid independent and must be viewed with a remembrance of the numerical diffusion that is present. The resolution of the boundary layers cannot be considered adequate, and it should be recalled that the wall-function approach is being used.

The measured inlet profiles at an RPM of 165 for mean and fluctuating velocities were used as starting conditions. The usual assumptions concerning hydraulic diameter were made for a length scale of turbulence.

5.1.2 Flow Visualization

Although the experiment did not provide any visualization of the flow, the code does provide such a convenience. Since a sound appreciation of the basic flow patterns is essential for a comprehensive understanding of flows as complex as those under consideration, this aspect of the experiment is visited here.

Once again, the flow visualization technique used in the calculations is the random streakline. Figure 5.1 shows the calculated streaklines in a cross-section of the duct at two axial locations along it, equidistant from the axis of rotation. The formation of the counter-rotating vortex pair due to Coriolis forces can be observed. The strength of these vortices increases with distance down the duct because the sign of the Coriolis force remains the same on either side of the axis of rotation. Rotation of the duct causes a progressive shift of the vortex centers from the mid-line of the duct toward the pressure-side of the duct. This does not change as the axis of rotation is crossed. However, since the developing vortices are still relatively weak on the inflow side (flow toward the axis of rotation) of the duct, this shift only becomes evident on the outflow side (flow away from the axis of rotation).

The results observed are in agreement with the flow visualization of Reference 20 and the calculations of Reference 21.

The calculations agree quite well with the measurements of mean axial velocity profile and indicate the almost constant boundary layer thickness on the wall that is the pressure side on the outflow side of the duct, and the thickening on the opposite wall. Since the turbulence model does not recognize the extra strains associated with rotation, the calculated effect is due entirely to secondary flow development.

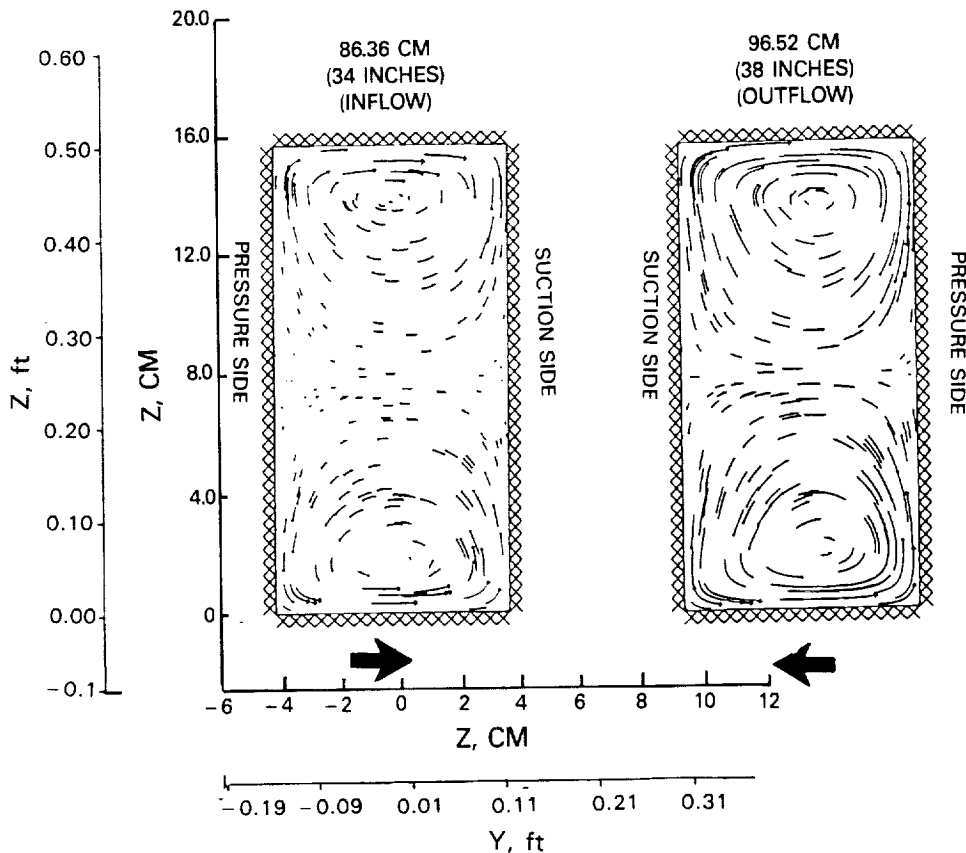


Figure 5.1 Calculated Secondary Flow Patterns Due to Coriolis Forces With Rotation (Moon's Experiment)

5.1.3 Mean Velocity Development

A comparison of the calculated and measured development of mean axial velocity profiles at the duct centerline is contained in Figure 5.2.

On the pressure side of the duct, the Coriolis forces increase turbulent momentum exchange in the boundary layer and cause a thinner boundary layer. On the suction side they inhibit momentum exchange thereby causing a thicker boundary layer. The secondary flow development shown in the cross-sectional flow visualization, also causes low momentum fluid to be transferred to the suction side resulting in a thicker boundary layer. This profile development is shown in the measurements, as Figure 5.2 shows.

The calculated velocity profiles shown in Figure 5.2 were obtained using the "law of the wall" approach for the boundary layers, as was described in Appendix A2. To ascertain exactly how well this computational convenience really works, it is necessary to examine the boundary layer parameters. The boundary layer thicknesses, defined as the distance normal to the wall to where the local velocity reaches 99 percent of the "free-stream" value, are compared in Figure 5.3. These thicknesses reflect the profile development across the duct in a quantitative manner. The agreements of the calculations with the measurements are good. Figure 5.4 compares momentum thicknesses, $\hat{\alpha}$, for the suction side. Again, the agreement is good.

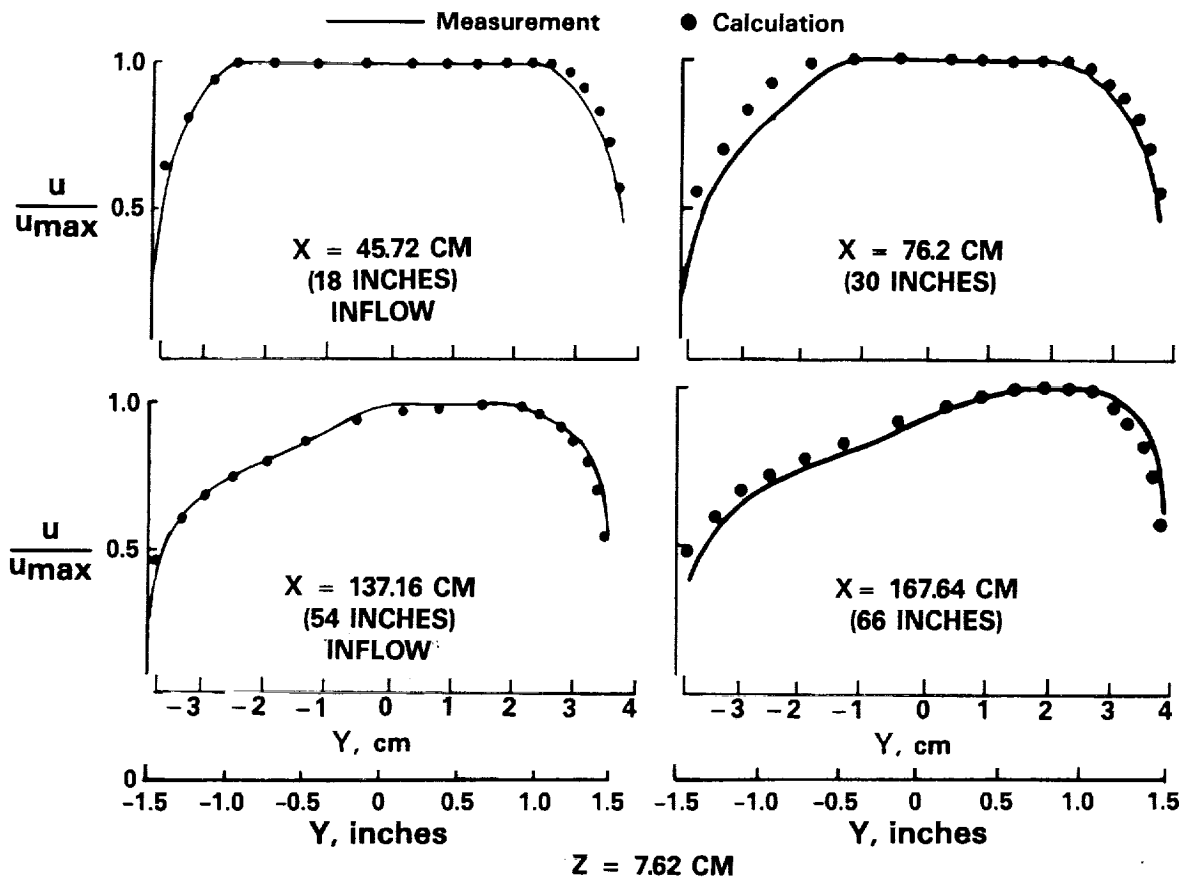


Figure 5.2 Calculated and Measured Mean Axial Velocity Profiles in Moon's Experiment

Figure 5.5 compares measured and calculated skin friction coefficients along the duct. The measurements are based on a Preston tube, and the calculations were obtained on the basis of a Clauser plot. It can be seen that on the suction side of the duct there is excellent agreement between measurement and calculation, except for the last station where the measured skin friction is higher than calculated. The last measurement station is close to the duct outlet, and flow at this station was probably influenced by the outlet (Ref. 17). On the pressure side, the initial agreements are good, but the measured skin friction increases with distance much more rapidly than calculated. This is most likely due to the turbulence changes due to rotation, which are not accounted for in the calculation. The turbulence changes and the secondary flows may also causes changes in the velocity profile through the boundary layer. This is assumed to be "universal" in the calculations.

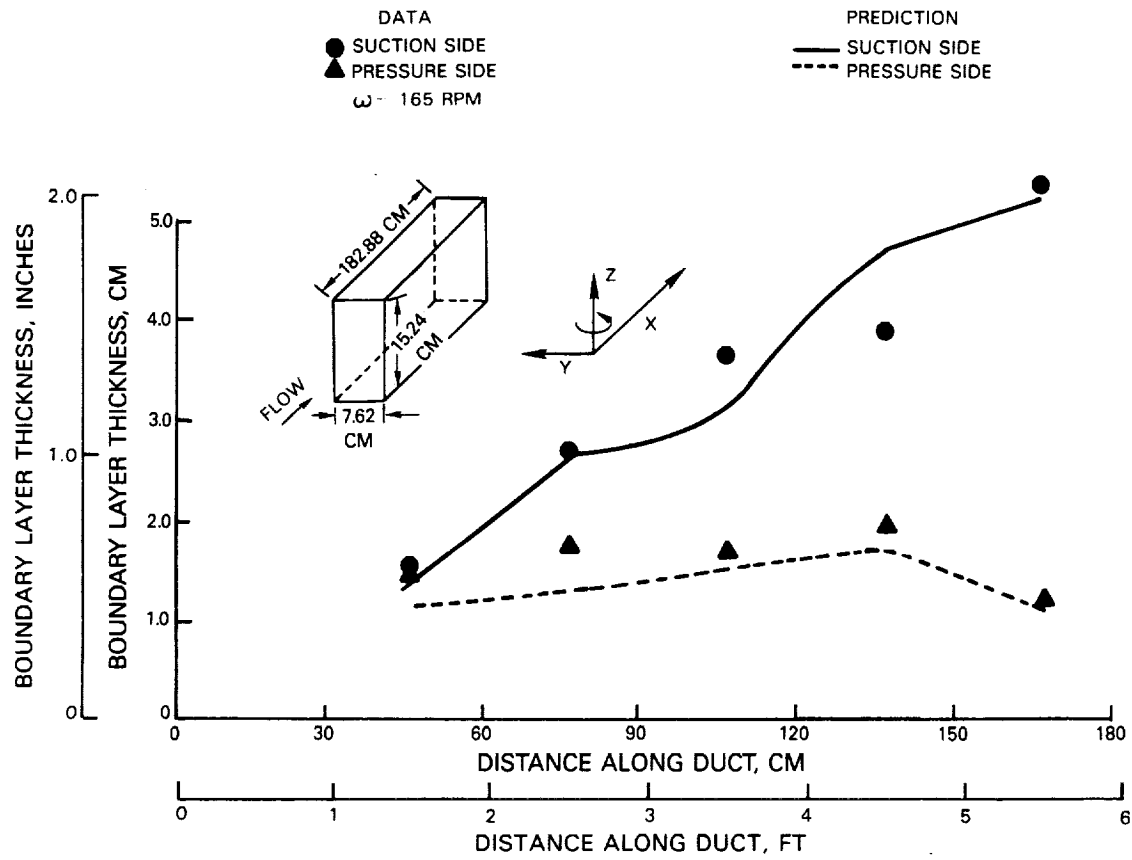


Figure 5.3 Comparisons of Boundary Layer Thicknesses Along Pressure and Suction Walls of Moon's Duct

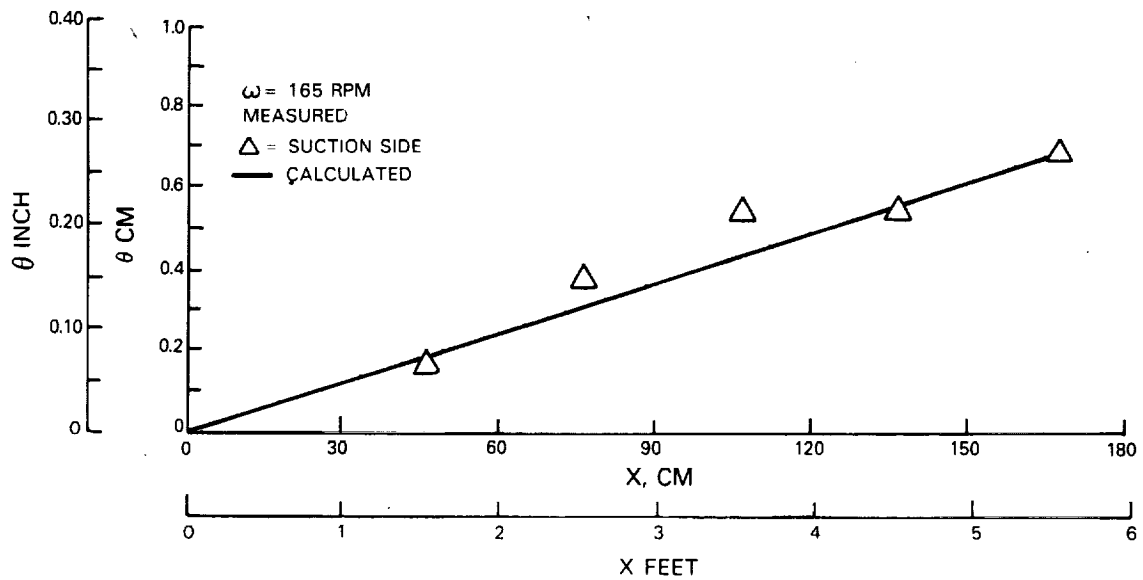


Figure 5.4 Comparison of Momentum Thickness on Suction Wall of Moon's Duct

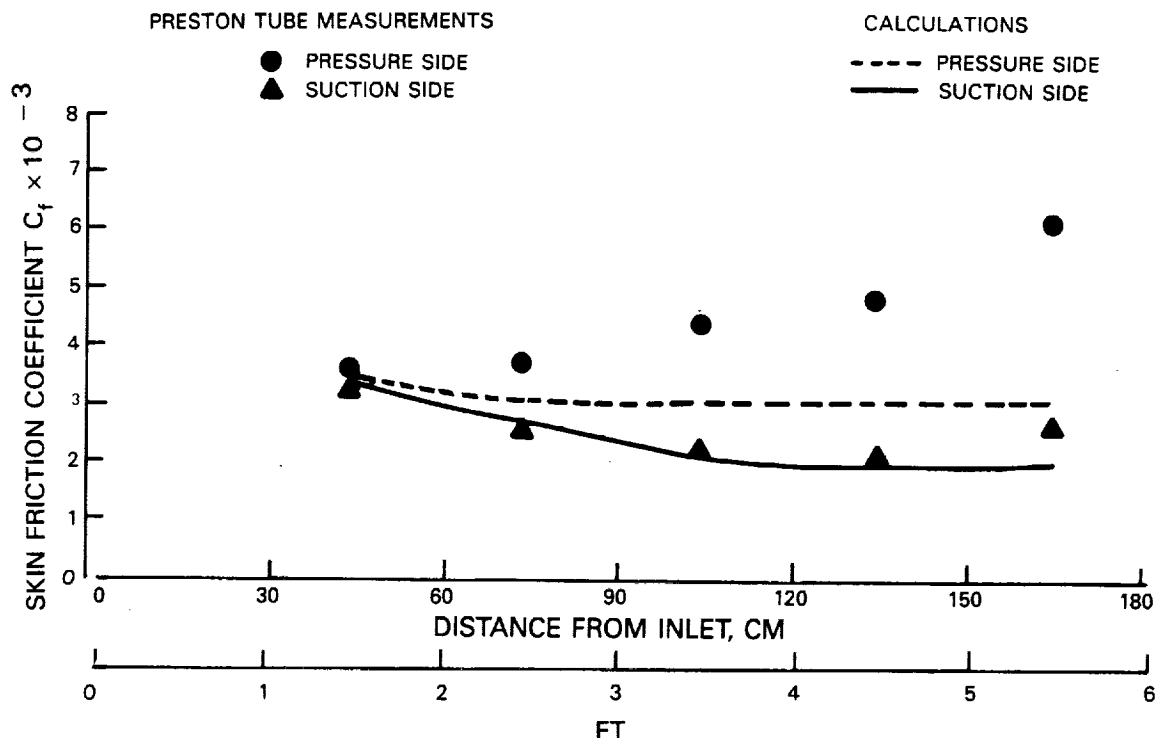


Figure 5.5 Skin Friction Coefficient Variation Along Pressure and Suction Walls in Moon's Duct

5.1.4 Fluctuating Quantities

The turbulence model used in the calculations is known to have both limitations and shortcomings for the present application. Therefore, good agreements between measurements and calculations for turbulence quantities should not be expected. For this reason, extensive comparisons of these quantities were not attempted.

Inherent in the turbulence model is the assumption of turbulence isotropy, i.e., if a prime represents a fluctuating velocity component, $u' = v' = w'$. The code calculates the specific kinetic energy of turbulence K (Equation 3.3) which, with isotropy, is:

$$K = 3/2 (u'^2) \quad (5.1)$$

where the overbar denotes a time-mean velocity. Now, the experiment presents measurements of u' and v' . If an assumption is made for w' , the "measured" and calculated specific kinetic energies of turbulence may be compared. There are two plausible assumptions for w' :

$$1. \quad w' = v', \text{ so that } K = 1/2(u'^2 + 2 v'^2) \quad (5.2)$$

$$2. \quad w' = 1.5v', \text{ so that } K = 1/2(u'^2 + 2.5 v'^2) \quad (5.3)$$

The latter assumption is based on the flat plate boundary layer measurements of Klebanoff (Ref. 22).

Figure 5.6 compares the calculated profile of K across the duct at the 66 inch (1.68 m) station with "measured" profiles based on the measured profiles of u' and v' together with the two assumptions above for w' . Outside of the boundary layers the three curves are in good agreement. The agreements with either of the w' assumptions are quite poor in the thicker boundary layer existing on the suction wall. The agreements were better for the thinner, pressure-wall, boundary layer, especially for the second of the assumptions about w' .

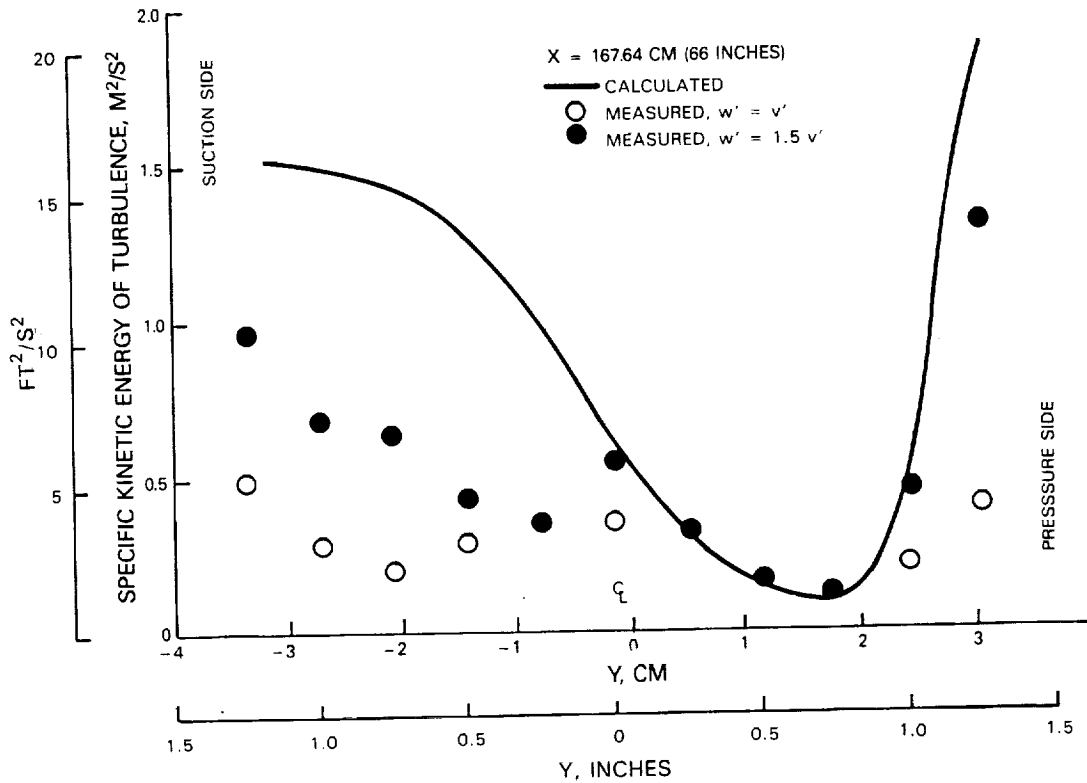


Figure 5.6 Kinetic Energy of Turbulence Profiles Across Moon's Duct Close to Exit

The Reynolds stress $u'v'$ can be found (Equation 3.2) from:

$$-\overline{u'v'} = \frac{\mu_t}{\rho} \left(\frac{\partial \bar{u}}{\partial y} + \frac{\partial \bar{v}}{\partial x} \right) \quad (5.4)$$

The calculated mean velocity information and the turbulence model (Equation 3.4) provide the gradient information and eddy viscosity to enable the Reynolds stresses to be found. These are compared with the hot-wire measurements of the Reynolds stress $u'v'$ in Figure 5.7 at two stations down the duct.

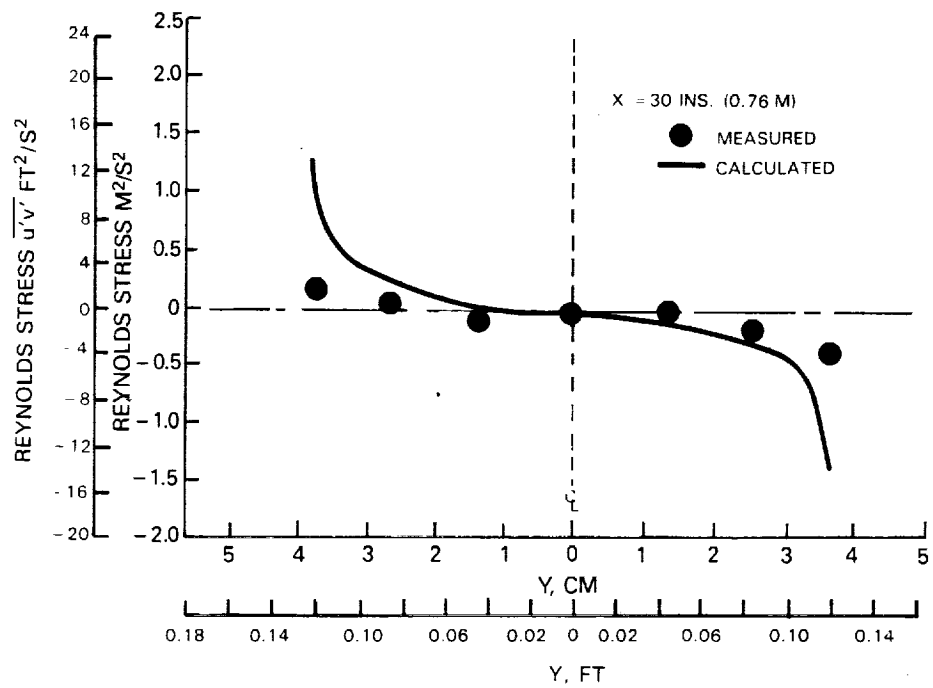
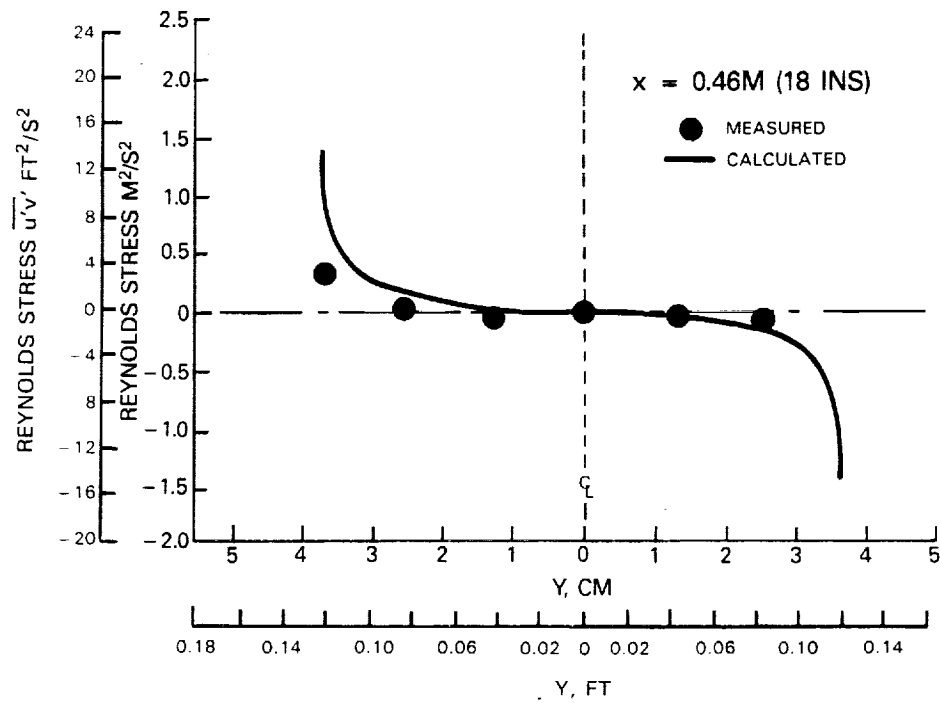


Figure 5.7 Reynolds Stress Comparison Across Moon's Duct on Inflow Leg

On the pressure side of the duct $-\bar{u}'\bar{v}'$ is negative, and on the suction side it is positive, and this is reproduced in the calculations. However, the magnitudes of the Reynolds stresses are over-estimated on both sides of the duct by the turbulence model. The discrepancy between the measurements and calculations increases with increasing distance down the duct. It should be noted that the accuracy of the gradients used in Equation 5.4 is severely and adversely affected by the limited grid used in the calculations.

5.1.5 Summary

The experiment is a nice one because it confines itself to a simple geometry and isothermal flow, and has mean and fluctuating velocity information. Boundary layer parameter information is also included. It lacks flow visualization and cross-stream velocity component measurements, and the instrumentation is intrusive. Measurement accuracy information is not available.

The calculations reproduce the measured flow behavior in every respect in qualitative fashion. The accuracy is affected by the relatively coarse grid that had to be used. The quantitative accuracy of the mean flow calculation is, however, fairly good. The boundary layer parameters do not calculate particularly accurately. Considering the grid used, the use of wall functions to describe the boundary layers, and the known limitations of the existing turbulence model, this should not be surprising. The fluctuating quantities are not accurately calculated. This is common experience with the two-equation turbulence model (Ref. 3) when used for complex flows.

5.2 Effects of Duct Aspect Ratio with Rotation

5.2.1 Computational Set-Up

The available storage capacity on the computer was again restricted to 4 Megabytes. However, since the previous calculations had required large amounts of computer time to achieve convergence, some economies were introduced to reduce this. This of course, represents a conscious trade-off of resolution and accuracy for economy. The grid used was $12 \times 18 \times 12$. The y-grid lines were not uniformly distributed, but expansion and contraction factors were applied to the grid to concentrate cells on the suction and pressure side walls where the boundary layers of interest are.

5.2.2 Flow Visualization

Figure 5.8 uses streaklines to show vortex development in the cross-sections of two ducts with aspect ratios $1/2:1$ and $7\ 1/3:1$, rotating at a steady speed of 175 RPM. The cross-sections are 1.37 m (4.5 ft.) from the inlet.

The general features of the flow are similar to those shown in Figure 5.1, and have the counter-rotating vortex pair formation due to Coriolis forces (Figure 5.8). The effects of the passage aspect ratio, which interchanges major and minor axes, are obvious.

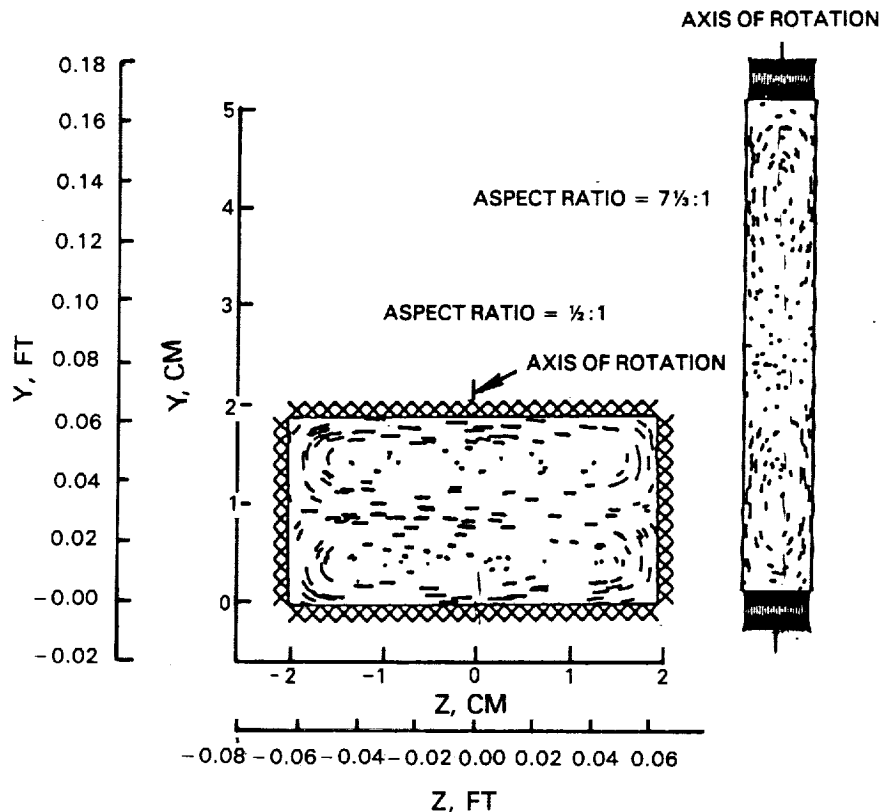


Figure 5.8 Streaklines Showing Vortex Development for Different Aspect Ratio Ducts in Moore's Experiment

5.2.3 Velocity Profile Development

To examine the effect of passage aspect ratio centerline profiles of mean axial velocity are compared at a station of 1.37 m (4.5 ft.) from the entrance to the duct. This is on the outflow leg of the duct. This is done for aspect ratios of 1:1, 4:1 and 7 1/3:1; the rotational speed was again 175 RPM.

Figure 5.9 compares the calculated profiles. For reference, the aspect ratio was 2:1 for the experiment described under Section 5.1. To obtain the aspect ratio variation, the duct width D was kept constant and the height L was varied. As the aspect ratio, L/D , increases past 1:1, the profile shift to the pressure wall due to rotation that was described in Section 5.13, becomes reduced. The flow visualization of Figure 5.8 suggests this is because the vortex centers become further apart, and the flow on the horizontal centerline is not well-organized, remaining relatively undisturbed.

The calculations show the effect of aspect ratio with qualitative accuracy. The quantitative agreement is reasonable for the 4:1 aspect ratio. It is not as good for the 1:1 aspect ratio. The accuracy for both aspect ratios is inferior to that for the 2:1 aspect ratio passage calculated earlier. The disagreements are particularly severe on the suction wall where the boundary layer thickening takes place. However, careful consideration of Figure 5.10 yields two relevant observations:

CENTERLINE VELOCITY PROFILES
PREDICTIONS FOR J. MOORE EXPERIMENT FOR ROTATING DUCT
FOR ASPECT RATIOS OF 1:1, 4:1, 7 1/3:1
FOR A ROTATION NUMBER OF 0.0207 (175 RPM)

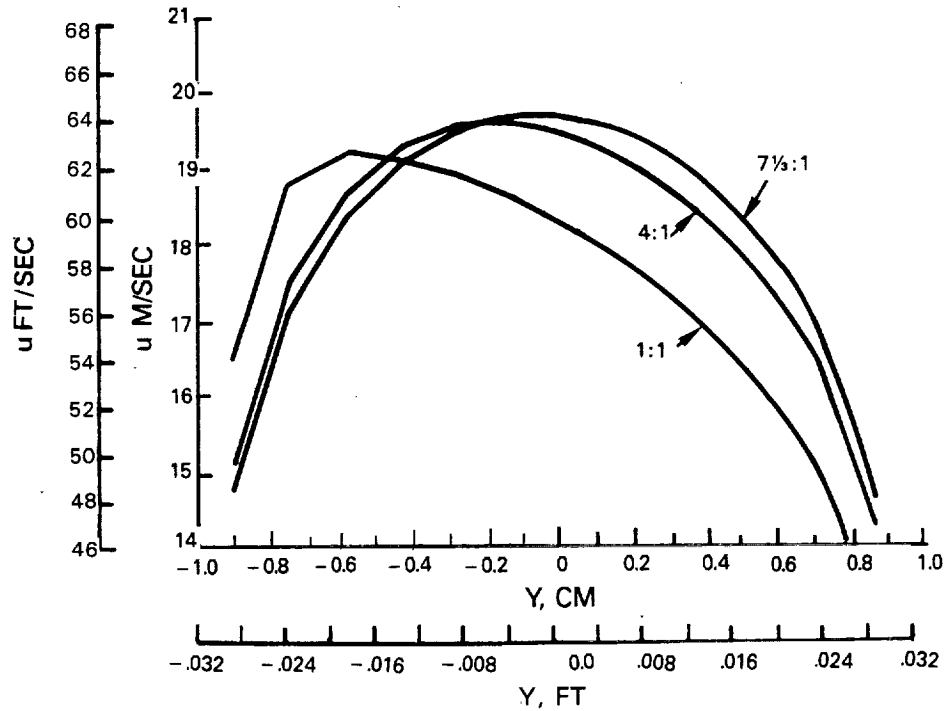


Figure 5.9 Calculated Effects of Duct Aspect Repeat Ratio on Mean Axial Velocity Profiles in Moore's Experiment

Figure 5.10 compares the measured velocity profiles with those calculated for aspect ratios of 1:1 and 4:1. This comparison provides for a quantitative assessment of the code.

1. The normalizing factor u_{max} was poorly defined in the experiment, and quite clearly the value used in Figure 5.10 is not the correct one for any of the profiles shown.
2. The gradients of velocity are fairly well calculated.

Therefore, there is absolutely no reason to suppose that the quantitative accuracy is any worse, or better, than that demonstrated in Figure 5.2 for the 2:1 aspect ratio passage. The effects of the grid changes, or the adequacy of either grid, cannot be assessed.

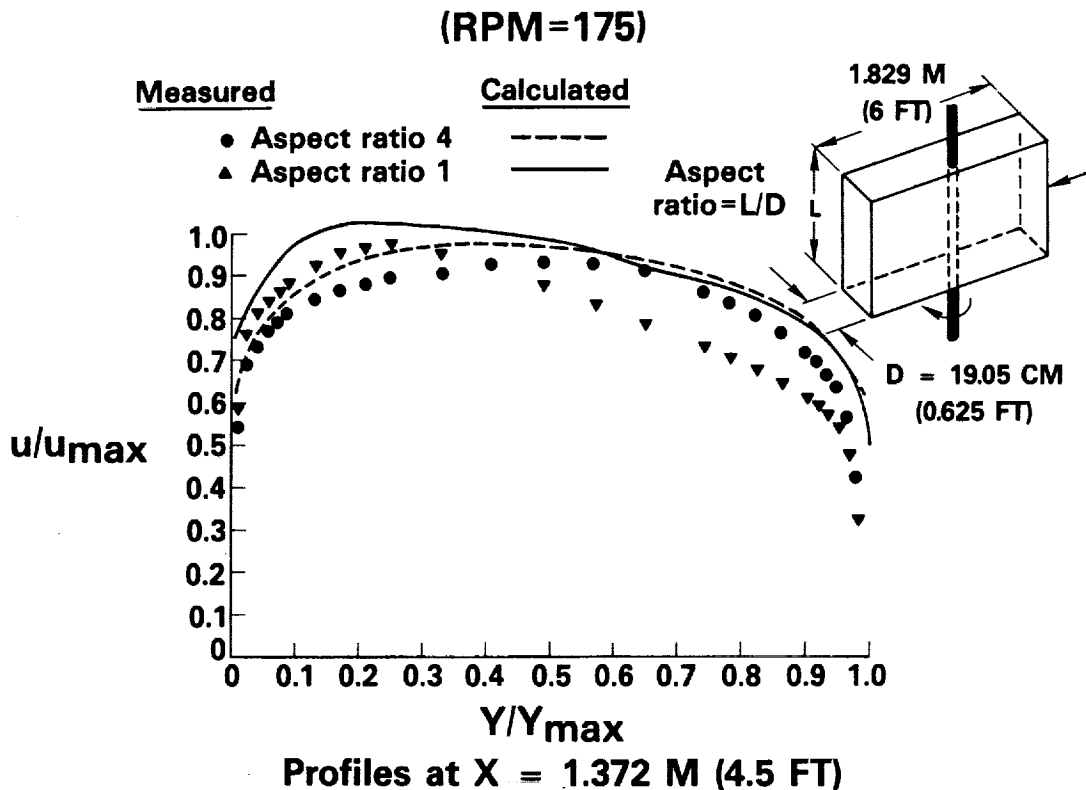


Figure 5.10 Comparison of Calculated and Measured Aspect Ratio Effects on Mean Axial Velocity Profiles

5.2.4 Effects of Rotation

For a fixed aspect ratio of 1/2:1 centerline profiles of mean axial velocity were calculated for a number of rotational speeds covering rotation numbers $\Omega D/\bar{u}$, from 0 to 0.082. The results are shown in Figure 5.11 (See Figure 5.8 for the general flow pattern at this aspect ratio).

As might be expected, the profile shift toward the pressure side increases with increasing rotation. This is in qualitative agreement with the findings in Reference 18; direct comparisons against the data were not made because of the uncertainty concerning the definition of the normalizing factor u_{max} in the reference.

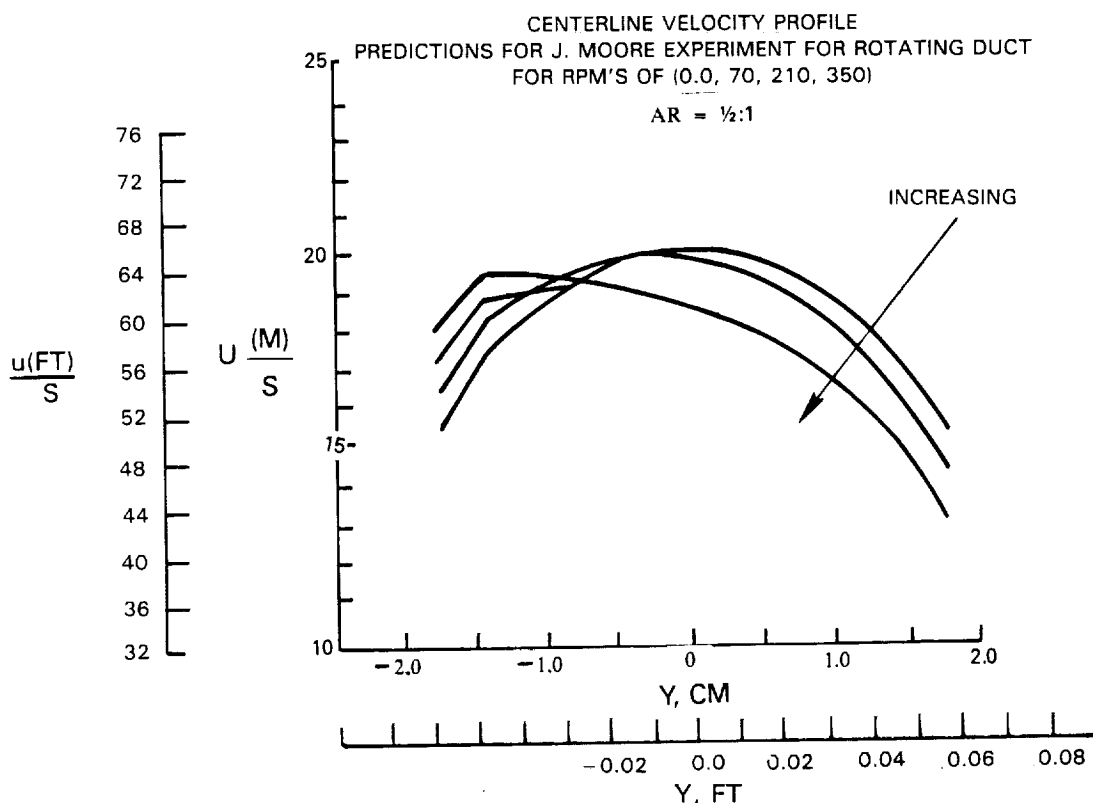


Figure 5.11 Calculated Effect of Rotation Number on Mean Axial Velocity Profiles in Moore's Experiment

5.2.5 Summary

It is unfortunate that the full potential of the experiment could not be used due to inadequate definitions in the data presentation. However, the calculation, once again, reproduced in qualitative fashion the measured behavior in every respect for the limited parameters compared. If more comprehensive comparisons could have been made there is no reason to expect results any different than found under Section 5.1. The accuracy would still be dominated by the coarseness of the grid upon which the calculations were performed. The limitations imposed through the use of wall functions and the two-equation (isotropic) turbulence model would remain.

The combined results show that passage aspect ratio introduces another important effect that influences the flow, in addition to rotation and the presence of a sharp bend. It might be anticipated that combinations of parameters could be such that ranges of variables would exist where one or another of the effects dominated the overall flow field.

5.3 Surface Heat Transfer in a Sharp Bend

5.3.1 Computational Set-Up

The flow path shown in Figures 4.3 and 4.4 was provided in the experiment with a plenum chamber at entrance and an exit section. To provide better definition of the inlet conditions to the section, and to give the correct back-pressure, both the inlet and outlet sections were calculated. A $12 \times 6 \times 8$ grid was used for each of these. For the heated test section, a $24 \times 14 \times 8$ grid was used, arranged to increase the number of grid lines adjacent to the surfaces of interest. This grid-densing did not, of course, approach that necessary to truly calculate the boundary layers.

5.3.2 Comparison Conditions

From the collected test data, an inlet width W_1 (see Figure 4.3) of 3.175 cm (1.25 in.) was selected to give a ratio W_1/W_2 of unity. The duct height D was 1.27 cm (0.5 in.) and the turn dimension, H , was 2.54 cm (1 in.). Two Reynolds numbers, 10,000 and 60,000, were chosen.

5.3.3 Flow Visualization

Figure 5.12 shows a flow visualization made in a similar geometry to that under consideration (Ref. 23). It serves to reveal the basic features of the flow in such a duct. The flow shown is the surface flow made visible using the technique of Langston at the University of Connecticut.

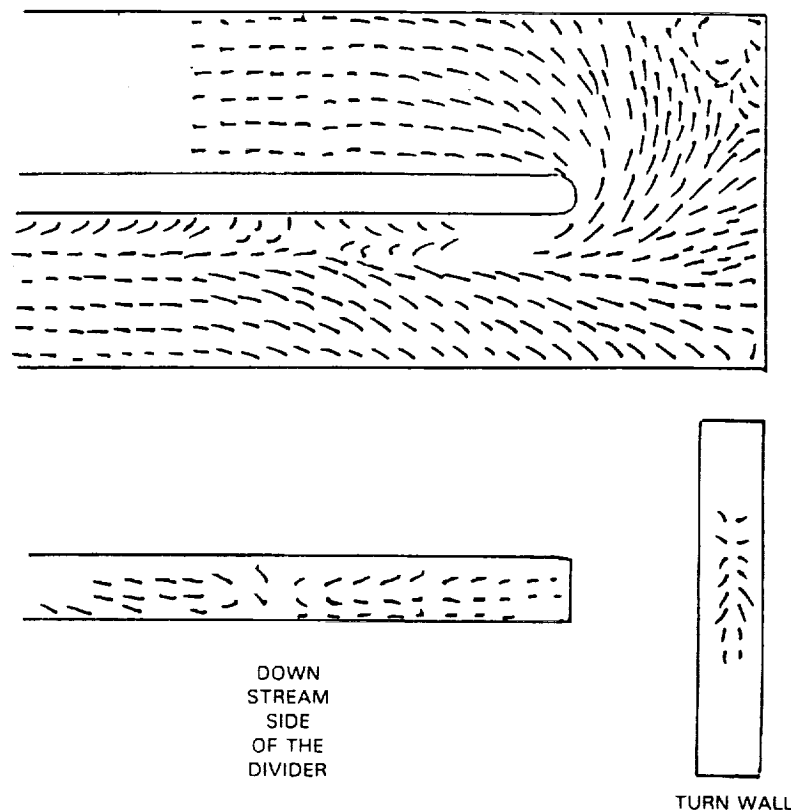


Figure 5.12 Experimental Visualization of Flow Development on Bottom Surface of a Sharp Turn, Showing Separated Flow Regions

The calculated surface flow ($z = 0.001$ ft or 0.03 cm from the surface) is shown in Figure 5.13. The corner-vortex on the first bend is reproduced in the calculations, as is the separated flow region on the dividing partition immediately downstream of the second bend. The presence of a thick boundary layer on the partition downstream of the separated flow reattachment appears to be evident.

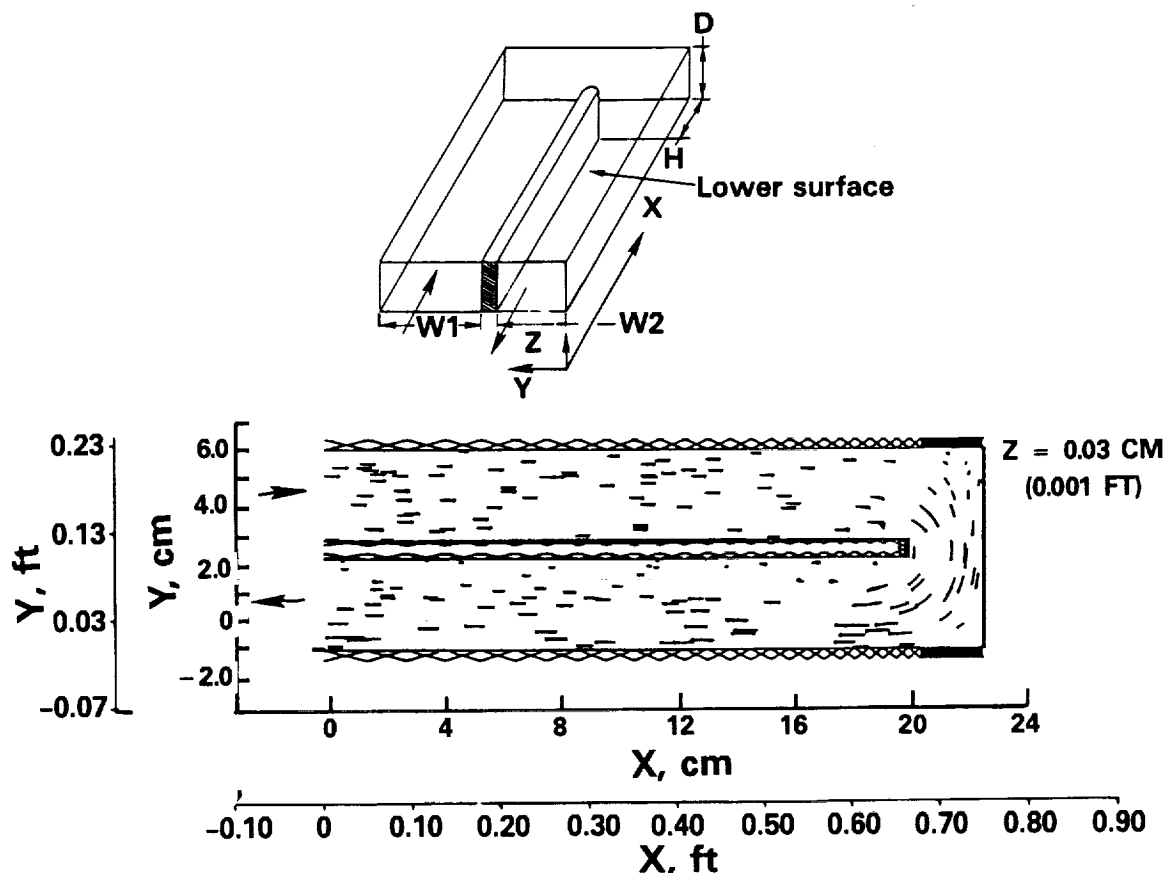


Figure 5.13 Calculated Streakline Flow Visualization on Bottom Surface of Metzger's Experiment Showing Separated Flow Regions

5.3.4 Surface Heat Transfer

The Nusselt numbers calculated for the lower surface of the duct are compared with values derived from measurement in Figure 5.14 for the two Reynolds numbers, which are based on hydraulic diameter. The Nusselt numbers are overall values for each of the regions shown in Figure 4.4. The calculated heat transfer coefficients were based on a "film temperature" which was taken as the value at the first grid-node away from the wall, a specified wall temperature, and the calculated heat flux.

The results of the comparison are encouraging. The level-change in Nusselt number with Reynolds number is reproduced, as is the large increase caused by the 180° sharp bend -- a doubling of Nusselt number. On the outflow leg of the passage, calculated Nusselt numbers are less than measured, indicating a faster recovery of the flow from the effects of the bend. This may be due to

an incorrect calculation of the separated flow region on the downstream side of the partition. The numerical diffusion introduced due to the coarse grid could be responsible for this. A further cause could be the failure of the turbulence model to account for the changes in turbulence structure associated with the sharp bend. There is some question also as to how representative the temperature gradient to the wall is, and used in calculating the heat flux, with such a coarse grid.

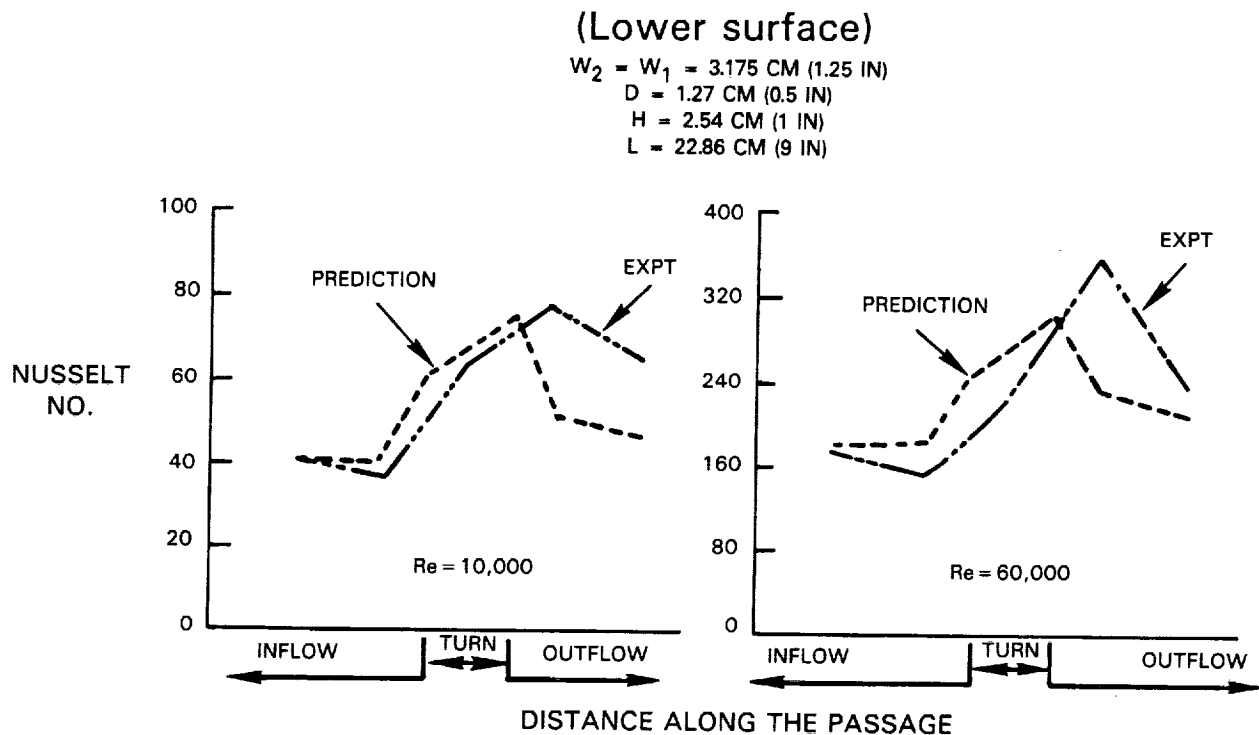


Figure 5.14 Comparison of Measured and Calculated Nusselt Number at Two Reynolds Numbers in Metzger's Sharp Turn Experiment

5.3.5 Summary

The surface heat transfer should be the most sensitive parameter to the shortcomings known to exist in the current code; specifically, the lack of resolution and the numerical diffusion associated with the forced use of coarse grids, and the isotropic turbulence model. There is reason to believe these shortcomings did adversely influence the calculations. However, the results are still extremely encouraging and do reproduce the general features, the changes with Reynolds number, and the correct levels of heat transfer.

6.0 DISCUSSION OF RESULTS

6.1 General Observations

A program of verification testing such as that described above in Sections 3.5 and 5.0 is a necessary step in the application of any CFD computer code to a new area; in this case, to heat transfer with rotation, which is far removed from the original application of the Pratt & Whitney-TEACH code to chemically-reacting combustor flows.

It was first necessary to check the soundness of the modifications introduced into the momentum equations to account for Coriolis and centrifugal forces, and that they were correctly programmed into the code. It was also desirable to obtain a "feel" for the influence of the known limitations of the code on the solutions obtained. This was necessary to ascertain what might have to be changed later in order to improve the quantitative accuracy. Furthermore, it was important to build up user experience of using the code for three-dimensional heat transfer calculations and rotating flows which were areas new to the TEACH group at Pratt & Whitney. This experience was required to build confidence in the modified code and its three-dimensional post-processor, to acquire problem set-up experience, and so establish an accuracy-base against which to compare the subsequent calculations of the experiments to be performed at United Technologies Research Center under this contract. The verification study accomplished these goals.

The known shortcomings existing in the modified code were concerned with numerical diffusion and flow resolution associated with the sparse grids, the stair-step representation of curvilinear geometries which is a consequence of the finite difference approach, use of an isotropic turbulence model not able to account for the changes in turbulence structure due to rotation and curvature, and the computationally-convenient use of "universal" wall-functions to represent boundary layers. Of these, only the second was not present in the verification testing carried out. The one believed to be most limiting in achieving quantitative accuracy was the first-numerical diffusion. This was, in the main, due to the unsuitability of the existing computer configuration for CFD work. Being concerned with surface heat transfer, it was also reasonable to expect that the turbulence model and use of wall functions might also exert a secondary effect on accuracy through their influence on the boundary layers.

The verification testing carried out was limited to simple configurations; specifically, straight passages with rotation, sharp turns without rotation, and smooth walls in all cases. The benchmark experiments themselves were considered to be adequate by the standards established for such a purpose (Section 4.1). They enabled the major features felt to be important in the blade cooling passage configuration to be explored. These were rotation, passage aspect ratio, and sharp turns. A more extensive program of verification testing against a broader base of benchmark experiments would have been desirable, but this desire was constrained by considerations of time and expense.

The general results of the verification study were exceedingly encouraging given the state-of-the-art in turbulent, recirculating flow CFD. The changes made to the equations of motion appear to be satisfactory and they seem to be correctly programmed. Qualitative agreements of flow patterns and data trends were obtained in all cases. Quantitative agreement was better than anticipated. The defects encountered appear to be those that were expected.

6.2 Fluid Dynamics

The fluid dynamic aspects of interest cover the general flow field, velocity profile development including boundary layer parameters, and the turbulence structure.

The results of the flow visualization are satisfactory. The flow characteristics are well shown in all cases, and the pictures presented are a great help in understanding the developing features. The flow visualization also helps explain the form of some of the measurements. For example, the sharp increase in heat transfer shown in the curves of Figure 5.14 can be related to the flow separation off the edge of the partition forming the sharp turn, as revealed in Figure 5.13. Similarly, the negligible shift in centerline axial velocity profile with rotation for the 7 1/3:1 aspect ratio passage visible in Figure 5.9 is explained by Figure 5.8 which shows a large, relatively axial flow region existing between the widely-separated vortex pair. The flow visualization suggests that combinations of passage geometry and operating conditions might exist under rotation where one flow feature or another might dominate the overall characteristics, or the characteristics in one section of a multi-pass passage (e.g., see Figure 3.8).

The development of axial-velocity profiles under the influence of rotation is calculated with acceptable accuracy, showing that at least the right equations of motion are being solved correctly. Indeed, there would be something seriously wrong with the modified code if centerline profiles of axial velocity could not be calculated.

The major discrepancies evident in Figure 5.10 are believed to be due entirely to the uncertainty with the values used for u_{\max} . Obviously, by definition all the curves must have a value somewhere of unity for u/u_{\max} . This being so, the effects of passage aspect ratio (on centerline profiles) may be considered also correctly calculated.

The code does go astray when it comes to calculating the boundary layer parameters with rotation. Although the boundary layer thickness δ is adequately calculated on both suction and pressure sides with rotation (Figure 5.3) and the momentum thickness $\hat{\alpha}$ on the suction side is reasonably well calculated (Figure 5.4) the skin friction is not so well calculated. Figure 5.5 shows good agreement on the suction side, but serious disagreement on the pressure side. The implication of this is that the universal profile used in the wall functions (see Appendix A2) is a good approximation on the suction side of the duct, but that the actual profile on the pressure side is different.

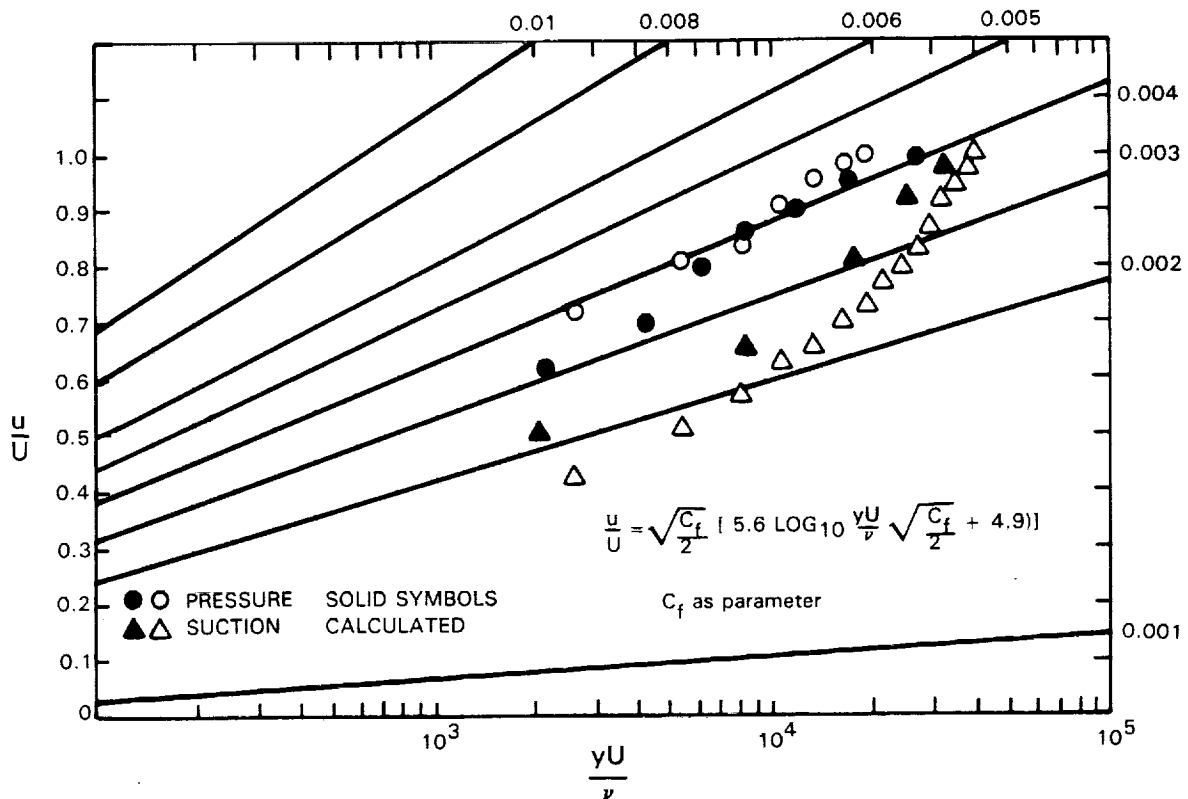
Moon (Ref. 17) reported that his measured boundary layer profiles were different on the two sides of the duct; the profile on the suction side was better represented by a power law. Moore (Ref. 18) showed that the measured departures from a log-profile on the suction side are functions of both rotation number D/ω , and passage aspect ratio, with the largest effects being for aspect ratios of unity and less.

The effects reported by Moon and by Moore are related to the suction side of the duct, while the discrepancies in skin friction revealed in Figure 5.5 are related to the pressure side of the duct. The measured skin friction was obtained from Preston tubes and was reported as being about 10 percent higher than that obtained from Clauser plots (Ref. 24). The 10 percent difference between the Clauser plot results and the Preston tube measurements is far less than the discrepancy between the calculated and measured skin friction on the pressure side. At the beginning of the duct, the measured and calculated skin frictions are in agreement, so it does appear that the calculation is failing to account for all the physics associated with the developing flow in the duct under the influence of rotation.

A comparison of measured and calculated centerline profiles for Moon's experiment is made in Figure 6.1 at 106.7 cm (42 in.) from the duct origin. The information is presented in Clauser plot form so that the relationship to skin friction may be readily appreciated. The universal relationship used is stated on the figure; for reference, the TEACH code uses a relationship that can be expressed as:

$$\frac{u}{U} = \sqrt{\frac{C_f}{2}} \cdot 2.3883 \ln 9.793 \frac{yU}{\nu} \sqrt{\frac{C_f}{2}} \quad (6.1)$$

from which the calculated skin friction values given in Figure 5.5 were obtained. Equation (6.1) yields slightly lower values of skin friction than the equation in Figure 6.1.



UNIVERSAL PLOT OF VELOCITY PROFILE AT STATION 4M = 165 RPM

Figure 6.1 Clauser Plot of Axial Velocity profiles for Moon's Experiment

Although the absolute value of skin friction from Figure 6.1 cannot be compared directly with those in Figure 5.5 since the calculations used a different universal profile, Equation (6.1), relative magnitudes may be compared.

It can be seen from Figure 6.1 that although calculated and measured profiles for both suction and pressure sides of the duct agree with each other in the outer "wake" component of the boundary layer, this is not so in the log-law region of the inner layer. On the pressure side, the calculated profile indicates a lower skin friction at this station than the measured profile, while on the suction side the calculated profile indicates a higher skin friction than measured. Both calculated and measured profiles indicate that skin friction is higher on the pressure side than on the suction side, and this is consistent with the Preston tube measurements shown in Figure 5.5. The differences between calculation and measurement should not be as large as that indicated for the pressure side in Figure 5.5. Comparison of the calculated suction side profile with the measured profile shows that the calculated profile is indicating the logarithmic form which gave rise to it, while the measured profile is not logarithmic for the smallest value of yU/ν of about 2,500.

The Clauser plot approach to skin friction implies that a universal profile has a fixed turbulence structure associated with it, i.e.,

$$C_{f/2} = \tau_w / \rho U^2 \quad (6.2)$$

and,

$$\tau_w = -\rho \overline{u'v'} \quad (6.3)$$

The skin friction calculations are therefore wrong in two respects: the wrong velocity profile is calculated because of the imposed logarithmic wall function, and the isotropic turbulence model does not calculate the changes in turbulence structure associated with rotation, specifically the increase in turbulence on the pressure side and its suppression on the suction side (see Figures 5.6 and 5.7).

6.3 Heat Transfer

The agreement of calculated Nusselt numbers with those derived from measurements at both Reynolds numbers investigated are satisfactory in the inflow passage and around the sharp turn. They go astray in the outflow passage where the calculation shows lower heat transfer than measured. However, the form of the heat transfer distributions and the increases with Reynolds number, are correctly calculated, Figure 5.14.

The implication of Figure 5.14 is that the calculations are showing a much faster recovery from the effects of the bend and a return to passage flow than is measured. This is almost certainly associated with calculation of the separated-flow region on the downstream side of the central partition forming the turn. This separated flow is shown in Figures 5.12 and 5.13. The major cause of the failure to calculate the separated region correctly is almost certainly a lack of resolution and the high numerical diffusion arising from the coarse grid used. In addition, the "law of the wall" used in the wall functions contained in the code is unlikely to hold in the vicinity of the reattachment point (see Appendix A2 for details).

6.4 Summary

Although results of the study indicate an encouraging start in calculating heat transfer in rotating passages involving sharp flow-turns, they also indicate areas where the calculation is deficient. The difficulties revealed were not unexpected (see Sections 3.2 and 3.3). Specifically, it is clear that the two-equation turbulence model is not adequate, and representation of the extra strains associated with flow rotation and turning is needed. The use of wall-functions might be acceptable if these were modified to account for rotation. Resolution and numerical diffusion with the allowable grids (computer and cost limitations) prevents accurate determination of the gradients near the walls. The lack of a curvilinear formulation for the equations was not a factor in the present study, but could create a problem in the experiment to be calculated (Figure 3.3). Ironically, the calculation is not so likely to be limited by this lack for real blade passages (Figures 2.1 and 3.5).

7.0 CONCLUSIONS AND RECOMMENDATIONS

7.1 Conclusions

As a result of analysis and data correlation in Phase I, Task III of the NASA sponsored program to investigate heat transfer within rotating turbine blades, the following conclusions may be drawn:

1. The 3D-TEACH code is a suitable selection as a baseline code.
2. The modifications to the momentum and enthalpy equations to account for rotation are appropriate.
3. The accuracy of the code for making three-dimensional calculations where the "mainstream" and "boundary layer" regions of the flow are both important, is severely compromised by the relatively coarse grids that have to be used with the current generation of computers.
4. The turbulence model currently incorporated in the code does not permit adequate calculation of the turbulence quantities where rotation and turning is involved.
5. The lack of a body-fitted coordinate system in three-dimensions causes difficulties in adequately representing smooth turns.
6. Where a stair-step representation of the passage walls is important, the existing wall-functions could be inappropriate.
7. The results of the study are encouraging enough both to believe that CFD can make a useful contribution to blade internal cooling, and to proceed further with the present program.

7.2 Recommendations

Following-on from the conclusion, it is possible to make some recommendations. It is not implied that these recommendations will be implemented during the course of the present contract.

1. Turbulence models more advanced than the present two-equation model can be formulated and should be explored for this application.
2. Modification of the wall functions to account for rotation can be made.

The computer problem and its resolution is beyond the scope of this report. Development of a three-dimensional curvilinear code is a difficult and costly task. It is certainly beyond the terms of the present contract.

APPENDIX A1

DESCRIPTION OF 3D-TEACH

1.0 Description of Aerothermal Model

3D-TEACH is a computer code that can solve fully three-dimensional fluid dynamics problems. It can handle axisymmetric, planar, or three-dimensional, elliptic, turbulent flows. It is one of a family of such codes with titles 2D-TEACH, 2D(C)-TEACH, 3D-TEACH and, 2D-PREACH.

The input to all of these codes is generalized such that different problems can be run without the need for Fortran programming between problems. Also, the physical models used can be turned on or off by input command. These collective features result in an extremely flexible system.

The codes form a family in that:

- a) As computer codes they are written with the same format, menus and commands such that an operator trained to run 2D-TEACH can easily run 3D-TEACH.
- b) All codes have an interactive nature using the IBM Conversational Monitor System (CMS), and use prompts and cautions to ensure smooth execution of a case. The operator has the choice of either CMS or Batch running. The recommended procedure is to set up a case and get it running on CMS, then switch it to Batch to complete execution. File modification and selection of running mode is identical for all codes.
- c) The same basic equations are solved and the same physical models are used, together with solution algorithms, in all codes such that regression is possible. This means that the same two-dimensional problem can be solved on 2D-TEACH and 3D-TEACH, and the same results will be achieved. The only difference between the 2D-TEACH and 3D-TEACH is the additional dimension available in the three-dimensional code. Also, the post-processors available with 3D-TEACH are necessarily more comprehensive than those with 2D-TEACH, in order to adequately display the results.

The acronym TEACH (Teaching Elliptic Axisymmetric Characteristics Heuristically) represents a generic solution technique and these codes represent current production state-of-the-art calculations in terms of equations solved, physical models used, discretization of the equations, and solution algorithms. They are not perfect, but are a marked advance on one-dimensional flow calculations and global modeling that formed the previous capability. The structure of the codes has been made such that modular replacement can be carried out as better models and solution algorithms are developed, while the basic framework and operational features remain.

The 2D-PREACH code is similar in concept to the others, but uses different solution procedures. It is not considered further here.

1.2 Outline of Calculation Procedure

1.2.1 Equations to Be Solved

The combustion process is an extremely complex turbulent flow. It is a somewhat daunting task to set about describing such a random flow of chemically active eddy structures in terms that can be currently solved and can provide useful answers for the designer of practical equipment.

Currently, the most practical approach is to stay within the framework of continuum mechanics and to use a statistical description of the turbulence, coupled with the accepted Eulerian description provided by the Navier-Stokes equations of motion. Hence, an instantaneous quantity is described as the sum of a time-averaged value and a random, fluctuating value.

When the statistical description of an instantaneous quantity is substituted into the Navier-Stokes equations (Ref. A1) and time averaged, the resulting equation set is known as the Reynolds equations (Ref. A2). These equations are similar to the Navier-Stokes equations except that time-averaged quantities are used, and for the appearance of time-averaged correlations of fluctuating quantities.

Turbulent motions increase the apparent viscosity of a fluid by some orders of magnitude since there is a continuous transfer of energy from the mean flow into large eddies and thence, cascading down through progressively smaller eddies, to the molecular level where the energy is dissipated as heat. If laminar diffusion terms are therefore very much smaller than turbulent diffusion terms, then neglect of fluctuations in laminar viscosity is permissible. This results in simplification of the Reynolds equations. It is a frequently used practice (Ref. A3) to also neglect terms involving fluctuating density, although this implies that temperature differences in the flow are not large. This practice also results in simplification of the Reynolds equations.

The simplified Reynolds equations are expressed in terms of time-mean quantities and also cross-correlations of fluctuating velocities such as $\rho u_i' u_j'$. These terms are known as the Reynolds stresses, and result in a closure problem. Turbulence modeling provides the necessary descriptions of the Reynolds stresses in known or determinable quantities. When the flow consists of more than one chemical species, modeling is required also for the turbulent mass flux $\rho u_i' m_j'$. These terms arise from applying the statistical treatment of turbulence to an instantaneous species transport equation. The instantaneous energy equation is given the same treatment.

To model the turbulent mass fluxes it was assumed that, similar to molecular Schmidt and Prandtl numbers, there are turbulent Schmidt and Prandtl numbers that relate turbulent mass and heat diffusivities to momentum diffusivity. Closure to the Reynolds equations was provided by a particular turbulence model known as the two-equation or K- ϵ model. It relies on the eddy viscosity concept. Finally, the modeled equations were algebraically manipulated into a general form in cylindrical co-ordinates:

$$\frac{\partial}{\partial x} (\bar{\rho} \bar{u} \bar{\phi}) + \frac{\partial}{r \partial r} (r \bar{\rho} \bar{v} \bar{\phi}) + \frac{\partial}{r \partial \theta} (\bar{\rho} \bar{w} \bar{\phi}) - \frac{\partial}{\partial x} \left(\Gamma_{\text{eff}, \phi} \frac{\partial \bar{\phi}}{\partial x} \right) - \frac{\partial}{r \partial r} \left(r \Gamma_{\text{eff}, \phi} \cdot \frac{\partial \bar{\phi}}{\partial r} \right) - \frac{\partial}{r \partial \theta} \left(\frac{1}{r} \Gamma_{\text{eff}, \phi} \frac{\partial \bar{\phi}}{\partial \theta} \right) = S_{\phi} \quad (\text{A1.1})$$

where:

- ϕ = any of the independent variables
- eff, ϕ = an appropriate turbulent exchange coefficient, depending on what ϕ represents
- S_{ϕ} = a so-called "source term" which lumps together all other terms in a given equation not included in the first four terms of Equation (A1.1).

The equation given is for steady state flow. Reynolds averaging does result in the equations retaining time-dependent terms, but these have been dropped. This was done for two reasons: (1) compatibility with the present design system and (2) time averaging precludes dynamic behavior other than that induced deliberately through one of the independent variables.

By way of example, Figure A1-1 gives the values of some of the items in Equation (A1.1).

1.2.2 Numerical Approach to Equation Solution

The simultaneous set of main and auxiliary equations to be solved in a turbulent reacting flow with a liquid-fuel spray contains a significant number of individual equations, most of which are either ordinary or partial differential equations, and which are nonlinear. Numerical solution of these equations is necessary. Rearrangement into the general form represented by Equations (A1.1) and (A1.2) enables one solution algorithm to be used for all equations.

Conventional numerical methods available to solve equations of these types can be broadly divided into finite difference and finite element methods, although the dividing line is not distinct. Finite differences have a considerable background, and most solution approaches utilize this method.

The finite difference analog of the differential equations is obtained by overlaying a computational mesh on the flow domain, and obtaining the basic finite difference form of the partial derivatives for every node of the mesh from a control volume approach (Ref. A4). The finite difference expressions, when substituted back into the differential equations, yield a set of linearized, algebraic equations for every node of the mesh. Thus, there are as many sets of equations as there are nodes in the calculation domain. These sets, along with the problem boundary conditions, can then be solved to give solutions for the entire flow field.

EQUATION	ϕ	$\Gamma_{eff, \phi}$	S_ϕ
CONTINUITY	1	0	0
x-MOMENTUM	\bar{u}	μ_{eff}	$\bar{\rho} g_x \cdot \frac{\partial \bar{P}}{\partial x} + \frac{\partial}{\partial x} \left(\mu_{eff} \frac{\partial \bar{u}}{\partial x} \right) + \frac{\partial}{\partial r} \left(\mu_{eff} r \frac{\partial \bar{v}}{\partial x} \right) - \frac{2}{3} \frac{\partial}{\partial x} (\mu_{eff} \nabla \cdot \vec{v}) + \frac{\partial}{\partial \theta} \left(\mu_{eff} \frac{\partial \bar{w}}{\partial x} \right)$
r-MOMENTUM	\bar{v}	μ_{eff}	$-\frac{\partial \bar{P}}{\partial r} + \bar{\rho} g_r + \frac{\partial}{\partial x} \left(\mu_{eff} \frac{\partial \bar{u}}{\partial r} \right) + \frac{\partial}{\partial r} \left(r \mu_{eff} \frac{\partial \bar{v}}{\partial r} \right) - \frac{\partial}{\partial r} \left(\frac{2}{3} \mu_{eff} \nabla \cdot \vec{v} \right) - \frac{\partial}{\partial \theta} \left(\mu_{eff} \frac{\partial \bar{w}}{\partial r} \right) + \frac{\bar{w}^2}{r} - \frac{2\mu_{eff} \bar{v}}{r^2} - \frac{2\mu_{eff}}{r^2} \frac{\partial \bar{w}}{\partial \theta} - \frac{1}{r} \frac{\partial}{\partial \theta} (\mu_{eff} \bar{w})$
θ -MOMENTUM	\bar{w}	μ_{eff}	$-\frac{\partial \bar{P}}{r \partial \theta} + \frac{\partial}{r \partial \theta} \left(\mu_{eff} \frac{\partial \bar{w}}{\partial \theta} \right) + \frac{\partial}{\partial x} \left(\mu_{eff} r \frac{\partial \bar{u}}{\partial \theta} \right) + \frac{\partial}{\partial r} \left(\mu_{eff} \frac{\partial \bar{v}}{r \partial \theta} \right) - \frac{2}{3} \frac{\partial}{r \partial \theta} (\mu_{eff} \nabla \cdot \vec{v}) + \frac{2\mu_{eff}}{r} \frac{\partial \bar{v}}{r \partial \theta} - \frac{\bar{v} \bar{w}}{r} - \frac{\bar{w}}{r^2} \frac{\partial}{\partial r} (\mu_{eff} r)$
TURBULENCE ENERGY	K	μ_{eff}/σ_K	$\mu_{eff} \left[2 \frac{\partial \bar{v}}{r \partial \theta} \frac{\partial \bar{w}}{\partial r} + 2 \frac{\partial \bar{w}}{\partial x} \frac{\partial \bar{u}}{r \partial \theta} + \left(\frac{\partial \bar{u}}{r \partial \theta} \right)^2 + \left(\frac{\partial \bar{v}}{r \partial \theta} \right)^2 + 2 \left(\frac{\partial \bar{w}}{r \partial \theta} \right)^2 \right] + \mu_{eff} \left[2 \left(\frac{\partial \bar{w}}{r \partial \theta} \cdot \frac{\bar{v}}{r} - \frac{\partial \bar{v}}{r \partial \theta} \frac{\bar{w}}{r} + 2 \frac{\bar{v}}{r} \frac{\partial \bar{w}}{r \partial \theta} \right) \right]$
ENERGY DISSIPATION	ϵ	$\mu_{eff}/\sigma_\epsilon$	$C_{\epsilon 1} \frac{\epsilon}{K} \mu_{eff} \left[2 \frac{\partial \bar{v}}{r \partial \theta} \frac{\partial \bar{w}}{\partial r} + \left(\frac{\partial \bar{u}}{r \partial \theta} \right)^2 + 2 \frac{\partial \bar{w}}{\partial x} \frac{\partial \bar{u}}{r \partial \theta} + \left(\frac{\partial \bar{v}}{r \partial \theta} \right)^2 \right] + C_{\epsilon 3} \frac{\epsilon}{K} \left[2 \mu_{eff} \left(\frac{\partial \bar{w}}{r \partial \theta} \right)^2 - \frac{2}{3} \nabla \cdot \vec{v} (\mu_{eff} \nabla \cdot \vec{v} + \bar{P} K) \right] + C_{\epsilon 1} \frac{\epsilon}{K} \mu_{eff} \left[2 \left(\frac{\partial \bar{w}}{r \partial \theta} \right) \frac{\bar{v}}{r} - \left(\frac{\partial \bar{v}}{r \partial \theta} \right) \frac{\bar{w}}{r} + 2 \left(\frac{\partial \bar{w}}{r \partial \theta} \right) \frac{\bar{v}}{r} + (\nabla \cdot \vec{v}) K - C_{\epsilon 2} \bar{P} \frac{\epsilon^2}{K} \right]$

where $\nabla \cdot \vec{v} = \frac{\partial \bar{u}}{\partial x} + \frac{1}{r} \frac{\partial (r \bar{v})}{\partial r} + \frac{\partial \bar{w}}{r \partial \theta}$

$C_{\epsilon 3}$ is an additional constant, presently taken as being equal to $C_{\epsilon 1}$.

Figure A1-1. Summary of Some of the Equations Solved in 3D-TEACH

ORIGINAL PAGE IS OF POOR QUALITY

Standard numerical techniques can be employed to solve the finite difference forms of the differential equations (Ref. A5). A steady-state implicit solution method is often used (Ref. A6); an initial guess is made of the field variables, and these guesses are iteratively updated until the solutions have converged. Convergence is deemed to have been obtained when the absolute sums of the residuals of each variable over the whole grid goes below a specified value.

The relevant equations describing the flow motions, the physical models, and the solution techniques are assembled into the computer codes to carry out direct flow simulations on high-speed, large-core digital computers. Figure A1-2 presents a flow diagram describing the calculation procedure, showing the assembly of the equations, the utilization of physical modeling, the computer solution, and the output for design use. The 3D-TEACH code conforms to this organization.

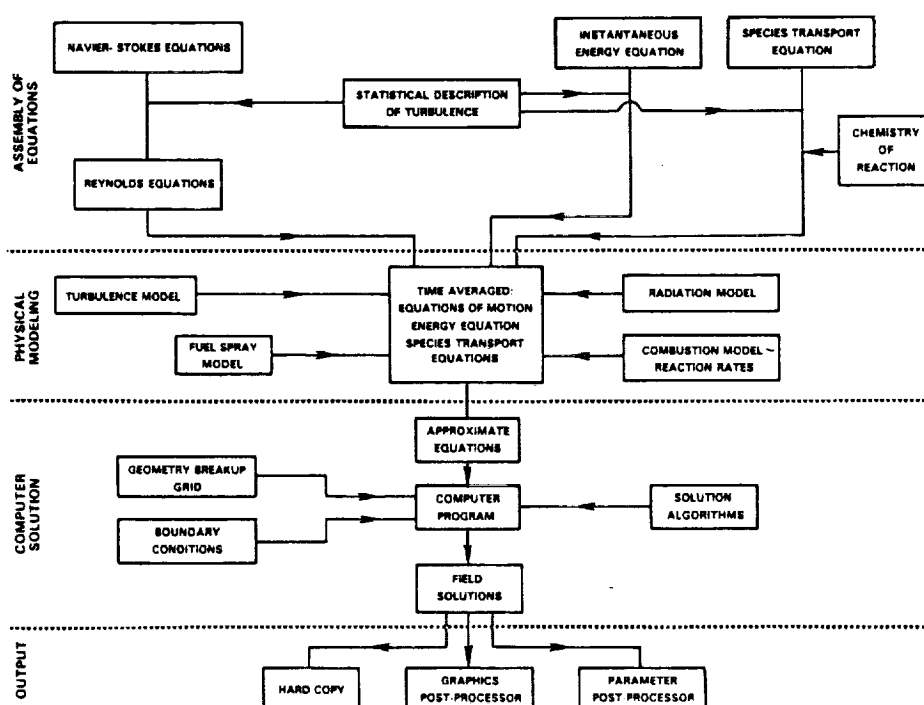


Figure A1-2 Flow Diagram of Calculation Procedure

1.3 Solution Procedure

With reference to Figure A1-2, assembly of the equations governing the problem has been briefly described. The details of the computer solution of the resulting equation sets are to be described.

Rearrangement of the equations into the general form represented by Equation (A1.1) enables one solution algorithm to be used for all equations. The equation set is solved using a steady state, implicit, finite difference

numerical procedure. Initial guesses are made of the field variables, and these guesses are iteratively updated until the solutions have converged. Convergence is deemed to have been obtained when the absolute sum of the residuals over the whole grid of each variable goes below a specified value.

1.3.1 Discretization of the Equations

The finite difference analog of the difference equations is obtained by overlaying a computational mesh on the flow domain to be calculated, and obtaining the basic finite difference form of the partial derivatives for every node of the mesh from a control volume approach, (Ref. A4). The finite difference expressions, when substituted back into the differential equations, yield a set of linearized, algebraic equations for every node of the mesh. To demonstrate, first in two-dimensions, Figure A1-3 illustrates the mesh and the control volume established about a considered node, P. The control volume approach is based on the satisfaction of macroscopic physical laws such as conservation of mass, momentum and energy. The conservation property is essential when combustion is taking place.

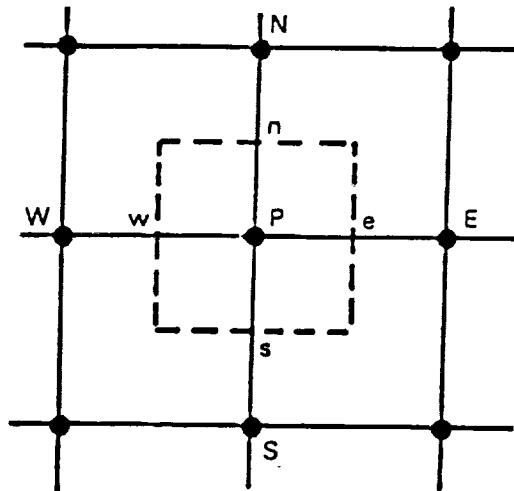


Figure A1-3 Control Volume for the Finite Difference Scheme

The code is written in both cylindrical and cartesian coordinates. The grid system consists of a set of coordinate lines intersecting in the $x-r$, $x-\theta$ and $r-\theta$ planes for the cylindrical system. In the cartesian system the grid is formed by the intersection of $x-y$, $x-z$, and $y-z$ plane lines. The intersections of these lines form the grid nodes at which all scalar properties are stored. Vector quantities are stored midway between nodes. Figure A1-4 gives the finite difference grid control volumes for the scalar quantities and storage locations for the velocities in both coordinate systems. Note that compared to Figure A1-3, there are two additional neighboring nodes, F and B, denoting Front and Back nodes in the z or θ direction. The faces of the scalar control volume are denoted by lower case letters. Figure A1-5 shows typical scalar

control volumes in perspective and gives the face areas and volume. Since the velocity components are located midway between the grid nodes, the control volumes for velocity components are formed by planes passing through the grid lines. Note that since the control volumes for the velocity components are staggered (Figure A1-6), the areas and volumes for these control volumes will be different from those of the scalar control volume.

The finite difference form of the general partial differential equation is derived by supposing that each variable is enclosed in its own control volume, as illustrated in Figures A1-3 to A1-6. The general ϕ transport equation has a source term S_ϕ . This is expressed in linearized form and integrated over the control volume. The remainder of the transport equation is also integrated over the control volume, and added to the integrated source term. This yields,

$$C_E \phi_e - C_W \phi_w + C_N \phi_n - C_S \phi_s + C_B \phi_b - C_F \phi_f = D_E (\phi_e - \phi_p) - D_W (\phi_p - \phi_w) + D_N (\phi_n - \phi_p) - D_S (\phi_p - \phi_s) + D_B (\phi_b - \phi_p) - D_F (\phi_p - \phi_f) + (S_u + S_p \phi_p) \quad (A1.2)$$

In the above equation the convection coefficients are defined as,

$$C_E = (\bar{\rho} \bar{u})_e a_e \quad ; \quad C_F = (\bar{\rho} \bar{w})_f a_f \quad \text{etc.},$$

and the diffusion coefficients are defined as:

$$D_E = \left(\frac{\Gamma_{eff, \phi}}{\Delta x} \right)_e \cdot a_e \quad ; \quad D_F = \left(\frac{\Gamma_{eff, \phi}}{r \Delta \theta} \right)_f \cdot a_f$$

etc. are the areas of the cell faces

Certain weighting factors are introduced into the variation of ϕ , the variable being calculated, and with the help of continuity, Equation (A1.2) can be manipulated and normalized to give the form,

$$A_p \phi_p = A_N \phi_N + A_S \phi_S + A_W \phi_W + A_E \phi_E + A_F \phi_F + A_B \phi_B + S_u \quad (A1.3)$$

where,

$$A_p = A_N + A_S + A_E + A_W + A_F + A_B - S_p$$

and Equation (A1.3) is the finite difference equation for ϕ , and the main coefficients are defined as,

$$A_N = 0 \text{ when } P_{e_N} < -2$$

$$A_N = D_N - \frac{C_N}{2} \text{ when } -2 \leq P_{e_N} \leq 2$$

$$A_N = C_N \text{ when } P_{e_N} > 2$$

Similarly for A_S , A_E etc., where the cell Peclet number is defined as,

$$P_{e_N} = C_N/D_N \quad \text{etc.}$$

There are several differencing schemes that can be used to evaluate the weighting factors. The values of the coefficients A_N , A_S , etc., above were obtained using Spalding's Hybrid Differencing Scheme (HDS), of Ref. A7.

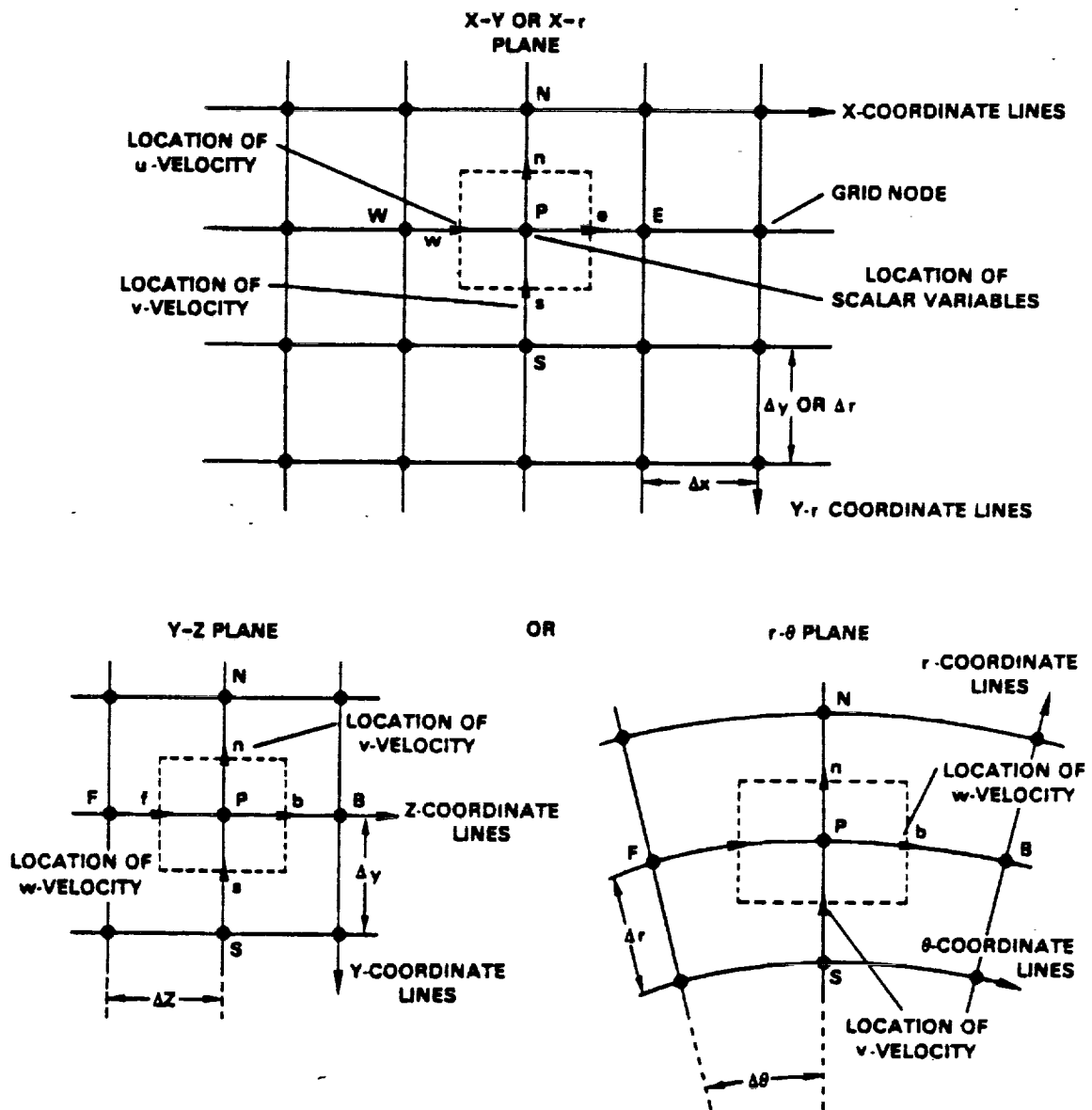
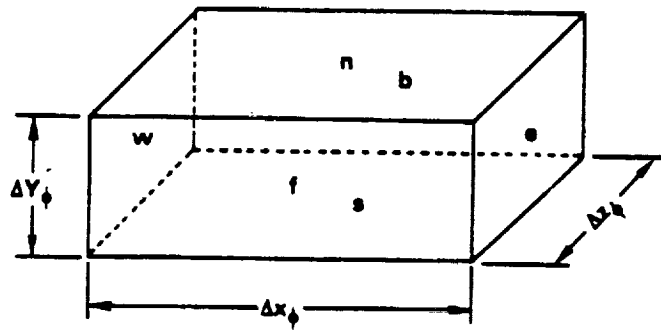
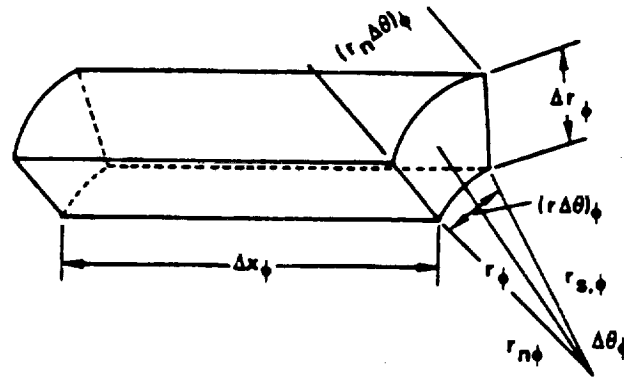


Figure A1-4 3-D TEACH: Finite Difference Grid in Cylindrical and Cartesian Coordinate Systems



CONTROL VOLUME IN THE CARTESIAN SYSTEM



CONTROL VOLUME IN THE CYLINDRICAL SYSTEM

AREA	CARTESIAN	CYLINDRICAL	REMARKS
a_w	$(\Delta Y \Delta Z)$	$(\Delta r \Delta \theta r)$	Cartesian system can be obtained from cylindrical system by putting $r = 1$. $\Delta \theta = \Delta Z$.
a_e	$(\Delta Y \Delta Z)$	$(\Delta r \Delta \theta r)$	
a_n	$(\Delta X \Delta Z)$	$(\Delta r \Delta \theta r_n)$	
a_s	$(\Delta X \Delta Z)$	$(\Delta x \Delta \theta r_s)$	
a_f	$(\Delta X \Delta Y)$	$(\Delta x \Delta r)$	
a_b	$(\Delta X \Delta Y)$	$(\Delta x \Delta r)$	
Vol	$(\Delta X \Delta Y \Delta Z)$	$(\Delta x \Delta r \Delta \theta r)$	

Figure A1-5 Perspective View of Scalar Control Volume, Giving Face Areas and Volume

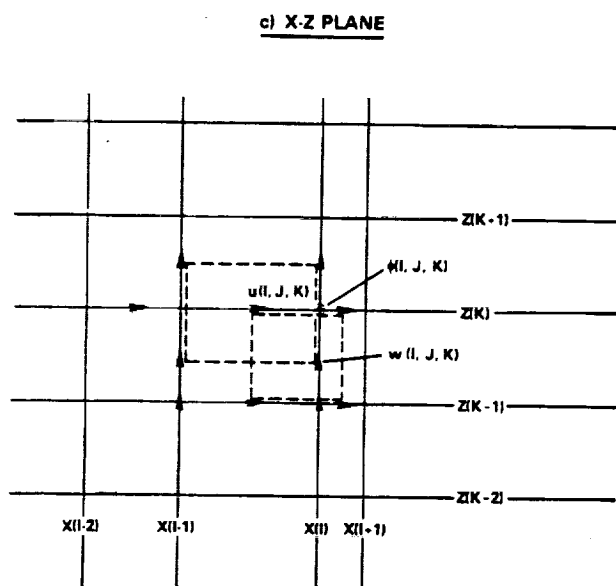
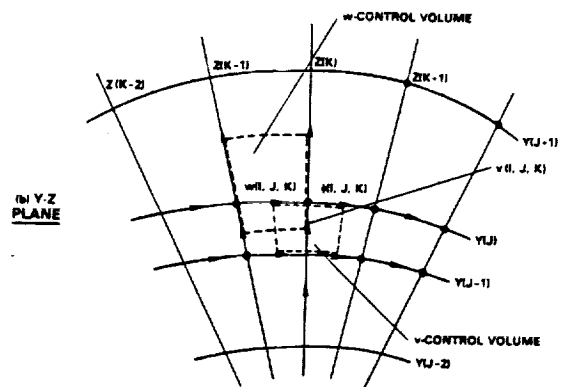
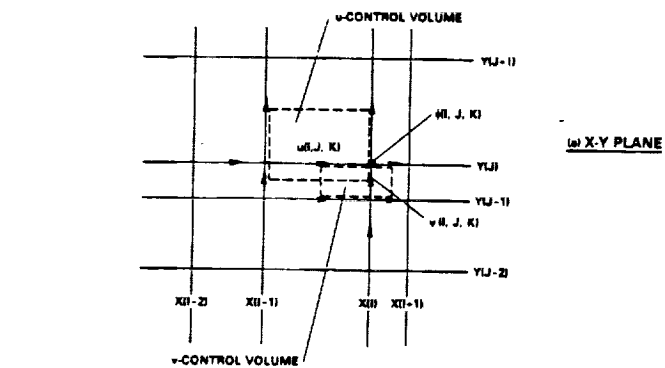


Figure A1-6 Control Volumes for Velocity Components

The hybrid differencing scheme is unconditionally stable and the solution is bounded. It uses second order central differencing for convection and diffusion fluxes when the absolute value of cell Peclet number is less than or equal to two. When Peclet number is greater than two, first order upwind differencing is used for convection fluxes, and diffusion fluxes are neglected altogether. The switch of differencing is done both locally and directionally in the computational grid. Peclet number defines the relative importance of convective and diffusive transport.

The finite difference Equation (A1.3) derived in the previous section could be used to obtain the velocity if the pressure field were known a priori. Since the pressure field is unknown, an iterative solution procedure, SIMPLE (Ref. A8) is used. SIMPLE is an acronym for Semi Implicit Method for Pressure Linked Equations.

The essence of SIMPLE is that a pressure field is guessed, velocities are calculated from their finite difference equations, then the pressure and velocity fields are updated using a "pressure correction" equation which satisfies continuity. The procedure is repeated until the momentum and the continuity equations are adequately and simultaneously satisfied. The pressure correction equation can be derived from the continuity and momentum equations; the procedure is described below.

The finite difference form of the continuity equation can be written as:

$$(\bar{\rho} \bar{u})_e a_e - (\bar{\rho} \bar{u})_w a_w + (\bar{\rho} \bar{v})_n a_n - (\bar{\rho} \bar{v})_s a_s + (\bar{\rho} w)_f a_f - (\bar{\rho} w)_b a_b = 0 \quad (A1.4)$$

The momentum equations can be written as:

$$A_p v_p^* = A_N v_N^* + A_S v_S^* + A_E v_E^* + A_W v_W^* + A_F v_F^* + A_B v_B^* + a_s (P_S^* - P_p^*)$$

$$A_p u_p^* = A_N u_N^* + A_S u_S^* + A_E u_E^* + A_W u_W^* + A_F u_F^* + A_B u_B^* + a_w (P_W^* - P_p^*)$$

$$A_p w_p^* = A_N w_N^* + A_S w_S^* + A_E w_E^* + A_W w_W^* + A_F w_F^* + A_B w_B^* + a_b (P_F^* - P_p^*)$$

In the above equations the pressure term has been separated from the source term and the (*) superscript denotes the values obtained from solving the momentum equations using the guessed pressure. An incorrect guess will give rise to a "mass source", M_p , in each cell because the continuity equation will not be satisfied. The mass source can be found by using Equation (A1.4). Hence

$$M_p = (\bar{\rho} u^*)_e a_e - (\bar{\rho} u^*)_w a_w + (\bar{\rho} v^*)_n a_n - (\bar{\rho} v^*)_s a_s - (\bar{\rho} w^*)_f a_f + (\bar{\rho} w^*)_b a_b$$

If the above equation is subtracted from Equation (A1.4)

$$-M_p = (\bar{\rho} u')_e a_e - (\bar{\rho} u')_w a_w + (\bar{\rho} v')_n a_n - (\bar{\rho} v')_s a_s - (\bar{\rho} w')_f a_f + (\bar{\rho} w')_b a_b \quad (A1.5)$$

where

$$u_e' = (\bar{u} - u^*)_e \text{ etc.}$$

The above velocity corrections can be calculated from the linearized momentum equations.

$$A_p u_p' = a_w (P_w' - P_p') \quad (A1.6)$$

Note that u_p' in the momentum equation control volume is u_w' for the continuity control volume and similarly for v_p' , etc.; On substitution of Equation (A1.6) in Equation (A1.5) and simplification,

$$A_p P_p' = A_N P_N' + A_S P_S' + A_W P_W' + A_E P_E' + A_F P_F' + A_B P_B' + S_u \quad (A1.7)$$

where

$$A_w = (a_w/A_p)$$

$$S_u = -M_p$$

$$A_p = A_N + A_S + A_W + A_E + A_F + A_B$$

Equation (A1.7) is called the pressure correction equation which is solved to obtain corrected velocities and pressures,

$$\bar{u}_e = u_e^* + u_e'$$

$$\bar{p}_e = p_e^* + p'$$

etc.

The difference equation for P' (Equation (A1.7)) is in the same form as the difference equations for ϕ (Equation (A1.3)) and hence a single solution algorithm can be used to solve all difference equations embodied in the numerical method.

Since the SIMPLE procedure computes the variable fields successively it is highly flexible with respect to the methods of solution which it will admit for the difference equations. At present the following line by line iteration method is employed. This method is also known as Alternating Direction Implicit Method (Ref. A9). The ADI methods were initially formulated for unsteady equations; their adaptation to steady state equations is sometimes also known as Alternating Direction Iterative Methods.

The finite difference Equation (A1.3) to be solved is

$$A_p \phi_p = A_N \phi_N + A_S \phi_S + A_W \phi_W + A_E \phi_E + A_F \phi_F + A_B \phi_B + S_u$$

where ϕ stands for u, v, p, K, ϵ , and H successively. This equation can be recast in the following form

$$A_p \phi_p = A_N \phi_N + A_S \phi_S + C'$$

or

$$A_p \phi_j = A_N \phi_{j+1} + A_S \phi_{j-1} + C_j' \quad (A1.8)$$

To solve the equations for points on each line (e.g., N-S line) values on neighboring lines are assumed to be temporarily known. The equation for each point on the N-S line then reduces to one where only three values (ϕ_p, ϕ_N, ϕ_S in Equation (A1.8)) are unknown. An equation of this type can then be solved by the Tri-Diagonal Matrix Algorithm (TDMA), which is explained below.

Equation (A1.8) can be rearranged for the j^{th} point as

$$\phi_j = B_j \phi_{j+1} + C_j \phi_{j-1} + D_j$$

where

$$B_j = A_N/A_p, \quad C_j = A_S/A_p$$

$$D_j = (A_W \phi_W + A_E \phi_E + A_F \phi_F + A_B \phi_B + S_u)/A_p$$

The points on the computation grid range from 1 to N_j in the N-S direction with points 1 and N_j on the boundaries. Since the boundary values ϕ_1 and ϕ_{N_j} are known, equations for ϕ_2 to ϕ_{N_j-1} are solved. The set of equations then becomes:

$$\begin{aligned} \phi_2 &= B_2 \phi_3 + C_2 \phi_1 + D_2 \\ \phi_3 &= B_3 \phi_4 + C_3 \phi_2 + D_3 \\ &\vdots \\ \phi_{N_j-1} &= B_{N_j-1} \phi_{N_j} + C_{N_j-1} \phi_{N_j-2} + D_{N_j-1} \end{aligned} \quad (A1.9)$$

Now since ϕ_1 is known ϕ_2 can be eliminated from Equation (A1.9) and so on, yielding a general recurrence relation

$$\phi_j = A_j \phi_{j+1} + D_j' \quad (A1.10)$$

To get the relation for A_j and D_j' Equation (A1.10) is written as

$$\phi_{j-1} = A_{j-1} \phi_j + D_{j-1}'$$

Now putting in the value of ϕ_j

$$\phi_j = \left(\frac{A_N}{A_P - A_S \cdot A_{j-1}} \right)_j \phi_{j+1} + \left[\frac{C_j' + A_S D_{j-1}'}{A_P - A_S A_{j-1}} \right]_j \quad (A1.11)$$

Comparing Equation (A1.10) and (A1.11) yields coefficients for the recurrence formula

$$A_j = (A_N / (A_P - A_S A_{j-1}))_j \quad (A1.12)$$

where

$$D_j' = ((A_S D_{j-1}' + C_j') / (A_P - A_S A_{j-1}))_j \quad (A1.13)$$

Using Equations (A1.12) and (A1.13), ϕ_j can be calculated from Equation (A1.10). Having solved for ϕ_j on one N-S ϕ_j 's on the next N-S line are solved and so on until the entire solution domain is swept. The same treatment is then applied in the W-E direction and finally, in the F-B direction. It is usually necessary to sweep between 1 and 3 times per iteration for optimum solution time.

The coefficient matrix formed by the finite difference equation of ϕ should satisfy the stability condition,

$$A_P \geq \sum_n |A_n|$$

Now

$$A_P = \sum_n A_n - S_P$$

So if

$$S_P \leq 0$$

the above criteria is satisfied. In the solution procedure care is taken so that S_P is always less than or equal to zero.

In the process of the computations, convergence is assessed at the end of each iteration on the basis of the "Residual Source" criterion. The residual source R_ϕ is defined as

$$R_\phi = A_P \phi_P - \sum_n A_n \phi_n - S$$

It is required that:

$$\sum |R_{\phi}| < \epsilon R_{\phi \text{ Ref}}$$

for each finite difference equation.

$R_{\phi \text{ Ref}}$ is the fixed flux of the relevant extensive property fed into the domain of calculation, and ϵ is of the order of 10^{-3} .

When it is the equations for mass fraction of species that are being solved an additional convergence criterion requires that the sum of the mass fractions at each node is \leq to $(1 + \epsilon)$.

When the flow is of variable density it is initially required that the change in density in one iteration at every node must also be less than ϵ

or

$$\left(\rho_{ij}^{\text{new}} - \rho_{ij}^{\text{old}} \right) / \rho_{ij}^{\text{old}} < \epsilon$$

Since the enthalpy values in the calculation domain do not conform with the specie mass fractions during the first few iterations, temperature and density are not updated for the first 10 - 25 iterations. If the density gradients are steep, density is updated every second or third iteration after the first update.

A typical convergence plot is shown in Figure A1-7.

Since the finite difference equations are nonlinear in nature, the convergence is facilitated and sometimes divergence is avoided by under-relaxing the value of ϕ being calculated as:

$$\phi_p^R = F \phi_p^{\text{New}} + (1-F) \phi_p^{\text{Old}} \quad (\text{A1.14})$$

where F is an under-relaxation factor which is less than one.

The way in which the above relation is introduced into the numerical procedure is as follows:

$$\begin{aligned} A_p^R &= A_p / F \\ S_u^R &= S_u + (1 - F) A_p^R \phi_p^{\text{Old}} \end{aligned} \quad (\text{A1.15})$$

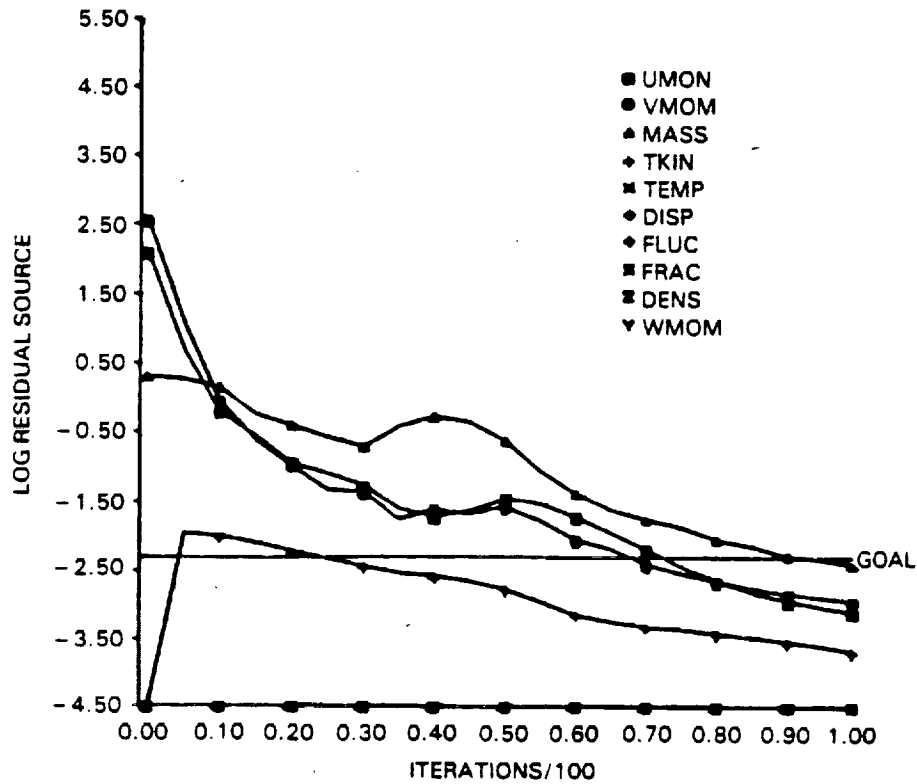


Figure A1-7 Typical Convergence Plot

It can easily be shown that the effect of introducing the above modifications is to under-relax ϕ_p according to Equation (A1.4). From Equation (A1.3) we have

$$\phi_p^{\text{New}} = \frac{\sum_n A_n \phi_n + S_u}{A_p} \quad (\text{A1.16})$$

putting in the under-relaxation factors,

$$\phi_p^R = \frac{\sum_n A_n \phi_n + S_u^R}{A_p^R}$$

putting the value of A_p^R and S_u^R from Equations (A1.14) and (A1.15) in (A1.16),

$$\phi_p^R = \frac{\sum_n A_n \phi_n + S_u + (1-F) A_p^R \phi_p^{Old}}{A_p^R}$$

$$\phi_p^R = \left(\frac{\sum_n A_n \phi_n + S_u}{A_p} \right) F + (1-F) \phi_p^{Old}$$

$$F = \frac{\text{New } F}{\phi_p} + (1-F) \phi_p^{Old}$$

It should also be noted that the effect of under-relaxation is to make the coefficient matrix more diagonally dominant.

The various steps in the numerical procedure can now be summarized as follows:

1. Guess fields for all variables.
2. Assemble coefficients of momentum equations and solve for U^* and V^* using prevailing pressures.
3. Solve the pressure correction equation and update velocities and pressures.
4. Solve equations for other variables.
5. Update fluid properties such as viscosity and density.
6. Test for convergence. If not attained use prevailing fields as new guesses and repeat from step 2 until convergence is attained.

In general, it is necessary to specify ϕ or its gradient at the boundaries of the calculation domain. There are six types of boundaries:

1. Axis of symmetry
2. Unspecified wall
3. Specified wall
4. Unspecified opening
5. Specified opening
6. Specified blockage

A specified boundary is one for which all boundary values such as velocities, temperatures, etc. are given. An unspecified boundary is one for which the boundary values are calculated by the code.

On an axis of symmetry the gradient of all ϕ 's except v-velocity is put to zero; v-velocity itself is set to zero. Most walls are specified, with all velocities set to zero (no slip condition). A moving wall is modeled with the no slip condition by specifying nonzero velocities in the plane of the wall. A porous wall is modeled by specifying nonzero velocities normal to the plane of the wall, or by inputting the wall as unspecified. At the outflow, it is required that there be no negative axial velocity components. At high Reynolds numbers this requirement makes specification of boundary values of all ϕ 's except u redundant. The axial velocity is specified thus,

$$u_{ni, j} = u_{ni-1, j} + U_{INC}$$

where n_i is the outflow boundary and U_{INC} is calculated such that the total mass outflow is equal to main inflow. Alternatively, if an exit velocity profile is known, it can be specified.

The calculation mesh is constrained by the coordinate system, which presently has been selected as orthogonal. Therefore, curvilinear geometries have to be represented in the form of discrete steps or "staircases." The specified blockage boundary condition permits this representation and allows inflow and outflow through elements of these staircases. In addition, the condition allows solid bodies to be placed inside the flowfield and to contain mass sources or sinks within them. This capability is written in generalized form and confers considerable geometric flexibility on the code without the need for interproblem reprogramming.

Adjacent to solid boundaries, the local Reynolds number of the flow based on local velocity and distance from the wall becomes very small and the two-equation turbulence model, which was developed for high Reynolds numbers, becomes inadequate. Although a version of the two equation model that can handle both high and very low local Reynolds numbers exists (Ref. A10), its application requires a large number of grid nodes (more than 30) in the wall layer. This is due to the steep gradients of properties in the wall region (Ref. A11).

To avoid these difficulties, it was argued that the flowfield in the calculation domain is not influenced to first order by the details of the flow at the walls (Ref. A12). Consequently, as a matter of computational efficiency and economy, the high Reynolds number version of the turbulence model was retained and a Couette-flow analysis was used to give an equilibrium boundary layer on all solid surfaces bounding the calculation domain. The resulting wall functions are used to link the walls to the near-wall nodes of the finite difference grid.

APPENDIX A2

TREATMENT OF WALL BOUNDARY LAYERS IN BASELINE CODE

The calculation mesh is constrained by the coordinate system, which presently has been selected as orthogonal. Therefore, curvilinear geometries have to be represented in the form of discrete steps or "staircases." The specified blockage boundary condition permits this representation and allows inflow and outflow through elements of these staircases. In addition, the condition allows solid bodies to be placed inside the flowfield and to contain mass sources or sinks within them. This capability is written in generalized form and confers considerable geometric flexibility on the code without the need for interproblem programming.

Adjacent to solid boundaries, the local Reynolds number of the flow based on local velocity and distance from the wall becomes very small and the two-equation turbulence model, which was developed for high Reynolds numbers, becomes inadequate. Although a version of the two equation model that can handle both high and very low local Reynolds numbers exists (Ref. A2-1), its application requires a large number of grid nodes (more than 30) in the wall layer. This is due to the steep gradients of properties in the wall region (Ref. A2-2).

To avoid these difficulties, it was argued that the flowfield in the calculation domain is not influenced to first order by the details of the flow at the walls (Ref. A2-3). Consequently, as a matter of computational efficiency and economy, the high Reynolds number version of the turbulence model was retained and a Couette-flow analysis was used to give an equilibrium boundary layer on all solid surfaces bounding the calculation domain. The resulting wall functions are used to link the walls to the near-wall nodes of the finite difference grid. The procedure is described below for the momentum transfer, heat transfer, and turbulence processes.

The wall layer is assumed to be one of constant shear stress at the wall ($\tau = \tau_w$). The heat flux is also assumed to be constant ($q'' = q_w$). It should be noted that these conditions are true only for an impermeable wall, with zero or negligible streamwise pressure gradient

$$\left(\text{i.e., } \left| \frac{\tau_w}{\frac{dp}{dx}} \right| \gg y \right)$$

The momentum equation can be reduced to a simple form as shown below. It is assumed that the wall is parallel to the x-axis. In the case of a vertical wall u will be replaced by v and y by x.

$$\frac{\partial}{\partial y} (\mu + \mu_t) \frac{\partial u}{\partial y} = 0$$

Integrating

$$(\mu + \mu_t) \frac{du}{dy} \Big|_0^y = 0$$

at $y=0, \mu_t=0$

so

$$\mu \frac{du}{dy} \Big|_{y=0} = (\mu + \mu_t) \frac{du}{dy} \Big|_{y=y}$$

or

$$\tau = (\mu + \mu_t) \frac{du}{dy} \tag{A2.1}$$

or

$$\frac{\tau}{\tau_w} = \left(1 + \frac{\mu_t}{\mu}\right) \frac{du^+}{dy^+}$$

where

$$y^+ = \frac{u_\tau y}{\nu}, \quad u^+ = \frac{u}{u_\tau}, \quad u_\tau = \sqrt{\frac{\tau_w}{\rho}}$$

Near the wall the local Reynolds number changes considerably and the approach adopted depends on the value of the local Reynolds number, y^+ , based on distance y from the wall and friction velocity u_τ .

For convenience the wall region is divided into two layers $y^+ \leq 11.63$, a fully laminar region, and $y^+ \geq 11.63$, a fully turbulent region. Then for $y^+ \leq 11.63, \mu_t \ll \mu$. Hence from Equation (A2.1)

$$\tau = \mu \frac{du}{dy} \quad (A2.2)$$

Also for $y^+ \geq 11.63 \mu_t \gg \mu$ and $\tau/\tau_w = 1$.

Hence from Equation (A2.2)

$$\frac{\mu_t}{\mu} \frac{du^+}{dy^+} = 1$$

From log-law of the wall (Ref. A2-4),

$$u^+ = 1/\kappa \log_e(Ey^+)$$

$$\frac{du^+}{dy^+} = \frac{1}{\kappa y^+}$$

$$\mu_t = \mu \kappa y^+$$

Hence from Equation (A2.1)

$$\tau = \mu \kappa y^+ \frac{du}{dy}$$

It should be noted that E is an integration constant that depends on the magnitude of the variation of shear stress across the layer or the roughness of the wall. The value of E used in the program is for smooth walls with constant shear stress. Effects of mass transfer across the layer and severe pressure gradients can be incorporated by modifying E which will then no longer be a constant.

In the case of flow with swirl, the axial velocity u is replaced by the resultant velocity, u_R , where

$$u_R = \sqrt{u^2 + w^2}$$

for walls parallel to the x-axis.

The shear stress τ then becomes the resultant shear stress τ_R and the shear stress in x and θ directions can be obtained by resolving this stress

$$\tau_x = \tau_R \frac{u}{u_R}$$

$$\tau_\theta = \tau_R \frac{w}{u_R}$$

If the wall is isothermal or the temperature distribution is specified, the following treatment, which is the same as the treatment used for momentum transfer is adopted. The energy equation can be reduced to

$$\dot{q}'' = (\Gamma + \Gamma_t) c_p \frac{dT}{dy} \quad (A2.3)$$

$$\frac{\dot{q}''}{q_w} = \left(\frac{\Gamma}{\nu} + \frac{\Gamma_t}{\nu} \right) \frac{dT^+}{dy^+} \quad (A2.4)$$

where

$$T^+ = \frac{\rho u_\tau c_p (T_w - T)}{\dot{q}_w''}$$

also

(A2.5)

$$T^+ = \sigma_{\phi,t} \left[u^+ + \left(\left(\frac{\sigma_\phi}{\sigma_{\phi,t}} \right)^{3/4} + 1 \right) \right]$$

ϕ = Laminar Prandtl number

ϕ_t = Turbulent Prandtl number

Now for $y^+ \leq 11.63$, $\Gamma > \Gamma_t$ from Equation (A2.3)

$$\dot{q}'' = \Gamma c_p \frac{dT}{dy}$$

For

$$y^+ \geq 11.63 \quad \Gamma \ll \Gamma_t \quad \sqrt{\frac{\dot{q}''}{q_w}} = 1$$

Therefore from Equation (A2.4)

$$\frac{\Gamma \epsilon}{\mu} \frac{dT^+}{dy^+} = 1 \quad (A2.6)$$

From Equation (A2.5)

$$\frac{dT^+}{dy^+} = \frac{\sigma_{\phi, \epsilon}}{\kappa y^+} \quad (A2.7)$$

Putting Equation (A2.6) and (A2.7) in Equation (A2.3)

$$\dot{q}'' = \frac{\kappa y^+ C_p}{\sigma_{\phi, \epsilon} \mu} \frac{dT}{dy} \quad (A2.8)$$

If the heat transfer rate to the wall \dot{q}_w'' rather than its temperature is specified Equation (A2.8) can be replaced by

$$\dot{q}_w'' = Q$$

where Q is obtained from experiments.

For adiabatic walls

$$\dot{q}_w'' = 0$$

The approach adopted for the turbulence equations is strictly valid for the initial sublayer where the flow is assumed to be completely turbulent: $y^+ > 30$, but sufficiently close to the wall so that the assumption of constant shear stress applies ($y^+ < 400$). In this region, the local rate of production of turbulence is balanced by the viscous dissipation rate. This local equilibrium forms the primary basis for specification of turbulent kinetic energy and its dissipation rate at the wall.

In case of local equilibrium,

$$-\rho \overline{u'v'} \frac{du}{dy} = \rho \epsilon$$

Also, shear stress near wall (Ref. A2-5),

$$\tau_w = -\rho \overline{u'v'} = \rho C_\mu^{1/2} K$$

(Experimental evidence suggests $\overline{u'v'} = 0.3 K$).

Using the "law of the wall,"

$$\rho \epsilon = \frac{(\rho C_\mu^{1/2} K)^{3/2}}{\rho^{1/2} \kappa y}$$

where κ is the constant in the log-law "law of the wall."

Hence the wall boundary value for dissipation is

$$\epsilon = \frac{C_\mu^{3/4} K^{3/2}}{\kappa y}$$

The value of K at the boundary is put to zero. The production of turbulence energy in the cell adjacent to the wall is

$$P_K = -\rho \overline{u'v'} \frac{du}{dy} = \tau_w \frac{du}{dy}$$

The dissipation term in the kinetic energy equation is found from the average over the control volume. The reason for using this technique is that is highly nonlinear in the vicinity of the wall. Hence,

$$\int_0^{y_p} \rho \epsilon \, dy = \int_0^{y_p} \frac{\rho C_\mu^{3/4} K^{3/2}}{\kappa y} \cdot dy$$

The integral of the above expression will be logarithmic and infinite at the lower limit. Hence, using the log law again,

$$\frac{du}{dy} = \sqrt{\frac{\tau_w}{\rho}} \cdot \frac{1}{\kappa y}$$

$$\therefore \int_0^{y_p} \frac{\rho C_\mu^{3/4} K^{3/2}}{\kappa y} \cdot dy = \int_0^{u_p} \frac{\rho C_\mu^{3/4} K^{3/2}}{\sqrt{\frac{\tau_w}{\rho}}} \cdot du = \rho C_\mu^{3/4} K^{3/2} u^+$$

where

$$u^+ = y^+ \quad \text{for} \quad y^+ \leq 11.63$$

and

$$u^+ = \frac{1}{\kappa} \log_e E y^+ \quad \text{for} \quad y^+ > 11.63$$

As stated earlier, these wall functions are based on the assumption of constant shear stress and impermeable smooth wall with negligible pressure gradient. Any departure from this condition is going to cause incorrect prediction of wall shear stress and heat transfer. In the recirculation region, especially near the reattachment point, it is unlikely that the log-law of the wall should be applicable and the predictions in this region will also be incorrect. However, in spite of the above apparent weaknesses the two equation model does an adequate job of predicting turbulence quantities.

APPENDIX A3

DERIVATION OF EXTRA TERMS GENERATED DUE TO SYSTEM ROTATION

In Figure A3-1, O_0, X_0, Y_0, Z_0 is the inertial frame and O_1, X_1, Y_1, Z_1 is the moving frame. The motion of the latter is described by the position vector \bar{R} of its origin and a vector $\bar{\Omega}$, the rotation of the moving frame about an axis through its origin. The components of \bar{R} parallel to O_0X_0, O_0Y_0, O_0Z_0 define the position of the moving frame and the components of $\bar{\Omega}$, define its rotation about the axis of inertial frame. The position vector r_0 and r_1 define the position of a particle 'P' in two frames of references. The line labelled 'path' is the track of 'P' seen by the moving observer. To him the location of its path does not change with time and inertial observer sees the same line traveling through space. Therefore:

$$\bar{r}_0 = \bar{r}_1 + \bar{R} \quad (A3.1)$$

The acceleration of P seen by the moving observer is:

$$\frac{d_1^2 \bar{r}_1}{dt^2} = \frac{d_1}{dt} \frac{d_1 \bar{r}_1}{dt} \quad (A3.2)$$

and the acceleration seen by the inertial observer is:

$$\frac{d_0^2 \bar{r}_0}{dt^2} = \frac{d_0}{dt} \frac{d_0 \bar{r}_0}{dt} \quad (A3.3)$$

The operator d_0/dt is for differentiation in inertial frame and d_1/dt is for the moving frame.

The relationships between the velocity and acceleration of A seen by the two observers can be found bearing in mind that \bar{r}_0 varies with time because of motion of P, \bar{R} varies because of the motion of O_1 and r_1 varies because of the motion of A and rotation of the moving frame. This gives:

$$\frac{d_0 \bar{r}_0}{dt} = \frac{d_0 \bar{R}}{dt} + \frac{d_1 \bar{r}_1}{dt} + (\bar{\Omega} \times \bar{r}_1) \quad (A3.4)$$

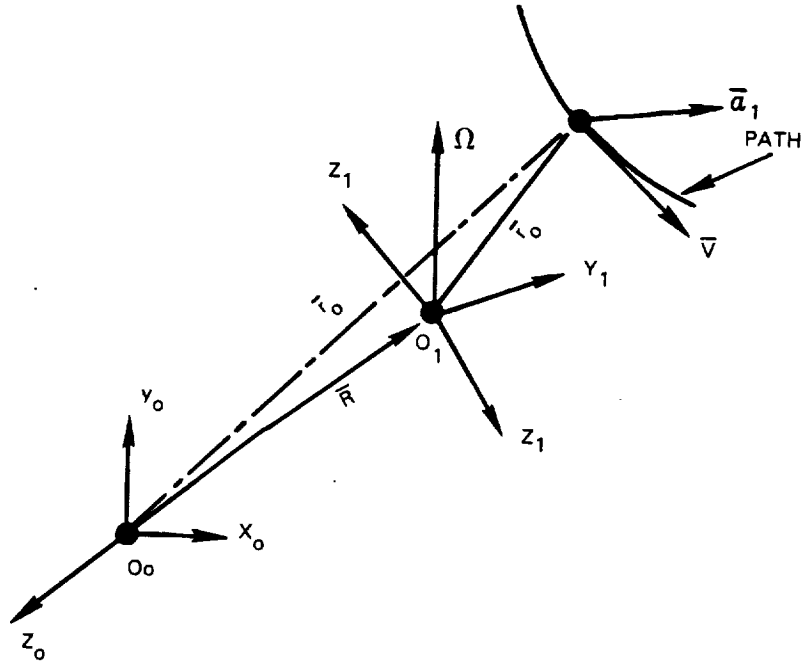


Figure A3-1 Derivation of extra terms generated due to system rotation

Differencing again in the inertial frame,

$$\begin{aligned}
 \frac{d_0^2 \bar{r}_0}{dt^2} &= \frac{d_0^2 \bar{R}}{dt^2} + \frac{d_0}{dt} \frac{d_1 \bar{r}_1}{dt} + \frac{d_0}{dt} (\bar{r}_1 \times \bar{\Omega}) \\
 &= \frac{d_0^2 \bar{R}}{dt^2} + \frac{d_0}{dt} \frac{d_1 \bar{r}_1}{dt} + \bar{r}_1 \times \frac{d_0 \bar{\Omega}}{dt} + \bar{\Omega} \times \frac{d_0 \bar{r}_1}{dt}
 \end{aligned} \tag{A3.5}$$

A correspondence between the operator d_0/dt and d_1/dt can be found from equations (A3.1) and (A3.4).

Differentiation of equation (A3.1) in the inertial frame gives:

$$\frac{d_0 \bar{r}_0}{dt} = \frac{d_0 \bar{r}_1}{dt} + \frac{d_0 \bar{R}}{dt} \tag{A3.6}$$

From equations (A3.4) and (A3.6) it can be seen that

$$\frac{d_0 \bar{r}_0}{dt} = \frac{d_0 \bar{R}}{dt} + \frac{d_1 \bar{r}_1}{dt} + (\bar{\Omega} \times \bar{r}_1) = \frac{d_0 \bar{r}_1}{dt} + \frac{d_0 \bar{R}}{dt}$$

or

$$\frac{d_0 \bar{r}_1}{dt} = \frac{d_0 \bar{r}_1}{dt} + (\bar{\Omega} \times \bar{r}_1) \quad (A3.7)$$

or

$$\frac{d_0}{dt} = \frac{d_1}{dt} + (\bar{\Omega} \times \bar{r}_1) \quad (A3.8)$$

Equation (A3.8) is the relationship between the derivatives in two frames.

From equations (A1.5) and (A1.8).

$$\begin{aligned} \frac{d_0^2 \bar{r}_0}{dt^2} &= \frac{d_0^2 \bar{R}}{dt^2} + \left\{ \frac{d_1}{dt} + (\bar{\Omega} \times) \right\} \left\{ \frac{d_1 \bar{r}_1}{dt} \right\} \\ &\quad + \bar{r}_1 \times \frac{d_0 \bar{\Omega}}{dt} + \bar{\Omega} \times \left\{ \frac{d_1}{dt} + (\bar{\Omega} \times) \right\} \left\{ \bar{r}_1 \right\} \\ &= \frac{d_0^2 \bar{R}}{dt^2} + \frac{d_1^2 \bar{r}_1}{dt^2} + \bar{\Omega} \times \frac{d_1 \bar{r}_1}{dt} + \bar{r}_1 \frac{d_0 \bar{r}}{dt} \\ &\quad + \bar{\Omega} \times \frac{d_1 \bar{r}_1}{dt} + (\bar{\Omega} \times \bar{r}_1) \end{aligned}$$

$$\begin{aligned} \frac{d_0^2 \bar{r}_0}{dt^2} &= \frac{d_0^2 \bar{R}}{dt^2} + \frac{d_1^2 \bar{r}_1}{dt^2} + \bar{\Omega} \times \frac{d_1 \bar{r}_1}{dt} + \bar{r}_1 \frac{d_0 \bar{\Omega}}{dt} \\ &\quad + \bar{\Omega} \times \frac{d_1 \bar{r}_1}{dt} + \bar{\Omega} \times (\bar{\Omega} \times \bar{r}_1) \end{aligned}$$

(A3.9)

$$= \frac{d_0^2 \bar{r}}{dt^2} + \frac{d_1^2 \bar{r}_1}{dt^2} + \frac{d_0 \bar{\Omega}}{dt} \times \bar{r}_1 + 2\bar{\Omega} \times \frac{d_1 \bar{r}_1}{dt} + \bar{\Omega} \times (\bar{\Omega} \times \bar{r}_1)$$

The terms in equation (A3.9) can be interpreted as follows:

- (a) $\frac{d_0^2 \bar{r}_0}{dt^2}$ Acceleration of particle P to an observer in inertial frame.
- (b) $\frac{d_0^2 \bar{R}}{dt^2}$ Acceleration of moving frame (translation) as observed from inertial frame.
- (c) $\frac{d_1^2 \bar{r}_1}{dt^2}$ Acceleration of particle P to an observer in the moving frame.
- (d) $\frac{d_0 \bar{\Omega}}{dt} \times \bar{r}_1$ Angular acceleration of the moving frame to an observer in the inertial frame.
- (e) $2\bar{\Omega} \times \frac{d_1 \bar{r}_1}{dt}$ Coriolis acceleration of P generated due to rotation.
- (f) $\bar{\Omega} \times (\bar{\Omega} \times \bar{r}_1)$ Centripetal acceleration of P when fixed in position in the moving frame, and the moving frame is rotating at constant angular velocity.

For an observer in the moving frame (with no translation) the terms (a), (b) and (d) in equation (A3.9) would disappear and equation (A3.9), in moving frame becomes:

$$\frac{d_1^2 \bar{r}_1}{dt^2} + 2\bar{\Omega} \times \frac{d_1 \bar{r}_1}{dt} + \bar{\Omega} \times (\bar{\Omega} \times \bar{r}_1) = 0 \quad (\text{A3.10})$$

writing $\frac{d_1^2 \bar{r}_1}{dt^2} = \bar{A}$, acceleration of particle P

and $\frac{d_1 \bar{r}_1}{dt} = \bar{V}$, velocity of particle P

in the rotating frame equation (A3.10) becomes:

$$\bar{A} + 2\bar{\Omega} \times \bar{V} + \bar{\Omega} \times (\bar{\Omega} \times \bar{r}_1) = 0 \quad (A3.11)$$

So an observer in the rotating frame can use the components of the acceleration he sees (\bar{A}) for Du/Dt , Dv/Dt , Dw/Dt (in momentum equation), provided he includes the extra 'apparent' body forces of per unit mass.

$$-2 [\bar{\Omega} \times \bar{V} + \bar{\Omega} \times (\bar{\Omega} \times \bar{r}_1)]$$

where

$$= i\Omega_x + j\Omega_y + k\Omega_z, \bar{V} = iu + jv + kw, \bar{r}_1 = ix + jy + kz$$

To use the extra terms generated due to system rotation in momentum equations used in TEACH the terms shown above should be multiplied by density ($\bar{\rho}$), i.e. $-\bar{\rho} [2\bar{\Omega} \times \bar{V} + \bar{\Omega} \times (\bar{\Omega} \times \bar{r}_1)]$.

These terms go into generalized equation in TEACH as source terms ($S_{\Omega\phi}$), i.e.

$$S_{\Omega\phi} = -\bar{\rho} [2\bar{\Omega} \times \bar{V} + \bar{\Omega} \times (\bar{\Omega} \times \bar{r}_1)] \quad (A3.12)$$

Resolving equation (A3.12) in i, j, and k directions gives:

$$-\bar{\rho} 2(\bar{\Omega} \times \bar{V}) = -2i\bar{\rho} [\bar{\omega}\Omega_y - \bar{v}\Omega_z] + 2j\bar{\rho} [\bar{w}\Omega_x - \bar{u}\Omega_z] - 2k\bar{\rho} [\bar{w}\Omega_x - \bar{u}\Omega_y] \quad (A3.13)$$

$$-\bar{\rho} \bar{\Omega} \times (\bar{\Omega} \times \bar{r}_1) = -i\bar{\rho} [\Omega_y (y\Omega_x - x\Omega_y) - \Omega_z (x\Omega_z - z\Omega_x)]$$

$$+ j\bar{\rho} [\Omega_x (y\Omega_x - x\Omega_y) - \Omega_z (z\Omega_y - y\Omega_z)]$$

$$- k\bar{\rho} [\Omega_x (x\Omega_z - z\Omega_x) - \Omega_y (z\Omega_y - y\Omega_z)] \quad (A3.14)$$

Adding (A3.13) and (A3.14) we get:

$$(S_{\Omega\phi}) = -\bar{\rho} [2\bar{\Omega} \times \bar{V} + \bar{\Omega} \times (\bar{\Omega} \times \bar{r}_1)]$$

$$\begin{aligned}
&= i [\bar{\rho}(\bar{v} - z\Omega_x + x\Omega_z) \Omega_z - \bar{\rho}(\bar{w} - x\Omega_y + y\Omega_x)\Omega_y + \bar{\rho}\bar{v}\Omega_z - \bar{\rho}\bar{w}\Omega_y] \\
&+ j [\bar{\rho}(\bar{w} - x\Omega_y + y\Omega_x) \Omega_x - \bar{\rho}(\bar{u} - y\Omega_z + z\Omega_y)\Omega_z + \bar{\rho}\bar{w}\Omega_x - \bar{\rho}\bar{u}\Omega_z] \\
&+ k [\bar{\rho}(\bar{u} - y\Omega_z + z\Omega_y) \Omega_y - \bar{\rho}(\bar{v} - z\Omega_x + x\Omega_z)\Omega_x + \bar{\rho}\bar{u}\Omega_y - \bar{\rho}\bar{v}\Omega_x]
\end{aligned}
\tag{A3.15}$$

Contribution of Rotation in Stagnation Enthalpy Equation (H rot)

Contribution of rotation to the stagnation in enthalpy can be found by forming dot product of the velocity vector (\bar{v}) and the extra apparent body forces generated by the system rotation. This becomes:

$$\begin{aligned}
H_{rot} &= \rho \bar{v} \cdot [- (2\bar{\Omega} \bar{v} + \bar{\Omega} \times (\bar{\Omega} \times \bar{r}_1))] \\
&= \rho \bar{v} \cdot [- (\bar{\Omega} \times (\bar{\Omega} \times \bar{r}_1))] \\
&= -\rho \bar{v} \cdot [\bar{\Omega} (\bar{\Omega} \cdot \bar{r}_1) - \bar{r}_1 (\bar{\Omega} \cdot \bar{\Omega})]
\end{aligned}$$

These extra terms generated due to rotation go into the generalized TEACH equations as extra source terms (S_H), i.e.

$$\begin{aligned}
S_{\Omega H} &= -\bar{\rho} \bar{v} \cdot [\bar{\Omega} (\bar{\Omega} \cdot \bar{r}_1) - \bar{r}_1 (\bar{\Omega} \cdot \bar{\Omega})] \\
S_{\Omega H} &= -\bar{\rho} \bar{v} \cdot [\bar{\Omega}(\Omega_x x + \Omega_y y + \Omega_z z) - \bar{r}_1(\Omega_x^2 + \Omega_y^2 + \Omega_z^2)] \\
&= -\bar{\rho} (i u + j v + k w) \cdot [(i \Omega_x + j \Omega_y + k \Omega_z) (\Omega_x x + \Omega_y y + \Omega_z z) \\
&\quad - (i x + j y + k z) (\Omega_x^2 + \Omega_y^2 + \Omega_z^2)] \\
&= -\bar{\rho} [(u \Omega_x + v \Omega_y + w \Omega_z) (\Omega_x x + \Omega_y y + \Omega_z z) \\
&\quad - (u x + v y + w z) (\Omega_x^2 + \Omega_y^2 + \Omega_z^2)]
\end{aligned}$$

collecting the u, v, w terms and averaging gives:

$$S_{\Omega H} = -\bar{\rho} \bar{u} [\Omega_x^2 x + \Omega_x \Omega_y y + \Omega_x \Omega_z z - \Omega_x^2 x - \Omega_y^2 x - \Omega_z^2 x]$$

$$\begin{aligned}
& - \bar{\rho} \bar{v} [\Omega_y \Omega_x^2 + \Omega_y^2 y + \Omega_y \Omega_z^2 - y \Omega_x^2 - y \Omega_y^2 - y \Omega_z^2] \\
& - \bar{\rho} \bar{w} [\Omega_z \Omega_x^2 + \Omega_z \Omega_y^2 + \Omega_z^2 z - z \Omega_x^2 - z \Omega_y^2 - z \Omega_z^2]
\end{aligned}$$

or

$$\begin{aligned}
S_H = & - \bar{\rho} \bar{u} [\Omega_y (\Omega_x y - \Omega_y x) + \Omega_z (\Omega_x z - \Omega_z x)] \\
& - \bar{\rho} \bar{v} [\Omega_x (\Omega_y x - \Omega_x y) + \Omega_z (\Omega_y z - \Omega_z y)] \\
& - \bar{\rho} \bar{w} [\Omega_x (\Omega_z x - \Omega_x z) + \Omega_y (\Omega_z y - \Omega_y z)]
\end{aligned}$$

(A3.16)

The expression in (A3.15) has been modeled into 3D-TEACH separately in u, v and w momentum equations, i.e., i-component in u-equation, j-component in u-equation, and k-component in w-equation.

The expression in (A3.16) has been modeled in 3D-TEACH code as shown above.

REFERENCES

1. Sturgess, G.J., "Stationary State Computational Fluid Dynamics for Aero Propulsion Devices," Computational Methods, Edit. K. L. Strange, CPIA Publication 401, February 1984, pp. 25-51.
2. Gosman, A.D. and Ideriah, F.T.K., "TEACH-2E: A General Computer Program for Two-Dimensional, Turbulent, Recirculating Flows," Imperial College, London, England, Mech. Engrg. Rept., (unnumbered), June 1976.
3. Sturgess, G.J., "Aerothermal Modeling, Phase I - Final Report," NASA Report CR 168202, May 27, 1983.
4. Leonard, B.P., "A Survey of Finite-Differences of Opinion on Numerical Muddling of the Incomprehensible Defective Confusion Equation," Applied Mechanics Division, ASME Winter Annual Meeting, New York, December 1979.
5. Boni, A.A., "Comments on the Computational Aspects of Turbulent Combustion," Acta Astronautica, Vol. 6, 1979, pp. 991-995.
6. Spalding, D.B., "A Novel Finite-Difference Formulation of Differential Expressions Involving Both First and Second Derivatives," Intl. J. Numerical Methods in Engineering, Vol. 4, 1972, p. 551.
7. Jones, W.P. and McGuirk, J.J., "Mathematical Modeling of Gas-Turbine Combustion Chambers," AGARD Conference Proceedings No. 275, Combustor Modeling, AGARD, 1980, pp. 4,1-4,11.
8. Jones, W.P. and Whitelaw, J.H., "Calculation Methods for Reacting Turbulent Flows," Proc. Panel Discussion, Prediction of Turbulent Reacting Flows in Practical Systems, Edit. T. Morel, ASME Fluids Engineering Conference, Boulder, Colorado, June 22-24, 1981, pp. 9-22.
9. Leonard, B.P., "A Stable and Accurate Convective Modeling Procedure Based on Quadratic Upstream Interpolation," Computer Methods in Applied Mechanics and Engineering, Vol. 19, 1979, pp. 59-98.
10. Raithby, G.D., "Skew Upstream Differencing Schemes for Problems Involving Fluid Flow," Computer Methods in Applied Mechanics and Engineering, Vol. 9, 1976, pp. 153-164.
11. Chang, S.M., Humphrey, J.A.C. and Modavi, A., "Turbulent Flow in a Strongly Curved U-Bend and Downstream Tangent of Square Cross-Section," University of California, Berkeley, Dept. Mech. Eng., Report No. FM-82-1, November 1982.
12. Sturgess, G.J. and Syed, S.A., "Widely-Spaced Co-Axial Jet Diffusion Flame Combustor: Isothermal Flow Calculations Using the Two-Equation Turbulence Model," Paper No. AIAA-82-0113, AIAA-20th Aerospace Sciences Meeting, Orlando, Florida, January 1982.

13. Jones, W.P. and McGuirk, J.J., "Mathematical Modelling of Gas-Turbine Combustion Chambers," AGARD Conference Proceedings No. 275, Combustor Modeling, AGARD, 1980, pp. 4,1-4,11, (see discussion).
14. Johnston, J.P., "The Effects of Rotation on Boundary Layers in Turbo-machine Rotors," Thermosciences Division, Rept. MD-24, Mech. Eng. Dept., Stanford University, May 1970.
15. Technical Proposal for Coolant Passage Heat Transfer with Rotation, P&W Document No. 82-4021, June 7, 1982.
16. Meyer, R.E., Introduction to Mathematical Fluid Dynamics, Dover, 1982, pp. 131-142.
17. Moon, I-Man, "Effects of Coriolis Force on the Turbulent Boundary Layer in Rotating Fluid Machines," Gas Turbine Lab. Report No. 74, Massachusetts Institute of Technology, June 1964.
18. Moore, J., "Effects of Coriolis on Turbulent Flow in Rotating Rectangular Channels," Gas Turbine Lab. Report No. 89, Massachusetts Institute of Technology, May 1968.
19. Sahm, M.K. and Metzger, D.E., "Effects of Turn Geometry Parameters on Heat Transfer Around Smooth Wall 180° Turns in Rectangular Ducts of Aspect Ratio 1.0 to 3.0," Technical Report ERC-R-83029, Mechanical and Aerospace Engineering, Arizona State University, July 1983.
20. Hart, J.E., "Instability and Secondary Motion in Rotating Channel Flow," J. Fluid. Mech., Vol. 45, Pt. 2, 1971, pp. 341-351.
21. Speziale, C.G., "Numerical Study of Viscous Flow in Rotating Rectangular Ducts," J. Fluid. Mech., Vol. 122, 1982, pp. 251-271.
22. Schlichting, H., Boundary Layer Theory, 7th Edit., McGraw-Hill, 1979, p. 567.
23. Metzger, D. and Sahm, M., "Measured Heat Transfer in Smooth Rectangular Duct with 180° Sharp-Corner Turns," Technical Report ERC-R-83003, Mechanical and Aerospace Engineering, Arizona State University, January 1983.
24. Clauser, F.H., "Turbulent Boundary Layers in Adverse Pressure Gradients," J. Aero. Sc., Vol. 21, No. 2, February 1954.

Appendix A1


- A1. Schlichting, H., Boundary Layer Theory, 7th Edition, McGraw-Hill, 1979, pp. 47-69.
- A2. Hinze, J. O., Turbulence, 2nd Edition, McGraw-Hill, 1975, pp. 20-24.
- A3. Gosman, A. D., Lockwood, F. C., and Syed, S. A., "Prediction of a Horizontal Free Turbulent Diffusion Flame," 16th Symposium (International) on Combustion, The Combustion Institute, 1976, pp. 1543-1555, (see discussion).

- A4. Roach, P. J., Computational Fluid Dynamics, Aermosa Publishers, New Mexico, 1976.
- A5. Carnahan, B., Luther, H. A., and Wilkes, J. O., Applied Numerical Methods, John Wiley and Sons, New York, 1969.
- A6. Richtmeyer, R. O., and Morton, K. W., Difference Methods for Initial Value Problems, Interscience Publishers Inc., New York, 1957.
- A7. Spalding, D. B., "A Novel Finite-Difference Formulation for Differential Expressions Involving Both First and Second Derivatives," Intl. J. Numerical Methods in Engineering, Vol. 4, 1972, pp. 551.
- A8. Patankar, S. V. and Spalding, D. B., "A Calculation Procedure for Heat, Mass and Momentum Transfer in Three-Dimensional Parabolic Flows," Intl. J. Heat. Mass Transfer, Vol. 15, 1972, p. 1787.
- A9. Paceman, D. W., and Rachford, H. H., Jr., "The Numerical Solution of Parabolic and Elliptic Differential Equations," J. Soc. Industrial Applied Math., Vol. 3, 1955, pp 28-41.
- A10. Jones, W. P., and Launder, B. E., "The Prediction of Laminarization With a Two-Equation Model of Turbulence," Intl. J. Heat Mass Transfer, Vol. 15, 1969, pp. 301-319.
- A11. Launder, B. E., Priddin, C., and Sharma, B., "The Calculation of Turbulent Boundary Layers on Spinning and Curved Surfaces," Trans, ASME, J. Fluids Engineering, March, 1977, pp. 231-239.
- A12. Sturgess, G. J. and Syed, S. A., "Widely-Spaced Co-Axial Jet Diffusion Flame Combustor: Isothermal Flow Calculations Using the Two-Equation Turbulence Model," AIAA-20th Aerospace Sciences Meeting, Paper No. AIAA-82-0133, Orlando, Florida, January 1982.

Appendix A2

- A2-1. Jones, W.P. and Launder, B.E., "The Prediction of Laminarization with a Two-Equation Model of Turbulence," Intl. J. Heat Mass Transfer, Vol. 15, 1969, pp. 301-319.
- A2-2. Launder, B.E., Priddin, C. and Sharma, B., "The Calculation of Turbulent Boundary Layers on Spinning and Curved Surfaces," Trans. ASME, J. Fluids Engrg., March 1977, pp. 231-239.
- A2-3. Sturgess, G.J. and Syed, S.A., "Widely-Spaced Co-Axial Jet, Diffusion Flame Combustor: Isothermal Flow Calculations Using the Two-Equation Turbulence Model," AIAA-20th. Aerospace Sciences Meeting, Paper No. AIAA-82-0133, Orlando, Florida, January 1982.

- A2-4 Hinze, J.O., Turbulence, McGraw-Hill, 1975.
- A2-5. Launder, B.E. and Spalding, D.B., "The Numerical Computation of Turbulent Flows," Computer Methods in Applied Mechanics and Engrg., Vol. 3, 1974, pp. 269-289.

1. REPORT NO. CR - 182109	2. GOVERNMENT AGENCY NASA	3. RECIPIENT'S CATALOG NO.	
4. TITLE AND SUBTITLE Coolant Side Heat Transfer With Rotation Task III Report: Application of Computational Fluid Dynamics		5. REPORT DATE January 1989	6. PERFORMING ORG. CODE
7. AUTHOR(S) F. C. Kopper, G. J. Sturgess, P. Datta		8. PERFORMING ORG. REPT. NO. PWA 5930-29	
9. PERFORMING ORG. NAME AND ADDRESS UNITED TECHNOLOGIES CORPORATION Pratt & Whitney Commercial Engine Business		10. WORK UNIT NO.	
12. SPONSORING AGENCY NAME AND ADDRESS National Aeronautics and Space Administration Lewis Research Center 21000 Brookpark Road, Cleveland, Ohio 44135		11. CONTRACT OR GRANT NO. NAS3-23691	
		13. TYPE REPT./PERIOD COVERED Contractor Report	
		14. SPONSORING AGENCY CODE 505-62-21	
15. SUPPLEMENTARY NOTES Frederick C. Yeh, NASA Lewis Research Center, Cleveland, Ohio 44135			
16. ABSTRACT An experimental and analytical program was conducted to investigate heat transfer and pressure losses in rotating multipass passages with configurations and dimensions typical of modern turbine blades. This program is part of the NASA "Hot Section Technology (HOST)" program and has as its overall objective, the development and verification of improved analysis methods that will form the basis for a design system that will produce turbine components with improved durability. As part of this overall program, the work reported herein involves development of computational fluid dynamic techniques. The specific objectives were to: 1) select a baseline CFD computer code, 2) assess the limitations of the baseline code, 3) modify the baseline code for rotational effects, 4) verify the modified code against benchmark experiments in the literature, and 5) identify shortcomings in the code as revealed by the verification. The Pratt & Whitney 3D-TEACH CFD code was selected as the vehicle for this program. The code was modified to account for rotating internal flows, and these modifications were evaluated for flows characteristic of those expected in the application. Results of this phase of the program indicate that the 3D-TEACH code is a suitable selection as a baseline code and that CFD can make a useful contribution to blade internal cooling.			
17. KEY WORDS (SUGGESTED BY AUTHOR(S)) 3D-TEACH, Computational Fluid Dynamics, Turbine Blades, Multipass Coolant Passages, Coolant-Side, Stair-Step, 3-D Rotational Code, Heat Transfer, Flow Visualization, Boundary Layer		18. DISTRIBUTION STATEMENT 	
19. SECURITY CLASS THIS (REPT) Unclassified	20. SECURITY CLASS THIS (PAGE) Unclassified	21. NO. PGS	22. PRICE *

1947

1948